Performance Improvement of the Rover 1S/60 Gas Turbine Compressor

by

Ruben Vincent Luiten

Thesis presented in partial fulfilment of the requirements for the degree of Master of Engineering (Mechanical) in the Faculty of Engineering at Stellenbosch University

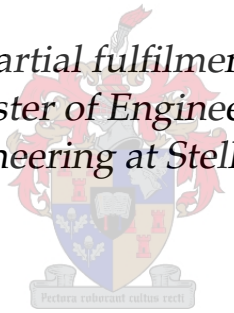

Supervisors:

Prof. T.W. von Backström
Mr. R. Haines
Dr. S.J. van der Spuy

March 2015

Declaration

By submitting this thesis electronically, I declare that the entirety of the work contained therein is my own, original work, that I am the sole author thereof (save to the extent explicitly otherwise stated), that reproduction and publication thereof by Stellenbosch University will not infringe any third party rights and that I have not previously in its entirety or in part submitted it for obtaining any qualification.

Signature: .....
R.V. Luiten

Date: 28/11/2014 .....

Performance Improvement of the Rover 1S/60 Gas Turbine Compressor

by

Ruben Vincent Luiten

Thesis presented in partial fulfilment of the requirements for the degree of Master of Engineering (Mechanical) in the Faculty of Engineering at Stellenbosch University

Supervisors:

Prof. T.W. von Backström Mr. R. Haines Dr. S.J. van der Spuy
Department of Mechanical and Mechatronic Engineering

March, 2015

Abstract

The use of gas turbines in central receiver solar power plant cycles has become an increasingly popular research topic. This has led to the need to investigate and analyse the effect of the solar receiver on the gas turbine cycle. The aim of this thesis is to construct an experimental gas turbine setup to accommodate further research on utilizing solar energy to power gas turbines. The gas turbine under consideration is the Rover Gas Turbines 1S/60. The focus of this investigation is the centrifugal compressor of the gas turbine. An increase in static pressure is required for the gas turbine to cope with anticipated pressure drops in the central receiver that will be part of the gas turbine cycle. The standard compressor design is analysed by means of 3-D (CFD) analysis using CFX® and experimental data. The new centrifugal compressor is designed by means of 1-D and 3-D (CFD) analysis using CompAero and CFX®. The aim is to design a compressor that maximizes the total-to-static pressure ratio. The size of the compressor is highly constrained by the geometry parameters of the gas turbine. Since the turbine rotor will remain unchanged, the power input, mass flow rate and rotational speed must stay the same. The experimental setup was build and the numerical results of the standard compressor were validated against the experimental results. A new centrifugal compressor was designed. The total-to-static pressure ratio was increased from 2.50 to 3.30 at an operating speed of 46 krpm. The efficiency of the compressor was improved from 63.8% to 85.6%. The input power of the new compressor design deviated 1.6% from the set benchmark, and 1.3% from the numerical data of the standard compressor.

Uittreksel

Die gebruik van gasturbines in sonkragstasiesiklusse met 'n sentrale ontvanger het gegroei tot 'n gewilde navorsingsonderwerp. Dit het gelei tot die behoefte om die effek van die sonontvanger op die gasturbinesiklus te ondersoek en te analiseer. Die doel van hierdie tesis is om 'n eksperimentele gasturbine opstelling te bou vir verdere navorsing oor die benutting van sonenergie om 'n gasturbine aan te dryf. Die gasturbine in oorweging is die Rover Gas Turbines 1S/60. Die fokus van hierdie ondersoek is die sentrifugale kompressor van die gasturbine. 'n Toename in statiese druk word benodig vir die gasturbine om die verwagte drukverlies in die sentrale ontvanger, wat deel uit maak van die gasturbinesiklus, te hanteer. Die standaard kompressor ontwerp is geanaliseer deur middel van 3-D Berekenings Vloeimeganika (BVM) analises met behulp van CFX® en eksperimentele data. Die nuwe sentrifugale kompressor is ontwerp deur middel van 1-D en 3-D BVM analises met behulp van CompAero en CFX®. Die doel is om 'n kompressor te ontwerp wat die totale-tot-statiese drukverhouding maksimeer. Die grootte van die kompressor is beperk deur die geometrie van die gasturbine omhulsel. Aangesien die turbinerotor onveranderd sal bly, moet die insetdrywing, massa-vloeitempo en rotasiespoed dieselfde bly. Die eksperimentele opstelling is gebou en die numeriese resultate van die standaard kompressor is teenoor die eksperimentele resultate gevalideer. 'n Nuwe sentrifugale kompressor is ontwerp. Die totale-tot-statiese drukverhouding is verhoog van 2.50 tot 3.30 teen 'n rotasiespoed van 46 000 omwentelings per minuut. Die doeltreffendheid van die kompressor is verbeter van 63.8% tot 85.6%. Die insetdrywing van die nuwe kompressor ontwerp het met 1.6% afgewyk van die vasgestelde maatstaf, en met 1.3% van die numeriese data van die standaard kompressor.

Acknowledgements

I would like to express my appreciation and gratitude to the following persons for tagging along with me on my foreign Master studies:

- Lindi Strydom for all she has done for me to forget about a traumatic occurrence, and giving me strength to get back on the horse. My stay here with you has been unforgettable and I cannot thank you enough.
- My partner in crime Yueqian 'Leon' Zhang, for us working together like a well-oiled machine on the experimental work for over two years. Thanks for all the laughs and the good times at- and off campus.
- My mom, Marijke Hoogerboord, supplier of an occasional box with Dutch delights, who supported me in any possible way in both the good and the though times during my overseas journey. Her visit together with Claudi Stuurman gave me renewed motivation and drive to get to the end.
- My dad, Frank Luiten, for his support and help with all the troublesome administration related to studying abroad.
- My two brothers, Timon and Gunnar Luiten, who kept me updated and stayed strong while their big brother was away.
- All my friends who gave up their means, time and effort to come and visit me in South Africa. I want to thank Niek Schotanus for a great road trip, Daniel Tanbour for a good couple of days, Bart Fikkers for an excellent two weeks, and Harald Sluiter for multiple welcoming visits. My gratitude goes beyond measure.
- My uncle, Peter Hoogerboord, for knocking on my door and joining me on a good day off.
- Friends I met here in South Africa who introduced me to the world of rugby and braais.
- I express my deep appreciation to my study leaders Professor Theo von Backström, Mister Richard Haines and Doctor Johan van der Spuy

for their support, advice and guidance during the many meetings and discussions. Sincere thanks goes to Doctor Johan van der Spuy for the helpful inputs given on the computational work, and Professor Theo von Backström for providing financial means.

- Special thanks to Mister Richard Haines who's empirical expertise proved to be extremely valuable during the course of my thesis.
- Professor Garth Hobson from the Naval Postgraduate School in Monterey, California for his much appreciated help with problems related to computational fluid dynamics.
- Mr. Gerhard Lourens for his assistance with the control cabinet and the gas turbine testing software.
- To all the staff at the Mechanical and Mechatronic Engineering Department, the staff from the workshop and the staff in charge of the high performance cluster at Stellenbosch University.

Dedications

to Teun...

Contents

Declaration i

Abstract iii

Uittreksel iv

Acknowledgements v

Dedications vii

Contents viii

List of Figures xi

List of Tables xiv

Nomenclature xv

1 Introduction 1
- 1.1 Background and motivation . . . 2
- 1.2 Objectives and methodology . . . 3

2 Literature Study 4
- 2.1 Operating principle of a centrifugal compressor . . . 4
- 2.2 Impeller . . . 4
- 2.3 Vaneless radial passage . . . 13
- 2.4 Vaned diffuser . . . 17

3 1-D Centrifugal Compressor Design 23
- 3.1 Introduction . . . 23
- 3.2 Review of 1-D software . . . 24
- 3.3 Compressor bounds and target performance parameters . . . 25
- 3.4 Impeller . . . 25
- 3.5 Vaneless radial passage . . . 29
- 3.6 Vaned diffuser . . . 30
- 3.7 Compressor stage overall performance . . . 34

4 Centrifugal Compressor Numerical Analysis 36
4.1 Introduction . . . 36
4.2 Procedure for modelling the standard compressor . . . 36
4.3 Procedure for modelling the new compressor . . . 40
4.4 Computational flow generation . . . 45
4.5 Numerical analysis conclusion . . . 50

5 Experimental Setup 51
5.1 Introduction . . . 51
5.2 Performance model . . . 51
5.3 RGT 1S/60 gas turbine overview . . . 55
5.4 Experimental setup . . . 59
5.5 Data acquisition . . . 63
5.6 Data processing . . . 69
5.7 Results . . . 70

6 Compressor Performance Evaluation 71
6.1 Validation of the standard compressor CFD results . . . 71
6.2 Modelling results and discussion . . . 73

7 Conclusions and Recommendations 80
7.1 Conclusions . . . 80
7.2 Recommendations . . . 81

Appendices 83

A Numerical Analysis 84
A.1 Review of the 1-D software package . . . 84
A.2 Review of the 3-D software package . . . 88

B CompAero Performance Analysis Theory 90
B.1 Impeller work input coefficient prediction . . . 90
B.2 Impeller analysis loss coefficients . . . 93
B.3 Vaneless radial passage . . . 95
B.4 Vaned diffuser . . . 96

C Axial Flow Turbine Stage Efficiency Model 99
C.1 Step 1: profile loss coefficient estimation . . . 100
C.2 Step 2: estimating the overall loss coefficient . . . 101
C.3 Step 3: estimate the total loss coefficient . . . 103
C.4 Step 4: stage efficiency . . . 104

D Experimental Setup 105
D.1 Testing software . . . 105
D.2 Experimental procedure . . . 106

D.3 Calibration of the measurement instrumentation 108
D.4 Experimental data 109

E Numerical Analysis Process and Mesh Overview **112**
E.1 BladeGen™ user interface 112
E.2 Mesh details 113
E.3 y^+ values of the thesis compressors 118

List of References **120**

List of Figures

1.1 The SUNSPOT cycle as proposed by Kröger (2008) 2

2.1 Impeller geometry in the r-Z and r-θ plane 5
2.2 Impeller inlet velocity triangle 6
2.3 Impeller Mollier chart 7
2.4 Impeller throat velocity triangle 8
2.5 Inlet to throat Mollier chart 8
2.6 Impeller discharge geometry 9
2.7 Impeller tip trimming 10
2.8 Blade tip skew 11
2.9 Velocity triangle at the impeller tip 13
2.10 Sectional view of a vaneless radial passage 14
2.11 Vaneless radial passage Mollier chart 14
2.12 Vaned diffuser geometry in the r-θ plane and channel diffuser outline 18
2.13 Vaned diffuser velocity triangles 18
2.14 Vaned diffuser Mollier chart 19

3.1 Compressor bounds 26

4.1 CAD model of the impeller (a) and diffuser (b) 37
4.2 Meridional view of the standard compressor geometry 37
4.3 Meridional view of the standard compressor's computational domain 39
4.4 CAD model of the impeller (a) and diffuser (b) 41
4.5 Meridional view of the new compressor geometry 41
4.6 Meridional view of the new compressor's computational domain 42

5.1 Gas turbine cycle diagram 52
5.2 Sectional overview of the RGT 1S/60 gas turbine (Rover Gas Turbines Ltd, 1965*a*) 56
5.3 Sectioned view of the fuel pump (Rover Gas Turbines Ltd, 1965*b*) 57
5.4 Internal view of the temperature control unit (Rover Gas Turbines Ltd, 1965*b*) 59
5.5 Test bench setup 61

5.6 Boat throttler (a) and fuel sprayer (b) 62
5.7 Needle-valve system 63
5.8 Data instrumentation on the RGT 1S/60 64
5.9 Four static pressure taps in the conical inlet duct 66
5.10 Speed sensor and load cell principle (SCHENCK Pegasus GmbH, 1997) 67
5.11 PLC; main CPU and separate modules 68
5.12 Comparison of the start-up process of multiple runs 70

6.1 RGT 1S/60 total-to-static performance map 72
6.2 Total-to-static pressure ratio of the compressors 74
6.3 Total-to-total efficiency values of the compressors 74
6.4 Mach number of the standard compressor (a) and the new compressor (b) 75
6.5 Distorted flow in the through-flow passage of the standard compressor (a), velocity vectors at the diffuser inlet to exhibit the mismatch between the flow and the blade angle (b) 76
6.6 Low Mach region indicates recirculating flow at the suction side of the standard diffuser vane at 50% span at operating point . . . 76
6.7 Low velocity region at the main blade suction side at 50% span at the operating point 77
6.8 High Mach number flow at the diffuser inlet and throat at 50% span and operating point of the new compressor (a). The angle between the flow and the theta direction perpendicular to the leading and trailing edge of the vanes, i.e. velocity flow angle, shows recirculation along 50% of the suction side of the vane starting at the leading edge at 20% span (b) 78
6.9 Low Mach number region at the main blade suction side of the new impeller at 30% span at the operating point 78

A.1 Flow chart of the VDDESIGN design procedure 87

C.1 Turbine planes and velocity triangles (Saravanamuttoo *et al.*, 2001) 100
C.2 Gas outlet angles (Saravanamuttoo *et al.*, 2001) 101
C.3 Profile loss coefficient curve (Saravanamuttoo *et al.*, 2001) 102
C.4 Lambda function curve (Saravanamuttoo *et al.*, 2001) 103
C.5 Trailing edge thickness correction factor (Saravanamuttoo *et al.*, 2001) 104

D.1 ETA user interface 106
D.2 Experimental temperature values of the RGT 1S/60 at operating point 111
D.3 Experimental pressure values of the RGT 1S/60 at operating point 111

E.1 User interface of ANSYS® BladeGen™ 112

E.2 View of the new standard mesh by ANSYS® Meshing 113
E.3 Leading edge and trailing edge mesh of the standard diffuser by TurboGrid™ 114
E.4 Leading edge and trailing edge mesh of the new impeller by TurboGrid™ 114
E.5 Leading edge and trailing edge mesh of the new diffuser by TurboGrid™ 115
E.6 Top view of the new compressor coarse mesh by TurboGrid™ . . 116
E.7 Top view of the new compressor medium mesh by TurboGrid™ . 116
E.8 Top view of the new diffuser fine mesh by TurboGrid™ 116
E.9 Region of "bad" cells at the blade trailing edge of the impeller . . 117
E.10 y^+ values of the standard compressor using the SST k-ω model . . 118
E.11 Suction surface y^+ values of the new compressor using the k-ω model 119
E.12 Pressure surface y^+ values of the new compressor using the k-ω model 119

List of Tables

3.1 Impeller performance by CENCOM 28
3.2 Impeller work coefficients by CENCOM 28
3.3 Impeller loss coefficients by CENCOM 29
3.4 Vaneless radial passage performance by CENCOM 30
3.5 Flow data by VDDESIGN 31
3.6 Design point performance by VDDESIGN 32
3.7 Design point parameters by VDDESIGN 34
3.8 Compressor stage overall performance by CENCOM 35

4.1 Compressor dimensions 38
4.2 Mesh quality of the standard compressor (ANSYS® Meshing) . . 40
4.3 Compressor dimensions 42
4.4 Mesh settings 43
4.5 Mesh quality of the new impeller (TurboGrid™) 44
4.6 Mesh quality of the new diffuser (TurboGrid™) 45
4.7 Inlet boundary property values 47
4.8 Basic settings of the transient analysis 49

5.1 Rover Gas Turbines Ltd (1965*a*) performance specifications 52
5.2 General performance predictions of the RGT 1S/60 55
5.3 Conical inlet parameters 65

6.1 Compressor discharge conditions for experimental and CFD data at operating point 72
6.2 Overall compressor performance 73
6.3 Power input estimates of the standard and new compressor . . . 79

C.1 Turbine geometry 99
C.2 Velocity values and flow angles of the three turbine stages 101
C.3 Temperatures values of the three turbine stages 104

D.1 Experimental data of the standard compressor at operating point 110

E.1 Mesh dependency of the new compressor 115

Nomenclature

Constants

R	287 J/kg·K	

Symbols

A	Total blade passage area	$[\,\mathrm{m}^2\,]$
A_R	Area ratio	$[\,-\,]$
B	Fractional area blockage	$[\,-\,]$
b	Hub-to-shroud passage width	$[\,\mathrm{m}\,]$
C	Absolute velocity	$[\,\mathrm{m/s}\,]$
C_c	Seal carryover	$[\,-\,]$
C_p	Specific heat at constant pressure	$[\,\mathrm{J/kg \cdot K}\,]$
C_r	Contraction ratio	$[\,-\,]$
C_t	Seal throttling	$[\,-\,]$
c	Compressor, chord	$[\,-, \mathrm{m}\,]$
c_f	Friction coefficient	$[\,-\,]$
c_p	Static pressure recovery coefficient	$[\,-\,]$
D_{eq}	Equivalent diffusion factor	$[\,-\,]$
d_H	Hydraulic diameter	$[\,\mathrm{m}\,]$
E	Design effectiveness parameter	$[\,-\,]$
e	Boundary layer edge	$[\,-\,]$
f_{actual}	Actual fuel/air ratio	$[\,-\,]$
f_c	Correction factor	$[\,-\,]$
$f_{theoretical}$	Theoretical fuel/air ratio	$[\,-\,]$
H	Head coefficient	$[\,-\,]$
h	Enthalpy	$[\,\mathrm{J/kg}\,]$
I	Work input coefficient	$[\,-\,]$
i	Incidence angle $(\beta - \alpha)$	$[\,^\circ\,]$
K	Clearance gap swirl parameter, vaned diffuser stall parameter	$[\,-\,]$

K_0	Zero leakage swirl parameter, unguided vaned diffuser stall parameter	[−]
K_1	Correction coefficient, see Equation B.4.11	[−]
K_2	Correction coefficient, see Equation B.4.11	[ ]
k	Tip clearance	[m]
L	Mean streamline meridional length, dimensionless diffuser blade loading parameter	[m]
L_B	Vane mean streamline camberline length	[m]
Ma	Mach number	[−]
m	Meridional length	[m]
$\dot{m}$	Mass flow rate	[kg/s]
N	Number of actually performed timesteps, rotational speed	[−, RPM]
p	Absolute pressure	[Pa]
Q_h	Heat flux	[J/s]
R	Rothalpy, radius ratio (r_4/r_3)	[J/kg, −]
Re	Reynolds number	[−]
r	Radius	[m]
s	Specific entropy, pitch	[J/K, m]
T	Temperature	[K]
t	Turbine, trailing edge thickness	[−, m]
t_b	Blade thickness	[m]
t_d	Time duration	[s]
U	Blade speed (ωr)	[m/s]
V	Velocity	[m/s]
W	Relative velocity, work factor	[m/s, J]
w	Vane-to-vane passage width	[m]
X	Choke parameter	[−]
y^+	Dimensionless wall distance	[−]
z	Number of blades of vanes	[−]
z_I	Effective number of blades	[−]

Greek Letters

α	Flow angle with respect to tangent	[°]
α_C	Mean stream angle with respect to zenith axis	[°]
$\alpha\epsilon$	Compound flow rate coefficient	[−]
β	Blade angle with respect to tangent	[°]

γ	Specific heat ratio	$[-]$
Δ	Difference	$[-]$
Δ_t	Timestep	$[\mathrm{s}]$
δ	Boundary layer thickness, dimensionless pressure correction factor	$[\mathrm{m}, -]$
ϵ	Impeller mean streamline radius ratio (r_1/r_2)	$[-]$
η	Isentropic efficiency	$[\%]$
θ	Camber angle	$[^\circ]$
κ_m	Mean streamline curvature	$[\mathrm{rad/m}]$
λ	Tip distortion factor, temperature equivalent turbine loss coefficient	$[-]$
μ	Dynamic viscosity coefficient	$[\mathrm{kg/m \cdot s}]$
ν	Kinematic viscosity coefficient	$[\mathrm{m^2/s}]$
ρ	Density	$[\mathrm{kg/m^3}]$
σ	Slip factor	$[-]$
$\sigma\star$	Parameter to determine ϵ_{LIM}, see Equation B.1.5	$[-]$
τ	Torque	$[\mathrm{N \cdot m}]$
Υ	Turbine loss coefficient	$[-]$
ψ_2	Tip flow coefficient	$[-]$
ω	Rotation speed	$[\mathrm{RPM}]$
$\bar{\omega}$	Total pressure loss coefficient	$[-]$
$2\theta_C$	Diffuser divergence angle	$[^\circ]$

Superscripts

$\star$	Sonic flow condition

Subscripts

ad	Adiabatic
B	Blade
BL	Blade Loading
$bolt$	Diffuser bolts
DF	Disk friction
CH	Choke
CL	Shroud clearance gap
CM	Torque coefficient
COR	Corrected
CR	Critical Mach number

c	compressor
D	Diffuser
DIF	Diffusion
e	Boundary layer edge
FB	Full blades
HS	Hub-to-shroud
h	Hub
$Ideal$	Ideal value
i	Index for total pressure loss and work input coefficient
imp	Impeller
inc	Incidence
L	Leakage
m	Meridional velocity component
max	Maximum value
mix	After mixing at the impeller tip or diffuser discharge
PG	Passage
PS	Pressure surface
p	Polytropic
par	Parasitic
R	Recirculation, rotor
S	Stator
SB	Splitter blades
SEP	Separation
SF	Skin friction
SS	Suction surface
s	Shroud, stagnation point
TS	Total-to-total ratio
TT	Total-to-total ratio
t	Total thermodynamic condition
th	Throat
U	Tangential velocity component
VD	Vaned diffuser
v	Velocity
$wake$	Before mixing at the impeller tip or diffuser discharge
0	Impeller eye condition

1	Impeller inlet condition
2	Impeller tip condition
3	Diffuser inlet condition
4	Diffuser discharge condition

Auxiliary Symbols

$'$	Value relative to rotating frame of reference
-	Average of values
$\cdot$	Time derivative

Acronyms

AC	Alternate Current
APU	Axiliary Power Unit
CAD	Computer Aided Design
CENCOM	Centrifugal Compressor
CFD	Computational Fluid Dynamics
CPU	Central Processing Unit
DC	Direct Current
EGT	Exhaust Gas Temperature
ETA	Engine Test Automation
k-ϵ	Turbulence model
k-ω	Turbulence model
IGES	3-D computer model format
LC	Loss Coefficient
LPG	Liquefied Petroleum Gas
NC	Normally Closed
PLC	Programmable Logic Controller
RGT	Rover Gas Turbines
RMS	Root-mean-square
RPM	Revolutions Per Minute
SFC	Specific Fuel Consumption
SIZE	Preliminary compressor size
SST k-ω	Turbulence model
SUNSPOT	Stellenbosch University Solar Power Thermodynamic cycle
VDDESIGN	Vaned Diffuser Design
VR	Variable reluctance

1-D	One-dimensional
3-D	Three-dimensional

1. Introduction

The Department of Mechanical and Mechatronic Engineering at the University of Stellenbosch is currently involved in the evaluation and development of a number of different solar thermal power generating plant cycles. This includes the SUNSPOT (***S***tellenbosch ***UN***iversity ***S***olar ***PO***wer ***T***hermodynamic cycle). One of the aims of SUNSPOT is to integrate a central receiver heat exchanger into a gas turbine Brayton cycle. In order to investigate the pressure drop over the central receiver, an experimental gas turbine setup is required where a mockup of the SUNSPOT central receiver will be part of the gas turbine cycle.

This document involves the study of the Rover Gas Turbines 1S/60 (RGT 1S/60) gas turbine that will be used for the experimental gas turbine setup, focussing mainly on the potential performance improvement of the centrifugal compressor to account for possible pressure loss in the central receiver. The aim of this thesis is to evaluate the standard compressor of the RGT 1S/60 by comparing the experimental data with three-dimensional (3-D) numerical analyses. Following this a preliminary one-dimensional (1-D) design of a new compressor with improved performance will be conducted, followed by further 3-D numerical flow analyses.

The 1-D analysis is performed on a mean streamline through the centrifugal compressor, based on theory and empirical loss models proposed by Aungier (2000). The software package CompAero [developed by Aungier (2000)] is utilized for the 1-D analysis of the new compressor, which is reviewed in Appendix A.1 and further discussed in Chapter 3 and Appendix B. The ANSYS® software platform by ANSYS Inc. is utilized for the 3-D Computational Fluid Dynamic (CFD) analysis. The CFD software platform is reviewed in Appendix A.2 and the numerical modelling process is further discussed in Chapter 4.

Besides the centrifugal compressor performance and the setup of a gas turbine testing facility, all SUNSPOT related components or investigations fall outside the scope of this thesis.

1.1. Background and motivation

The Department of Mechanical and Mechatronic Engineering at the University of Stellenbosch is currently involved in evaluating and developing the SUNSPOT cycle proposed by Kröger (2008), which is an efficient and appropriate cycle for electricity generation in South Africa. A schematic of the SUNSPOT cycle is shown in Figure 1.1.

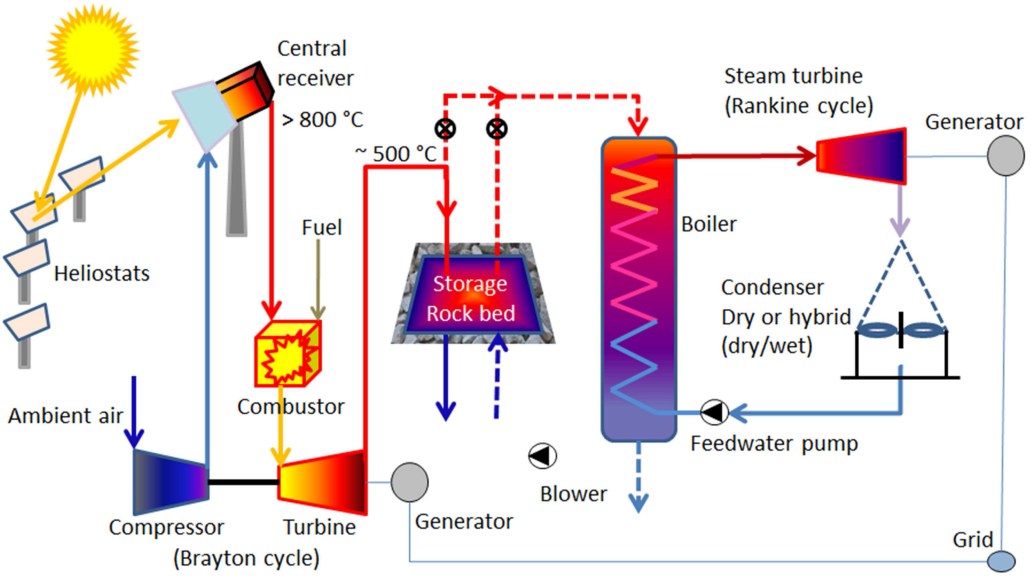

Figure 1.1: The SUNSPOT cycle as proposed by Kröger (2008)

The SUNSPOT concept is based on Concentrating Solar Power (CSP) technology where sun tracking mirrors (heliostats) concentrate the solar radiation onto a central receiver heat exchanger. In the SUNSPOT cycle ambient air is compressed and transported to the central receiver where the compressed air is heated to more than 800°C. The hot air then flows through a turbine which drives the compressor and a generator that provides electricity to a grid. The SUNSPOT cycle ducts the air leaving the turbine into a packed rock bed thermal storage facility for electricity generation after sunset.

The gas turbine appointed for the test setup, the RGT 1S/60, is designed to drive a car. Introduced in the late 1950s, the RGT 1S/60 was considered a possible alternative for conventional internal combustion engines in cars, primarily due to its advantageous weight to power ratio. However, the technical success of powering a car with a gas turbine did not prevent the concept from failing. The primary gas turbine properties such as the

high operating speeds, high temperatures, and inefficiency while idling or accelerating were the Achilles heel of the concept. Although the gas turbine is specifically designed for automotive use, the RGT 1S/60 was utilized as Auxiliary Power Unit (APU) on board aircraft, ships and hovercraft. In addition the RGT 1S/60 was used as a power source for some ground applications like water pumps. The RGT 1S/60 gas turbine was available for research and was therefore selected for the central receiver mockup research.

1.2. Objectives and methodology

This thesis was conducted with the objective to analyse, assess and redesign the centrifugal compressor of the RGT 1S/60 to attain a better performing compressor stage. Because the turbine design of the RGT 1S/60 was to be kept unchanged, it was of importance that the input power, or torque, would remain the same. Therefore an increase in pressure ratio and an improved efficiency value were design targets. The objectives were achieved by following the methodology that is itemized in chronological order below:

- Build an operational test setup for the RGT 1S/60 gas turbine that is controllable from a control room. Provide calibrated measuring equipment that allows data recording, and ensure that the operational setup is suitable for future research.
- Perform several experimental runs with the RGT 1S/60 setup to record data and to check for malfunctions, possible future problems, accuracy, repeatability and reliability.
- Use the 1-D software platform CompAero, based on the mean stream surface analysis theory by Aungier (2000), to perform a preliminary centrifugal compressor design that conforms to all relevant compressor parameters.
- Model the geometries of the standard and preliminary 1-D design centrifugal compressor in a Computer Aided Design (CAD) platform. Autodesk® is the CAD software package used for both components.
- Export the standard compressor geometry and the preliminary 1-D design geometry into the CFD platform to conduct 3-D flow analyses. ANSYS® is used as the CFD software package, utilizing the CFX® solver.
- Validate the numerical results of the standard compressor with the experimental results, and compare the results of the 1-D and 3-D design of the new centrifugal compressor design.
- Finalization of the new centrifugal compressor design
- Conclude the research and give recommendations for future work, related to both the experimental test setup and the new compressor design.

2. Literature Study

The geometry and operating principles of the centrifugal components relevant to this thesis are discussed in detail in the following section.

2.1. Operating principle of a centrifugal compressor

The centrifugal compressor stage consists of a stationary housing containing a rotating impeller which imparts a high circumferential velocity to the airflow. Following this a radially expanding area diffuses the air either vaneless or with a vaneless passage followed by vanes. The diffusion process decelerates the flow resulting in a rise in static pressure. This area is referred to as the diffuser.

Air is continuously sucked into the impeller eye and revolved at high velocity by the blades on the impeller disk. A radial pressure gradient at any given point in the fluid flow results in a corresponding centrifugal acceleration, consequently increasing the static pressure from the eye to the tip of the impeller (Boyce, 2002). The remainder of the static pressure rise occurs in the diffuser, where the stationary diffuser passages convert the kinetic energy of the airflow into static pressure by reducing the high velocity at the impeller tip to velocity values close to those at the impeller eye. The stagnation pressure will decrease somewhat due to friction losses in the diffuser. Usually approximately half of the total pressure rise in the centrifugal compressor is achieved in the impeller, and the other half in the diffuser (Saravanamuttoo *et al.*, 2001).

2.2. Impeller

The air enters the impeller from the inlet duct into the impeller inducer, identified as the region between the hub and the shroud (Figure 2.1). This flow is typically assumed to be uniform and axial (Dixon, 2005), as exhibited in Figure 2.2. The air then flows into the inducer which guides the

airflow into the blade passages where the rotating impeller blades energise the airflow, and thus increase the total enthalpy. The increase in radius from impeller eye to tip gives rise to an increase in the angular momentum of the fluid until the flow is discharged at the tip of the blade.

The impeller blades are exposed to a higher static pressure on the forward face of the impeller blade than on the back face of the blade, creating a pressure gradient over the blade. Because the centrifugal compressors used in gas turbines usually do not have a shroud, a small clearance gap between the impeller and the housing is inevitable. This gap causes air to flow over the edge of the blade. Since this naturally results in an efficiency loss, the clearance gap must be kept to a minimum.

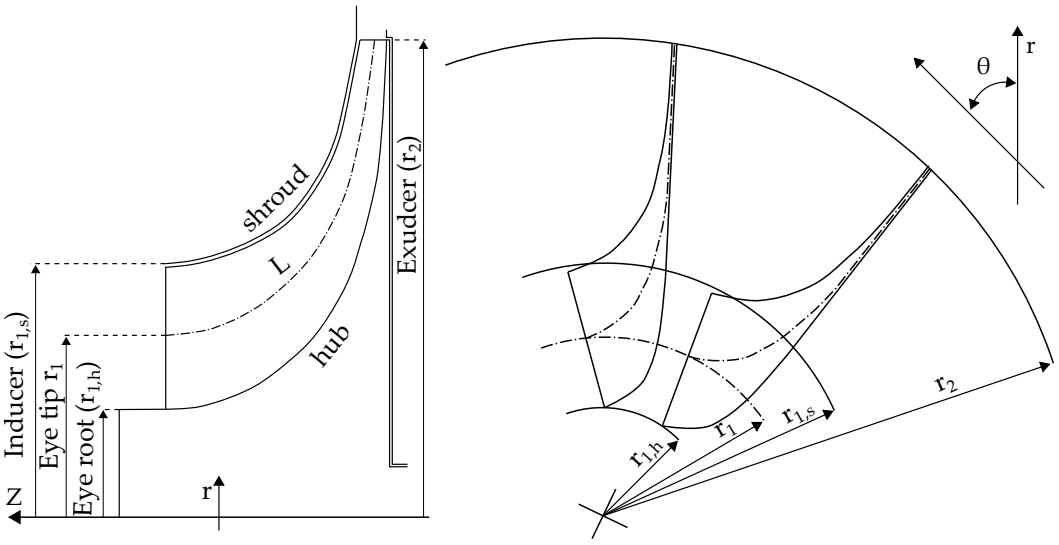

Figure 2.1: Impeller geometry in the r-Z and r-θ plane

2.2.1. Impeller operating principle

The total work coefficient of the mean stream surface (I) is the dimensionless work factor of the impeller and is expressed in Equation 2.2.1. The individual work coefficients (I_B, I_{DF}, I_L, I_R) are discussed in Appendix B.1.

$$\begin{aligned} I &= \left(h_{t,2} - h_{t,1}\right)/U_2^2 \\ &= I_B + I_{DF} + I_L + I_R \end{aligned} \tag{2.2.1}$$

The impeller analysis is conducted in the rotating frame of reference. The known absolute flow conditions at the inlet are used to acquire the relative

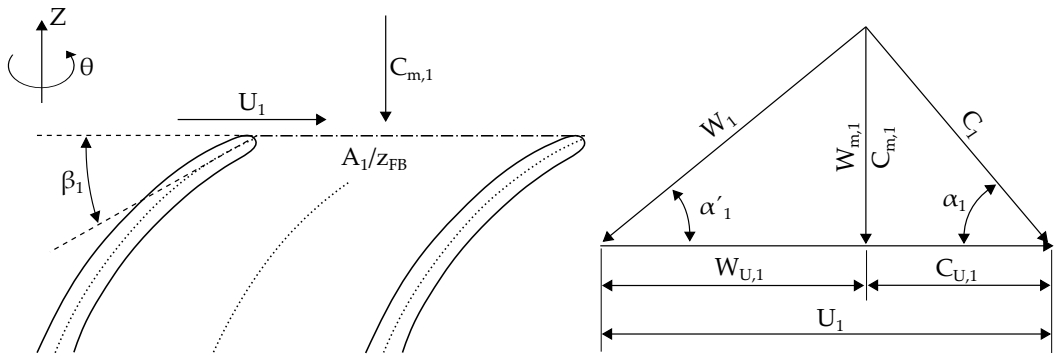

Figure 2.2: Impeller inlet velocity triangle

velocities and total enthalpy at the inlet (Equation 2.2.2). Since static enthalpy is identical in both frames of reference, the relative total temperature and pressure at the tip can be calculated. Because rothalpy (R) is conserved in the rotating frame of reference, the relative total enthalpy at the impeller discharge can be determined (Equation 2.2.3), which is used to calculate the isentropic discharge total conditions.

$$h'_{t,1} = h_{t,1} - U_1 C_{U1} + U_1^2/2 \tag{2.2.2}$$

$$h'_{t,2} = h'_{t,1} + \left(U_2^2 - U_1^2\right)/2 \tag{2.2.3}$$

Furthermore the discharge relative total pressure is given by:

$$p'_{t,2} = p'_{t,2(ideal)} - f_c \left(p'_{t,1} - p_1\right) \sum_i \bar{\omega}_i \tag{2.2.4}$$

where $\bar{\omega}$ is the total loss coefficient of the impeller. The individual loss coefficients are discussed in Appendix B.2

The thermodynamic state analysis of the impeller is summarised by a Mollier chart (Figure 2.3).

2.2.2. Geometric parameters

The various geometric parameters that are of importance in the design process of a centrifugal impeller are discussed in the following section.

2.2.2.1. Impeller throat

The throat of the impeller is the cross section area where distance between the leading edge of the aft main blade (regarding the impeller rotation di-

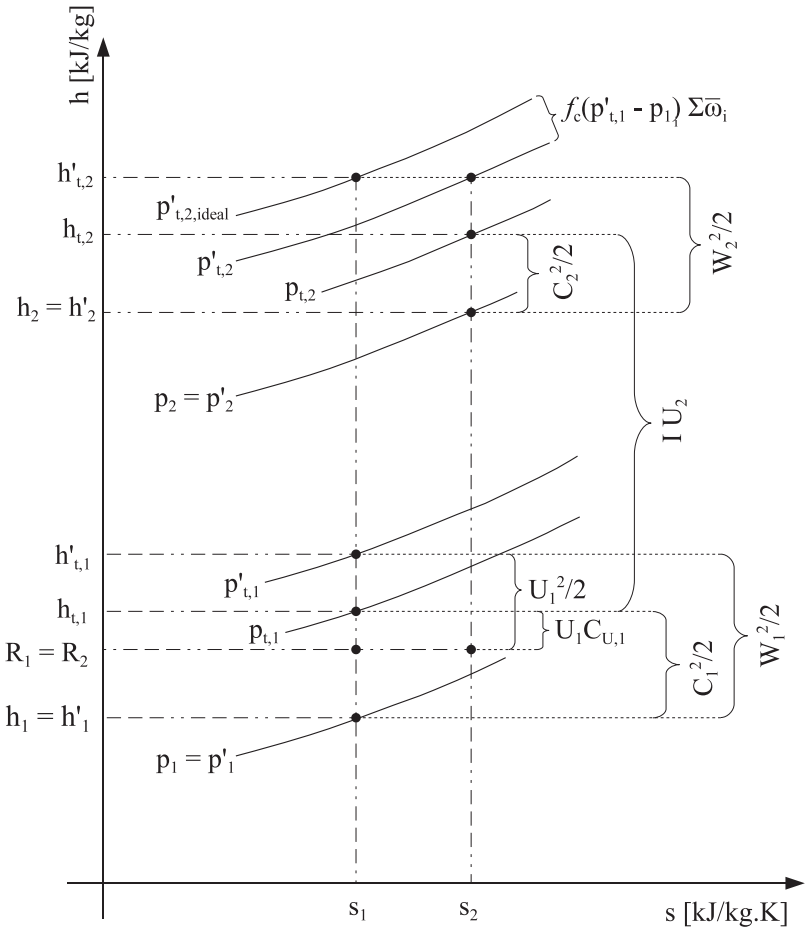

Figure 2.3: Impeller Mollier chart

rection) to the surface of the adjacent blade is a minimum (Figure 2.4). The throat of the impeller determines the choke margin of the impeller. The impeller inlet to throat Mollier chart in Figure 2.5 summarises the thermodynamic state of the throat.

The process between the inlet and throat is assumed to be isentropic. The impeller rotational speed is responsible for a rise in total enthalpy and pressure. Methods to calculate impeller choke and aerodynamic blockage are described in Appendix B.2.

2.2.2.2. Blade discharge geometry and blade loading

An impeller discharge geometry sketch is provided in Figure 2.6 as a reference. The blade discharge angle defines three different blade types. Impellers with a discharge angle $\beta_2 = 90°$ are categorised as radial blades. The term backward-swept is used to describe blades with $\beta_2 < 90°$, and blades

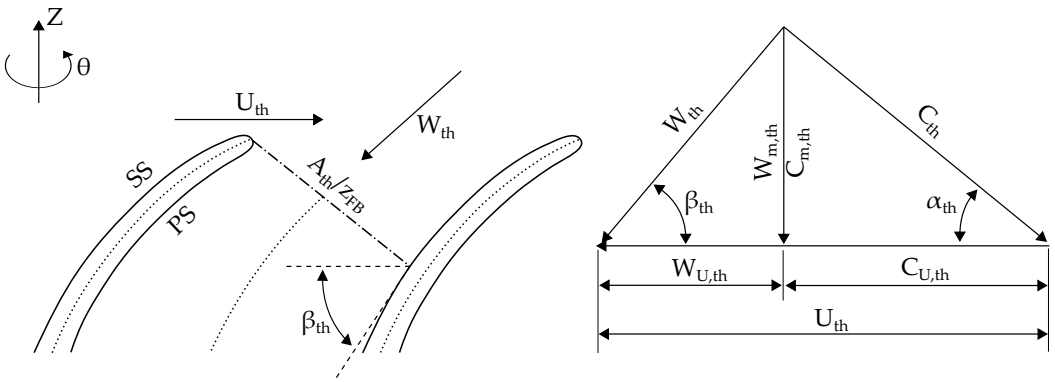

Figure 2.4: Impeller throat velocity triangle

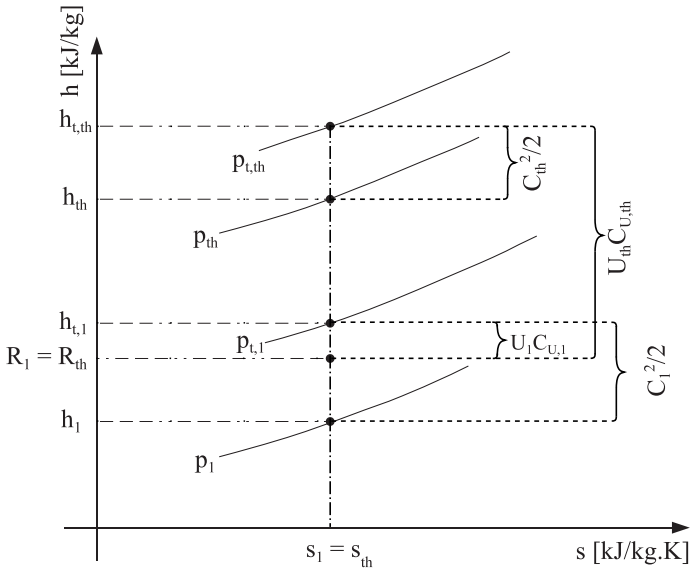

Figure 2.5: Inlet to throat Mollier chart

with $\beta_2 > 90°$ are referred to as forward-swept blades.

The various discharge blade angles have different head-flow rate characteristics, and each have their particular advantage or drawback. For example, radial blades are not subjected to high bending stresses but they do result in a relatively narrow surge margin. The backward-swept blades experience more complex bending stresses but do manage to widen the surge margin and because of the lower kinetic energy transfer a low diffuser inlet Mach number (Boyce, 2002). Forward-swept blades exhibit high-energy transfer at the cost of a high-diffuser inlet Mach number, complex bending stresses, and the narrowest surge margin of all configurations (Boyce, 2002).

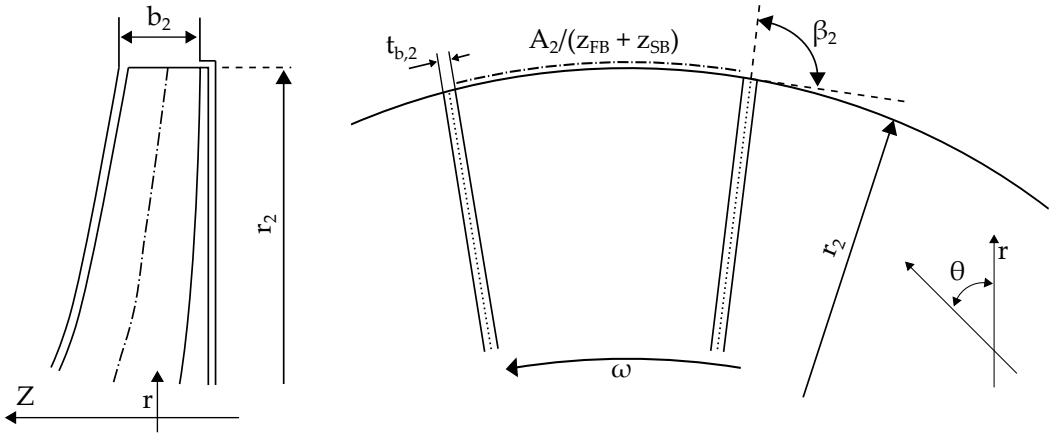

Figure 2.6: Impeller discharge geometry

Backward-swept blades are frequently used in impeller design due to their powerful effect on stage stability. This does however reduce the amount of kinetic energy that is transferred to the fluid and ultimately the net work output of the impeller. As a result of the reduced work factor at increasing back-sweep angles, the impeller characteristic of work versus mass flow and pressure ratio shows a steeper feature, indicating the importance of achieving the best performance when designing at the operating point. According to Came and Robinson (1998) a common back-sweep angle is 30° to balance the factors that affect the stage stability and impeller stress levels.

The number of blades directly affects the blade loading and how well the fluid follows the blade suction surface. A larger number of blades will result in a low blade loading and fluid flow that closely follows the blades. A smaller number of blades will cause the opposite; the flow will tend to separate from the suction surfaces of the blades, introducing a large exit velocity gradient.

2.2.2.3. Splitter blades

The influence of splitter blades on the velocity and pressure field in a centrifugal impeller was investigated by Kergourlay *et al.* (2007). The author observed both negative and positive effects on the impeller characteristics. The head rise increased; largely due to the increased slip factor as a result of improved conduction of the flow. The author noticed no efficiency increase because the losses attributable to the inclusion of the splitter blades outweighed the increase in head.

2.2.2.4. Impeller trimming

Centrifugal impeller blade trimming is widely used by designers to adjust a single impeller design to a series of flow characteristics. Engeda (2007) analysed the effect of impeller exit width trimming on the performance of a centrifugal compressor, which is done by narrowing the impeller flow passage depth (Figure 2.7). They observed improved impeller efficiency as a result of impeller tip trimming. Engeda (2007) also noticed that trimming the impeller reduces the tangential velocity component, resulting in an increase of the impeller discharge flow angle in the relative coordinate system. However, impeller trimming exhibits a decrement in stage head coefficient and a decrease in work factor.

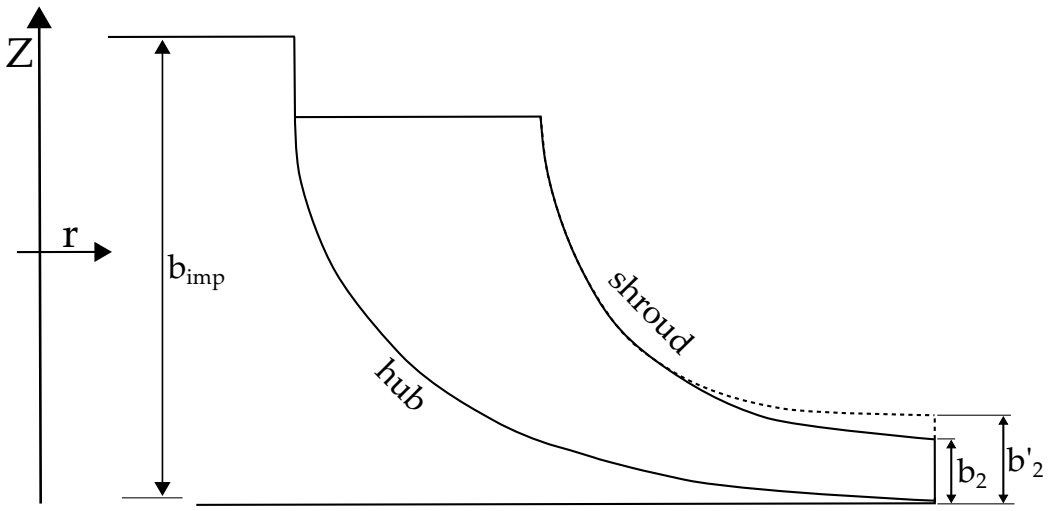

Figure 2.7: Impeller tip trimming

2.2.2.5. Blade tip skew

Introducing a blade angle variation at the impeller tip between the hub and the shroud is known as blade skew. This impeller tip configuration is considered appealing when attempting to re-distribute the fluid flow at the impeller discharge. The acute angle of the impeller tip is either positive or negative relative to the direction of rotation; negative skew is when the hub point leads and positive skew is when the shroud point leads (Figure 2.8).

Arunchalam *et al.* (2008) investigated blade skew angles of +45° and -45° relative to a 0° skew case. Results show an expected change in flow angle distribution from hub to shroud. Where positive skew transferred a higher energy to the air flow consequently increasing the tangential absolute flow

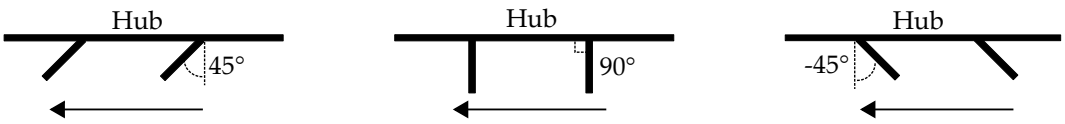

Figure 2.8: Blade tip skew

velocity, the negative skew case showed a reduction in tangential component of the absolute velocity at the impeller discharge. Hence positive skew improved the pressure ratio and efficiency, while negative blade skew reduced the pressure ratio significantly for a larger stall margin.

2.2.3. Aerodynamic parameters

The various aerodynamic parameters that are of importance in the design process of a centrifugal impeller are discussed in the following section.

2.2.3.1. Slip factor

The fluid flow angle at the impeller tip deviates from the impeller's blade angle, this phenomenon is called slip. The predominant reasons for the flow deviation are the centrifugal forces on the fluid and the inertia of the flow (Boyce, 2002). The airflow is not completely guided by the blades when it diffuses in the radial direction, as a result the flow on the centrifugal plane is reluctant to follow the rotational movement of the impeller. Hence the fluid elements are induced to flow closer to the pressure surface of the blade creating a higher pressure and low velocity. However a low pressure region with high velocity flow is observed at the suction side of the blade. Following this the pressure gradient of the two blade surfaces at the impeller tip cause a circulation in the direction of rotation. Consequently a velocity gradient arises at the impeller discharge that induces a net change in the flow discharge angle. Therefore the airflow is restricted from gaining the discharge whirl velocity equivalent to the rotational speed of the impeller. Hence, a slip factor is introduced to accommodate for a reduced discharge whirl velocity which affects the net power output of the centrifugal compressor (Equation 2.2.5).

$$\sigma = \frac{C'_{w2}}{C_{w2}} \tag{2.2.5}$$

2.2.3.2. Secondary flow

Secondary flows are strong circulatory vortex flows that are observed in the impeller on the suction side of the blade. These flows are undesirable and are accountable for slip, flow non-uniformity and head loss. It is believed

that the secondary flows can be suppressed by reducing the pressure gradient across the blade by introducing blade skew at the impeller tip (Saravanamuttoo *et al.*, 2001). However, designers often take preventive measures by employing hardware modifications that serve as guiding or disruptive elements, although these are actually workarounds that might also negatively effect the performance of the centrifugal compressor.

2.2.3.3. Leakage

A pressure gradient over the impeller blade in combination with an inevitable clearance between the casing and the impeller allows for fluid to flow from one side of a blade to the other, otherwise referred to as leakage. Besides decreasing the flow discharge angle, leakage reduces the energy that is transferred from the impeller to the fluid.

Eum *et al.* (2004) investigated the effect of tip clearance on the through-flow and performance of a centrifugal compressor by varying the tip clearance. The author shows that the tip leakage flow blocks the flow passage. As the tip clearance increases, Eum *et al.* (2004) noted that the total-to-total pressure ratio decrement becomes greater. Yet when the tip clearance is small, the decrement decreases slightly in the passage between the leading edge of the main blade and leading edge of the splitter blade. Moreover Cumpsty (1989) noticed that the tip leakage flow reduces the secondary flow when the tip clearance is very small.

Due to the significant effect of tip clearance on the work of the impeller, it has to be included when accurate impeller analyses is required. Shum *et al.* (2000) concluded that due to the inviscid nature of leakage flow and the thin impeller shroud tip, a limited number of nodes are required for tip clearance simulation in CFD.

2.2.3.4. Impeller discharge flow conditions

The effective discharge area is mostly dependent on the thickness of the boundary layer, which increases as the flow extends radially. Therefore the total effective discharge area is reduced when the flow reaches the impeller tip. As a result the relative and absolute velocities are affected, hence changing the impeller discharge velocity triangles (Figure 2.9).

Came and Robinson (1998) noted that the tip width influences the absolute flow angle at the impeller tip discharge (α_2), consequently affecting the design of the vaned diffuser inlet, and affecting mixing and boundary layer losses. For instance a too low α_2 results in a shallow spiral flow through the vaneless radial passage hence increasing boundary layer growth and

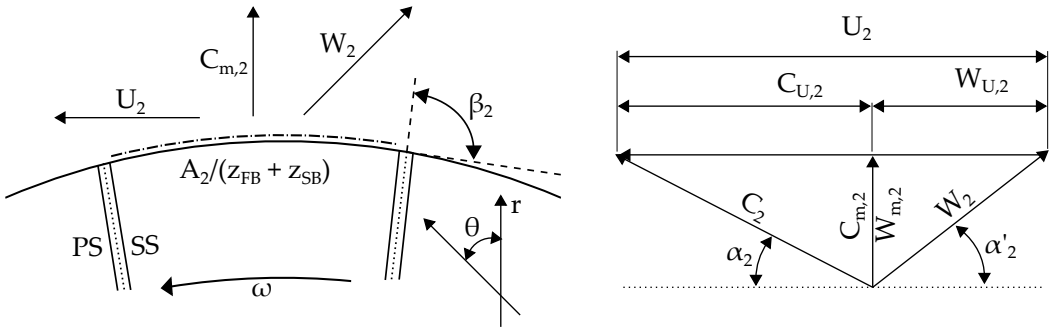

Figure 2.9: Velocity triangle at the impeller tip

affecting vaned diffuser inlet design. Furthermore a high α_2 causes the mixing to increase because of dissimilar radial velocities in the wake and core flows. The authors find a range of 17° <α_2<21° to provide appropriate limits. A similar range is suggested by Aungier (2000) who noted that successful vaned diffuser designs will generally make use of inlet blade angles between $16° \leq \beta_3 \leq 22°$.

2.3. Vaneless radial passage

The radial gap is acknowledged as an important design parameter that influences pressure ratio, efficiency, mass flow range, blade loading, centrifugal compressor sizing, and even noise emissions.

2.3.1. Operating principle

The highly distorted and heterogeneous impeller discharge flow causes the discharge static pressure to vary, and gives rise to shock waves due to local speeds in the sonic region. The function of the vaneless radial passage is to reduce the Mach number and relax the flow to lessen the likelihood of shock waves and excessive static pressure variation in the diffuser. Figure 2.10 serves as a reference while the workings of a vanelss radial passage is further described.

The vaneless radial passage diffusion is effected by controlling the radial- and swirl velocity component, the former is reduced because of the increased radius and the latter is governed by an increased flow area. No work is added to the flow through the vaneless radial passage, the total pressure decreases as a result of losses in the flow passage; hence the increase in enthalpy. The adiabatic flow through the vaneless radial passage is summarised in a Mollier chart (Figure 2.11).

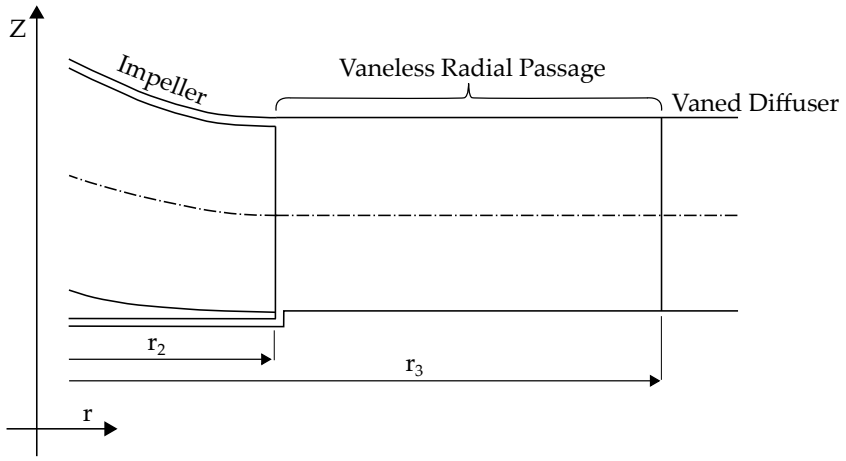

Figure 2.10: Sectional view of a vaneless radial passage

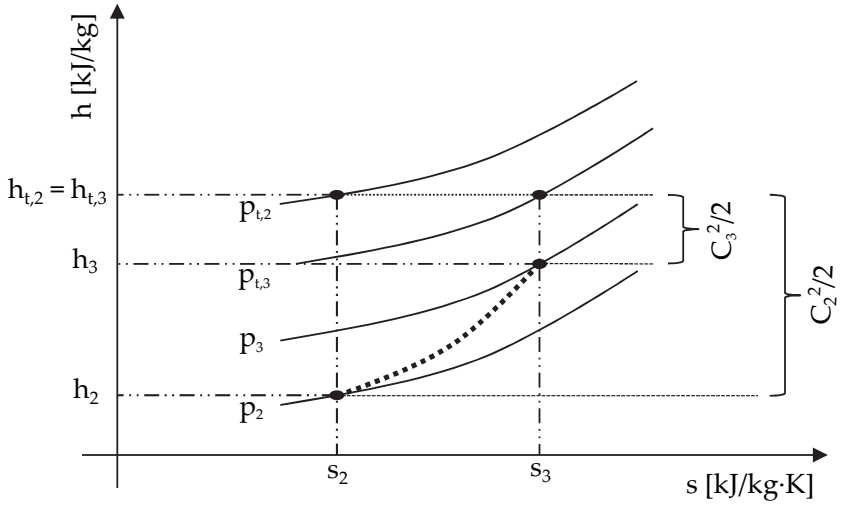

Figure 2.11: Vaneless radial passage Mollier chart

2.3.2. Impeller-diffuser interaction

The use of a vaned diffuser affects the flow discharge conditions of the impeller due to interaction of the flow fields. This interaction between the flow fields affects the performance of both the impeller and diffuser.

2.3.2.1. Interaction effect on the impeller

The effect on the performance of the impeller is investigated by various researchers. Shum *et al.* (2000) observed a small decrease in both static and total pressure at the impeller discharge when the diffuser vanes were positioned close to the impeller. An increase in unsteadiness associated with the tip-leakage flow was responsible for the change in blockage and loss in

the impeller discharge flow. Shum *et al.* (2000) stated that the impeller performance is prone to interaction influence and can be significantly affected. Nevertheless, according to Ziegler *et al.* (2003*b*) the slip factor in the impeller is hardly affected by the diffuser geometry.

Anish and Sitaram (2009) noticed that the efficiency of the impeller is the highest when the diffuser vane is furthest away, and the flow is most distorted when the diffuser vanes are closer. The author did however observe that the effects on the impeller do not penetrate deep into the flow passage because the disturbances are only evident in the last 10% of the impeller flow. However Ziegler *et al.* (2003*b*) claimed the opposite by investigating the effect of the vanes on the impeller flow. They observed a significant reduction of the wake region at impeller exit when a vaned diffuser was located far from the impeller tip. Furthermore a smaller but still noticeable decrease of wake occurs by positioning the vaned diffuser closer to the impeller tip. The authors therefore conclude that small radial gaps improve pressure recovery while hardly affecting the impeller efficiency.

2.3.2.2. Interaction effect on the diffuser

The flow distortions such as span-wise variation of the flow angle and circumferential unsteadiness are considered most influential on the performance of a vaned diffuser. One of the earlier works on interaction by Inoue and Cumpsty (1984) showed that the circumferential distortion from the impeller weakened relatively quickly and had only trivial effects on the flow in the vaned diffuser passage.

Kritley and Beach (1992) argued that span-wise variation of flow angle at the impeller tip has a more notable influence on the diffuser performance than circumferential unsteadiness in the flow. Because of this span-wise flow non-uniformity, conditions of incipient flow reversal and flow separation are revealed at the hub and shroud respectively (Ubaldi *et al.*, 1998). Moving downstream both circumferential and span-wise flow distortions are reduced by an intense mixing process, although Ubaldi *et al.* (1998) distinguished traces of impeller distortion flow still evident at a distance of approximately 10% of the impeller radius. Corresponding observations were made by Cukurel *et al.* (2010), who also observed that the circumferential variations are highest for the hub plane, and decrease towards a lesser magnitude at the shroud plane.

Although the impeller distortions are still distinguishable downstream in the diffuser, Shum *et al.* (2000) concluded that the diffuser performance is relatively insensitive to interaction, even if the diffuser vane is located close to the impeller tip. Boncinelli *et al.* (2007) concurs that the flow unsteadi-

ness at the tip of an impeller only marginally affects the stage performance. This result corresponds with the hypothesis by Ziegler *et al.* (2003*b*) who also claimed that a strong vortex in the diffuser throat would help prevent separation at the pressure side of the vane.

Shum *et al.* (2000) confirm that the effect of the circumferential distortion on the vaned diffuser was negligible. Shum *et al.* (2000) also stated that the non-uniform flow attributable to unsteadiness from the upstream impeller has an insignificant effect on the pressure recovery in the diffuser. They do however note that this might differ for other centrifugal compressor configurations, e.g. a different radial gap ratio or blade to vane number.

2.3.3. Optimum radius ratio range

Anish and Sitaram (2009) claim that there is an optimum impeller diffuser gap to obtain the highest static pressure rise. This is supported by an investigation of different types of diffusers at different radii (r_3/r_2), showing a maximum efficiency for all types of diffusers at their mean 1.10 radius ratio test. When the vanes are positioned further away from the impeller the efficiency drops marginally. Besides the flattening efficiency curve as the radius ratio increases, Anish and Sitaram (2009) also noted that the vaned diffusers show a higher energy coefficient and static pressure recovery at design flow rate at the 1.10 radius ratio, which is believed to be resultant of better flow guidance and more efficient flow deceleration. The radius ratio of 1.05 is considered too close for vaned diffusers indicating a lower static pressure rise (Anish and Sitaram, 2009).

Reduced blockage (B) and an improved slip factor (σ) are observed when the radial gap is small. However, if the diffuser vanes are positioned too close to the impeller, the penalty of increased losses would outweigh the benefits from reduced blockage and slip (Shum *et al.*, 2000). Hence Aungier (2000) recommends a vaneless radius ratio between 1.06 and 1.12. The lower limit allows for blade wakes to decay and the flow to smooth out, the upper limit prevents high losses in the vaneless passage due to low-flow angles and high Mach numbers. Aungier (2000) suggests that the vaneless radial passage ratio should be the smallest possible quantity if the Mach numbers allow it.

Shum *et al.* (2000) investigated different radial gaps while leaving the geometry of the vane and the area ratio unchanged. In their research the largest radius ratio indicates the highest total-to-total and total-to-static pressure ratio. They show that a higher pressure ratio can be achieved by reducing blockage, losses, and slip. Results indicate that the pronounced effect of increase in loss surpasses the decreased slip and reduced blockage when the

vanes are located close to the impeller tip. A radial length ratio of 1.075 caused a peak in static and total pressure ratio that marginally drops when further increased to 1.092.

Shum *et al.* (2000) claims that a trade-off between loss, blockage, and slip leads to an optimum radius ratio between 1.05 and 1.09. Clements and Artt (1987) recommend a slightly shifted radius ratio range between 1.06 and 1.10 which they consider is the optimum.

According to Saravanamuttoo *et al.* (2001) the chances of shock wave losses and excessive circumferential variation in static pressure are higher when the vanes are located close to the impeller tip. However, Ziegler *et al.* (2003*b*) recommend smaller radial gaps and found their optimum range between 1.04 and 1.06, though they do emphasize that it is dependent on the centrifugal compressor configuration. The essence behind their investigation is proving that the flow configuration in each diffuser passage can be optimized by adapting the vaneless radial passage length.

Ziegler *et al.* (2003*a*) recommend a smaller radial gap after investigating several radial gap ratios between 1.04 and 1.18. Ziegler *et al.* (2003*a*) noticed a more homogeneous flow field at the diffuser vane discharge when the vaneless radial passage ratio is small, indicating a better diffusion, and the total pressure ratio proved significantly higher at the same mass flow rate with a 1.04 radial gap compared to a 1.18 radius ratio.

2.4. Vaned diffuser

Since two thirds of the total losses in a centrifugal compressor occur in the diffuser, the stage efficiency is highly reliant on the diffuser (Anish and Sitaram, 2009). In many applications of the centrifugal compressor the geometry is constrained and therefore requires a very compact design. For instance the size of the compressor housing can limit the dimensions of the diffuser and reduce the potential pressure recovery. The advantage of a vaned diffuser is the ability to eliminate the swirl of the fluid at a high rate, thereby reducing the flow path length and evidently the discharge radius. Figure 2.12 and Figure 2.13 serve as a reference while the workings of a radial vaned diffuser are further described.

2.4.1. Vaned diffuser theory

The diffusion process for subsonic flow can be shown by the principle of mass flow conservation (Equation 2.4.1). As a result of the slow area expansion, the absolute velocity reduces and presuming the density remains

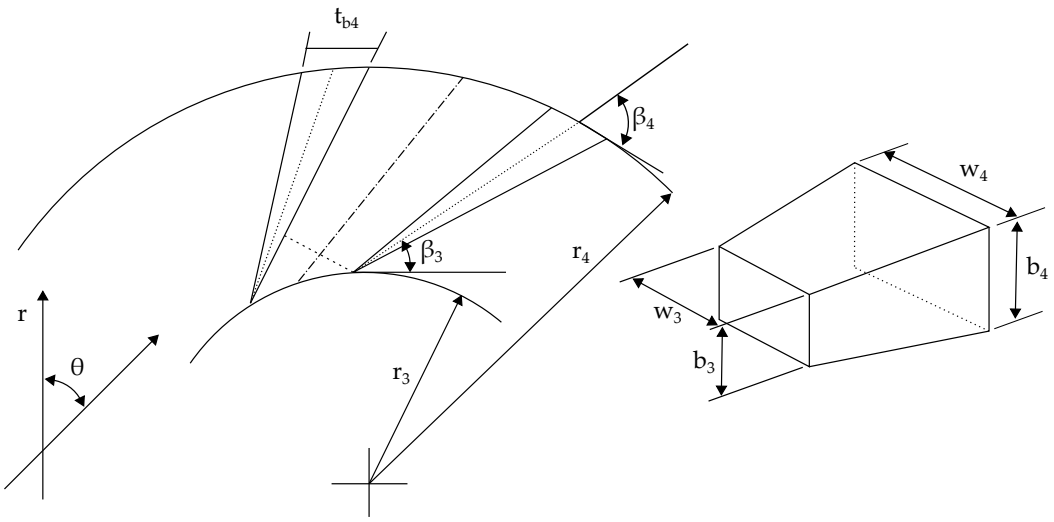

Figure 2.12: Vaned diffuser geometry in the r-θ plane and channel diffuser outline

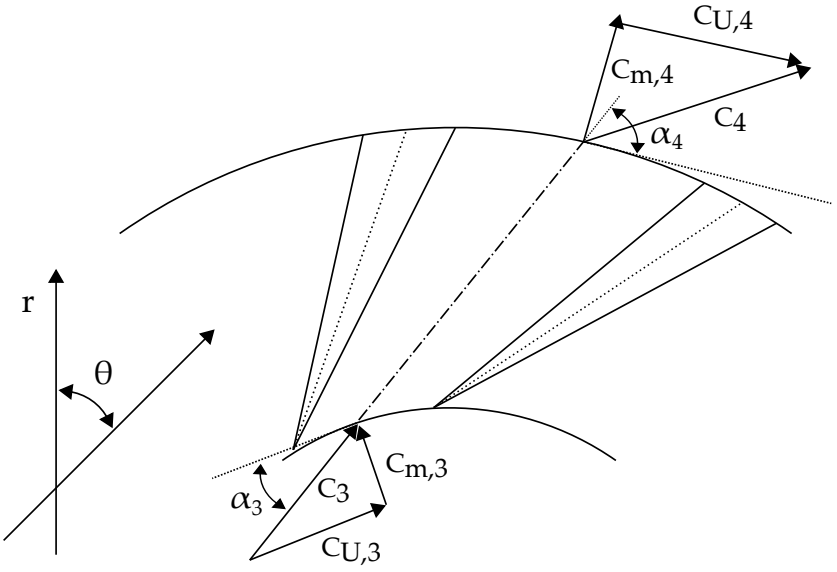

Figure 2.13: Vaned diffuser velocity triangles

unchanged the area expansion decreases the kinetic energy by converting it into static pressure. The kinetic energy term of the stagnation pressure at the diffuser outlet has to be as small as possible for simplified and more efficient combustion (Saravanamuttoo *et al.*, 2001).

$$\dot{m}_{in} = \dot{m}_{out} = \rho_3 A_3 C_3 = \rho_4 A_4 C_4 \tag{2.4.1}$$

Similar to the vaneless diffuser no energy is added to the fluid flow, there-

fore the total enthalpy remains unchanged, and the process is assumed adiabatic because of the losses accounting for the decrease in total pressure. The thermodynamic state of the diffusion process is discussed in Appendix B.4 and is summarised by the Mollier chart in Figure 2.14.

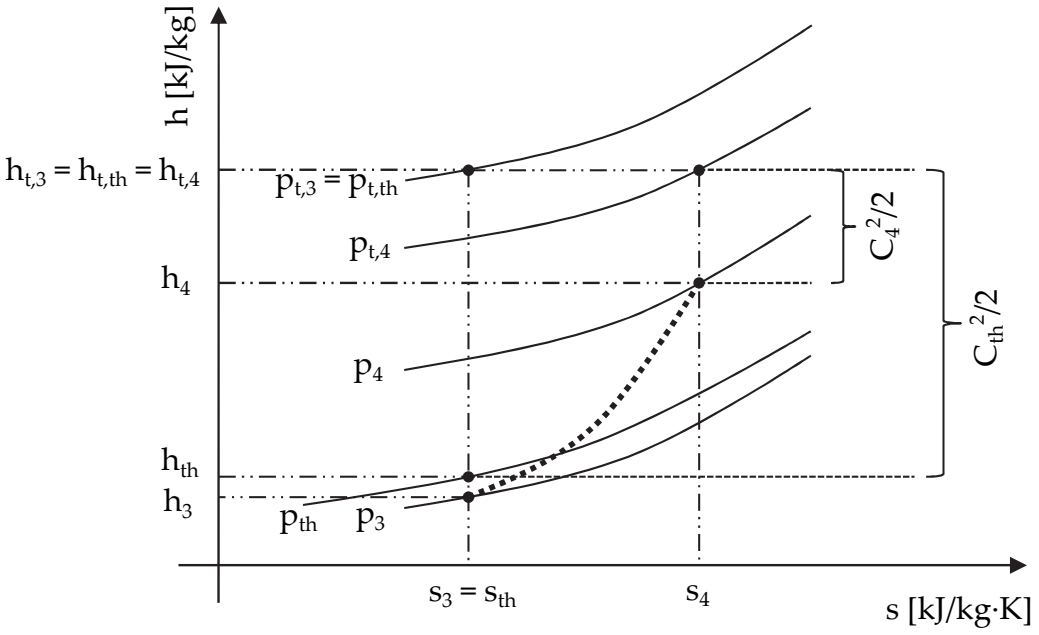

Figure 2.14: Vaned diffuser Mollier chart

The vaned diffuser section implements the diffusion principle by positioning diverging vanes tangential to the impeller. As a result the kinetic energy that is generated by the impeller is converted into pressure energy with a minimal loss. The vanes are aligned with the absolute velocity of the air at the leading edge radius to establish a smooth flow over the vanes for optimum performance.

The most frequently used performance parameter for a diffuser is the pressure recovery coefficient (c_p), defined as the static pressure rise through the diffuser divided by the dynamic pressure at the inlet (Equation 2.4.2). The pressure recovery coefficient signifies the fraction of dynamic pressure at the inlet that is converted into static pressure by the diffuser.

$$c_p = \frac{p_4 - p_3}{p_{t,3} - p_3} \tag{2.4.2}$$

The total pressure at the diffuser discharge is defined as:

$$p_{t,4} = p_{t,3} - (p_{t,3} - p_3) \sum_i \bar{\omega}_i \tag{2.4.3}$$

where the total pressure loss coefficient is represented by $\bar{\omega}_i$. The individual loss coefficients are discussed in Appendix B.4.3.

2.4.2. Geometric parameters

The various geometric parameters that are of importance in the design process of a radial diffuser are discussed in the following section.

2.4.2.1. Passage divergence and radial length

The geometric confinement of gas turbine applications often restricts the engine diameter, e.g. the compressor of this thesis. The radial length of the diffuser suffers from this restriction, for that reason a compact diffuser passage divergence and radial length are vital for adequate diffusion and consequential compressor efficiency.

The area ratio (A_R) and channel length (L_B) specify the divergence angle ($2\theta_C$) in a simple channel diffuser. Clements and Artt (1987) investigated multiple channel divergence angles ranging from 4° to 14°. The pressure recovery of the diffuser channel improved with an increasing divergence angle, however the flow range reduces simultaneously due to the occurrence of surge at higher mass flow rates. Moreover, beyond 12° the pressure recovery improvement ceased and only further reduction of the flow range was observed. The author therefore labelled the 12° channel divergence angle as ideal. A similar design criteria is suggested by Aungier (2000) who proposed a design limit $2\theta_C \leq 11°$; the author advised to apply a divergence angle as close to, but not exceeding, the upper limit. According to the investigation by Yoshinaga *et al.* (1980), the divergence angle of a straight-channel type diffuser has an optimum range from 8° to 10°.

2.4.2.2. Passage geometry

Over the years multiple geometric diffuser passage styles have been used in high pressure ratio applications, referred to as annular diffusers, channel diffusers and conical diffusers. The most common design is a straight-channel diffuser, also known as island-vane diffuser, and are thoroughly investigated by various researchers, e.g. Rodgers (1982) and Osborne and Japikse (1982). The configuration yields good performance and is easy to manufacture.

2.4.3. Aerodynamic parameters

The performance of a diffuser can be specified when three essential inlet parameters are known: blockage, shape of the velocity profile, and the turbulence scale and intensity (Japikse, 1987). The various aerodynamic parameters that are of importance in the design process of a radial diffuser are discussed in the following section, focussing on the inlet parameters.

2.4.3.1. Inlet flow distortions

At the diffuser inlet, the wake from the impeller is identified as a high tangential velocity region with a consequent small flow angle. The jet region in the fixed reference frame is observed as a low momentum region. The overall flow conditions are highly non-uniform because of velocity differences and flow distortions, it is therefore a nontrivial task to match a vaned diffuser to an impeller because of the complicated flow mechanics involved. Whilst complicated, Filipenco *et al.* (2000) underlines the importance of matching the design of the impeller to the diffuser. However, Shum *et al.* (2000) observed that no heavy separation takes place when the fluid flow angle misaligns with only some of the span, e.g. near the hub or the shroud, which allows for a minor discrepancy.

2.4.3.2. Blockage

Blockage is defined by the area equivalent to the boundary layer displacement thickness in the diffuser inlet flow area. For single channel vaned diffusers the pressure recovery decreases when the inlet blockage increases. Clements and Artt (1988) believed that the low pressure recovery in the latter part of the diffuser channel was due to blockage resultant from unstable boundary layers which prevented any further effective area increase.

Excessive boundary layer growth and a large throat blockage is observed by Bennett *et al.* (2000) in the semi-vaneless space due to disproportionate diffusion, severely reducing the performance of the downstream vaned diffuser and possibly reducing the surge margin. On the other hand, if the throat area is decreased excessively, premature choke will occur at the entrance of the vaned diffuser. For that reason it is vital to correctly specify the throat size to ensure matching of the impeller discharge and diffuser inlet flow.

2.4.3.3. Inlet Mach number

The flow at the inlet of the diffuser might, depending on the size and rotational speed of the impeller, reach $Ma_3 \geq 1$ relative to the surface over

which it moves. Due to the excessive loss related to the formation of shock waves it is evident that preventing supersonic flow in the diffuser is prioritized. Although provided that the radial velocity component is subsonic, no efficiency loss is observed with supersonic flow at the leading edge of the diffuser (Saravanamuttoo *et al.*, 2001).

Deniz *et al.* (2014) investigated the variation of the inlet Mach number due to impeller discharge flow distortions and reported a minimal influence on the mass-averaged overall pressure recovery. The author recommends time-averaged flow alignment with the diffuser vanes to anticipate the interaction with the impeller discharge flow and emphasizes the beneficial value in diffuser design. Both Shum *et al.* (2000) and Filipenco *et al.* (2000) agree with this design approach.

3. 1-D Centrifugal Compressor Design

3.1. Introduction

This chapter involves the 1-D component design and performance analysis of a new centrifugal compressor for the RGT 1S/60. The benefit of a preliminary one-dimensional design to identify the effect of alterations in blockage, loss, and slip on the impeller pressure ratio is confirmed by Shum *et al.* (2000) and Came and Robinson (1998).

The 1-D performance analysis examines the flow on the mean stream surface through the centrifugal compressor. Because of this 1-D analyses have apparent characteristic limitations, such as restricted geometry definition while there are an infinite number of designs possible for specific performance parameters. Furthermore solutions for hub to shroud distribution are not provided, therefore the main focus for the flow analysis was to obtain time- and area averaged performance predictions for pressure ratio, efficiency, etc. The new design is bound to the design parameters of the standard compressor.

The objectives regarding the standard compressor did not include using the 1-D software package to analyse the performance. Nevertheless it was attempted to see if reliable data could be collected. However the poor, old and unusual design of the standard compressor created several compatibility issues with the 1-D package, which prevented obtaining reliable results, for example: the impeller shroud ring could not be modelled, the blade angles could not be represented properly, and the simulation crashed or didn't converge as a result of the mismatch in design between diffuser inlet flow angle and blade angle. Only the design parameters of the standard diffuser are used as a reference in this section.

3.2. Review of 1-D software

The software package that is used to perform the 1-D analyses is CompAero by Aungier (2000). CompAero implements the centrifugal compressor aerodynamic design and analysis strategy described in Aungier (2000), and axial flow turbine aerodynamic design and performance theory from Aungier (2003). The mean stream surface computations through all centrifugal compressor parts are executed by numerical methods supported by basic principles of fluid dynamics and thermodynamics.

The software package consists of various programs that each have their own specific function in the compressor design process, nonetheless only SIZE, CENCOM (***CEN***trifugal ***COM***pressor), and VDDESIGN (***V***aned ***D***iffuser ***DESIGN***) were beneficial to engineer a new centrifugal compressor design.

The program CENCOM provides an aerodynamic performance analysis for a centrifugal compressor and plays a central role in the design process. All geometry stages, i.e. the impeller, vaneless radial space and vaned diffuser are defined including the initial conditions of the flow. CENCOM collects performance predictions when a stage is analysed and uses them to provide performance maps for centrifugal compressor design parameters such as: pressure, efficiency, and power.

Program SIZE implements a basic geometry input procedure for a preliminary aerodynamic design. Basic design correlations and parameters are used to get a rough impression of the centrifugal compressor stage design and provide a starting point for more detailed component design activities. The input files for comprehensive aerodynamic stage design in CENCOM and VDDESIGN are created in the SIZE program.

VDDESIGN is responsible for the aerodynamic design of conventional, thin or airfoil style vaned diffusers. The file from SIZE is used as a first input and is modified for most effective diffusion of the outlet aerodynamics of the finalized impeller design from CENCOM.

The CompAero workbench analysis procedure is discussed in Appendix A.1.

3.3. Compressor bounds and target performance parameters

The design of a centrifugal compressor, with a specific performance aim, is highly affected by restrictions due to geometry parameters. In this thesis the impeller and diffuser design were bounded by the profile of the standard centrifugal compressor of the RGT 1S/60. The only boundary that was allowed to be redesigned was the shroud curve, mostly because of the semi-covered shroud ring of the standard impeller which would completely disable any redesign possibility. Figure 3.1 serves as a reference for the impeller bounds.

The impeller discharge radius (r_2) was constrained to a maximum of 82 mm, the impeller inlet shroud radius ($r_{1,s}$) was restricted to 44.35 mm and the impeller inlet hub radius ($r_{1,h}$) of the eye was fixed at 20.65 mm. In addition, the axial height of the impeller (b_{imp}) was set at 45.90 mm and the upper limit of the impeller tip width (b_2) was 8.20 mm. The vaneless radial passage was not fixed but the maximum diameter of the radius (r_4) was 132.25 mm, thus additional vaneless radial passage would be at the expense of vaned diffusion. The vaned diffuser vane width (b_{VD}) was not to exceed 8 mm. Another design constraint on the diffuser was nine bolts equispaced around the axis with a diameter of 7.15 mm that secure the compressor to the compressor housing.

The design point mass flow rate of the compressor was 0.60 kg/s at 46 krpm. Because the turbine design of the RGT 1S/60 was to be kept unchanged, it was of importance that the input power, or torque, would remain the same. Therefore an increase in pressure ratio and an improved efficiency value to compensate for the input power were design targets. The objective of the new compressor design was to attain a pressure ratio of (total-to-static) $p_2/p_{1,t} \geq 3$ and a consequential total-to-total isentropic efficiency that would result in an unchanged input power, or torque. The vane angle of the standard diffuser is 11.48°, which is considered too small for good compressor performance according to the literature (see Section 2.2.3.4). Therefore to reduce the tangential velocity component and subsequently increase the impeller discharge flow angle to improve compressor performance, impeller tip trimming was considered for the new design (see Section 2.2.2.4).

3.4. Impeller

The axial-to-radial flow impeller is a key element in a centrifugal compressor, which manages to achieve substantial pressure ratios and yet remain

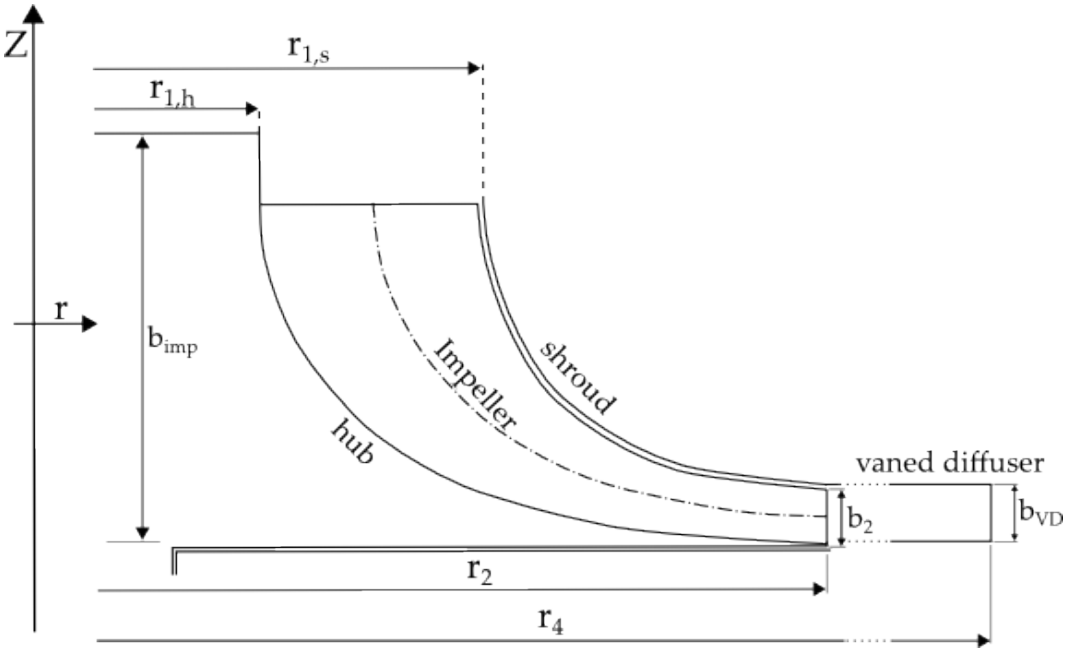

Figure 3.1: Compressor bounds

compact in design. The design and performance parameters of the impeller are discussed in this section.

3.4.1. Preliminary impeller sizing

In CENCOM three-dimensional, straight line-elements (ruled surface) are used for inducer impeller blades and it is common to assume an uniform flow at the axial inlet (Aungier, 2000). A series of quasi-normals from the inlet to the discharge yield the potential flow calculations (Equation 3.4.1).

$$C_{m,h}\Delta m_h = \bar{C}_m \Delta \bar{m} = C_{m,s}\Delta m_s \tag{3.4.1}$$

where Δm is the local meridional length between successive quasi-normals for the hub, mean and shroud contours. The sizing of the impeller requires a rough blade design, acquired using a generalized hub-and-shroud blade angle distribution (Aungier *et al.*, 1993), to prevent unacceptable blade rake angles (the angle between the leading edge of the blade and the perpendicular surface at the hub) which are the most common inconsistency during detailed aerodynamic design (Aungier, 2000).

Hub contours are generated using the largest circular arc possible to obtain the minimum contour curvature, linear additions help to match the impeller eye and tip bounds. The shroud contours are constructed to correspond to their end-point coordinates, a middle point coordinate, and their slopes.

The contour constructions and gas path design are described in Chapter 7 of Aungier (2000).

The impeller blade work input and tangential tip velocity are determined with use of the stage work input and parasitic losses, i.e.

$$I_B = I - I_{par} = C_{U2}/U_2 \tag{3.4.2}$$

Following the impeller work input model (Appendix B.1), the tip blade angle is computed iteratively with use of the Wiesner slip factor (adjusted by Aungier (2000)):

$$\begin{aligned} \sigma &= 1 - \sqrt{\sin \beta_2} \sin \alpha_C / z^{0.7} \\ I_B &= \sigma \left(1 - \lambda C_{m,2} \cot \beta_2 / U_2\right) \end{aligned} \tag{3.4.3}$$

The mean meridional velocity and blade angle of the leading edge are computed from the local blade speed and the flow angle relative to the rotating frame of reference ($\alpha_1^{'}$), defined as:

$$C_{m,1} = U_1 \tan \alpha_1^{'} \tag{3.4.4}$$

3.4.2. Number of blades

The number of blades is normally estimated from the blade loading parameter (Equation 3.4.5), however there was a constraint on the number of diffuser vanes. Hence the blade number was strongly dependent on the number of diffuser vanes that was selected (discussed in Section 3.6.5). After the number of diffuser vanes was selected, the following expression by Aungier (2000) was used in reverse:

$$z_I = z_{FB} + \frac{z_{SB} L_{SB}}{L_{FB}} \tag{3.4.5}$$

where the number of full blades and splitter blades is equal, and the meridional length ratio $L_{SB}/L_{FB} = 0.7$. The preferred effective number of blades (Equation 3.6.7) are either $z_I = 17$ or $z_I = 19$, however the eventual number of blades that was selected is $z_{FB} = z_{SB} = 12$. A higher effective number of blades is selected to benefit from a higher pressure ratio due to improved work conveyance to the fluid without compromising efficiency. As a result the effective number of blades is $z_I = 20$, which was considered close enough to the recommended value and safe as far as resonance was concerned.

3.4.3. Impeller performance

The performance predictions by CENCOM of the impeller component at design point are given in Table 3.1.

Table 3.1: Impeller performance by CENCOM

Impeller	Performance parameters
Mass flow rate ($\dot{m}$) [kg/s]	0.60
Tip rotational speed (U_2) [m/s]	399.9
Sonic inlet area ratio ($A/A^\star$)	1.09
Tip flow angle (α_2) [°]	15.9
Tip total pressure (p_t) [kPa]	369.34
Tip static pressure (p) [kPa]	195.31
Tip total temperature (T_t) [K]	443.94
Adiabatic head coefficient (H_{ad})	0.84
Adiabatic efficiency (η_{ad})	85.9%
Polytropic head coefficient (H_p)	0.86
Polytropic efficiency (η_p)	88.3%

The tip total pressure ($p_{t,2}$) produced by the impeller is considered sufficient to cope with minor pressure losses throughout the vaneless and vaned diffuser, and yet still enough to match the target pressure ratio $p_2/p_{t,1} \geq 3$ at the diffuser discharge. The work coefficients were calculated by CENCOM using the theory described in Appendix B.1, resulting in the work coefficient predictions of the new impeller design shown in Table 3.2.

Table 3.2: Impeller work coefficients by CENCOM

Impeller	Work coefficients
Tip flow coefficient (ψ_2)	0.28
Distortion factor (λ)	1.8731
Work input coefficient (I)	0.98
Blade work coefficient (I_B)	0.934
Disk friction work coefficient (I_{DF})	0.0072
Recirculation work coefficient (I_R)	0.0023
Leakage work coefficient(I_L)	0.032

The loss coefficients were calculated by CENCOM using the loss models described in Appendix B.2. The predicted values are provided in Table 3.3.

Table 3.3: Impeller loss coefficients by CENCOM

Impeller	Loss coefficients
Incidence LC ($\bar{\omega}_{inc}$)	0.201
Inducer diffusion LC ($\bar{\omega}_{DIF}$)	0
Choke LC ($\bar{\omega}_{CH}$)	0.005
Skin friction LC ($\bar{\omega}_{SF}$)	0.407
Blade loading LC ($\bar{\omega}_{BL}$)	0.044
Hub-to-shroud LC ($\bar{\omega}_{HS}$)	0
Critical Mach number LC ($\bar{\omega}_{cr}$)	0
Total LC ($\bar{\omega}$)	0.657

3.5. Vaneless radial passage

The main function of the vaneless radial passage between the impeller tip and diffuser inlet is to reduce the relatively high flow velocity and strong swirl factor at the exit of the impeller before the flow enters the diffuser. By lowering the high Mach numbers that exit the impeller, shock losses resulting from flow separation can be avoided. In addition, the high velocity values at the inlet of the diffuser cause excessive boundary layer growth, the reduced efficient throat area negatively affects the surge margin (Bennett *et al.*, 2000). The Mach number at the impeller tip of both the standard and new impeller design are given in Table 3.4.

Because of the geometry constraints on both the impeller and diffuser, the inlet of the vaneless radial passage remains fixed but the radial length can be adjusted at the expense of vaned diffusion. The shroud height is allowed to be adjusted for the new design but has a maximum of 8 mm. The radius of the diffuser inlet is determined with care. Since the 1-D analysis program is based on the theory by Aungier (2000), the initial general guideline for the inlet radius (r_3) is:

$$1.06 \geq \frac{r_3}{r_2} \geq 1.12 \tag{3.5.1}$$

The diffuser of the standard compressor is positioned close to the impeller but does not comply with the criterion from Aungier (2000), however it is within the lower limit proposed by (Ziegler *et al.*, 2003*a*). The radius length measures 3.76 mm resulting in a radius ratio of 1.046. Aungier (2000) recommends that, if the Mach numbers allow it, the vaneless radial passage ratio should be the smallest possible quantity. This theory is supported by Shum *et al.* (2000) and Ziegler *et al.* (2003*a*) who both suggest similar radius ratio criteria. The new centrifugal compressor was designed with a radius ratio of 1.072, equal to 5.9 mm in radial length, to adhere to the radius ratio

criterion. The Mach number at the diffuser inlet is reduced from 0.88 in the standard compressor to 0.84 in the new compressor design.

The performance predictions by CENCOM of the vaneless radial passage at the operating point (0.60 kg/s) are shown in Table 3.4 and compared to the vaneless passage of the standard RGT 1S/60 vaneless passage.

Table 3.4: Vaneless radial passage performance by CENCOM

Vaneless radial passage	New passage	Standard passage
Radius ratio (r_3/r_2)	1.072	1.046
Mass flow rate ($\dot{m}$) [kg/s]	0.60	0.60
Mach number (Ma_3)	0.84	0.88
Total pressure ($p_{t,3}$) [kPa]	369.34	279.32
Static pressure (p_3) [kPa]	194.19	127.4
Total pressure LC ($\bar{\omega}$)	0.0716	0.0651
Static pressure recovery (c_p)	0.0937	0.0785
Adiabatic efficiency (η_{ad})	83.4%	84.6%
Polytropic efficiency (η_p)	86%	87.3%

3.6. Vaned diffuser

A vaned diffuser is the most effective way of decelerating the high subsonic Mach numbers of the fluid flow exiting the impeller. In addition high pressure recovery can be achieved over a small distance relative to a vaneless diffuser. The design and performance parameters of the vaned diffuser are discussed in this section.

3.6.1. Stall

The prediction of the vaned diffuser stall incidence angle is considered an important aspect in the design process since it leads to flow instability if not correct. The inlet flow angle (α_3) and inlet blade angle (β_3) are the most influential features that affect diffuser stall, with the number of vanes (z_D) also having a significant effect. Aungier (2000) developed a stall design criterion for vaned diffusers (Appendix B.4.2).

There is a geometrical benefit using low design inlet flow angles since the operating range increases and the stability improves (Aungier, 2000). More specifically, successful vaned diffuser designs will generally make use of inlet blade angles between $16^\circ \leq \beta_3 \leq 22^\circ$ (Aungier, 2000). The lower limit

follows from an increase in vaneless space losses with lower flow angles, a higher skin friction coefficient because of longer blades and an increasing possibility that rotating stall may occur. The inlet blade angle of the new diffuser can be found in Table 3.5.

3.6.2. Inlet design

The detailed design of a vaned diffuser starts by forming the leading edge geometry up to the throat area, which is considered the most crucial part of any aerodynamic design because of the high influence on the overall performance of the centrifugal compressor. The leading edge location (r_3) and blade angle β_3 are established first. The primary constraint is the need to match the vaned diffuser to the air flow leaving the impeller tip, yet this air flow is highly distorted. To prevent separation and increased boundary layer thickness the correct incidence angle is important. Aungier (2000) recommends a design incidence angle (i_3) of around -1, i.e. $i_3 = \beta_3 - \alpha_3$.

According to Aungier (2000) vaned diffusers do not handle high flow coefficients (ψ) well as they appear no longer effective at higher flow coefficients. Since dominant loss factors at high flow coefficients are passage curvature losses and diffusion losses, both a result of higher flow angles (α), it is again evident that high flow angles should be avoided in the diffuser design. The flow coefficient (Equation 3.6.1) plus the relevant flow and blade angles at the diffuser inlet are shown in Table 3.5.

$$\psi_2 = \frac{\dot{m}}{\rho_{t,0}\pi r_2^2 U_2} \tag{3.6.1}$$

Table 3.5: Flow data by VDDESIGN

Diffuser	New diffuser	Standard diffuser
Tip flow coefficient (ψ_2)	0.28	0.34
Diffuser flow inlet angle (α_3) [°]	16.44	11.48
Diffuser blade inlet angle (β_3) [°]	15.79	11.2
Blade incidence angle (i_3) [°]	0.65	-0.28

As mentioned in Section 3.6.1, an inlet flow angle that satisfies to the ideal flow angle range is highly desirable for good performance and a wide stable operating range. The results show that the desired increased flow angle by tip trimming is achieved.

Another important parameter that is critical to maximise diffusion is the throat area. The Mach number at the diffuser throat area can reach sonic

numbers and cause the diffuser to choke. Appendix B.4.1 describes how the throat size can be specified correctly to prevent choking in the diffuser.

The design point performance of the 1-D design of the new centrifugal by VDDESIGN is given in Table 3.6, and is compared to the standard diffuser design.

Table 3.6: Design point performance by VDDESIGN

Diffuser	New diffuser	Standard diffuser
Throat area (A_{th}) [cm^2]	11.2	9.94
Sonic throat area ratio ($A_{th}/A^\star$)	1.17	1.06
Incidence LC ($\bar{\omega}_{inc}$)	0.023	0.013
Choke LC ($\bar{\omega}_{CH}$)	0	0.136
Blockage LC ($\bar{\omega}_{\lambda}$)	0.048	0.056

3.6.3. Blade design

When the leading edge and trailing edge geometries are accepted, the actual vane shape is designed in VDDESIGN by specifying the vane thickness distribution on the mean camber line of the blade. The general mean camber line calculation is convenient for this purpose and is described in Chapter 9 of Aungier (2000). The nine equispaced bolts around the axis of rotation not only restrict the number of vanes that can be used, but also influence the vane shape. The bolts have a diameter of 7.15 mm and the bolt radius (r_{bolt}) is 124.1 mm. The design of the blade at r_{bolt} is therefore bound to be wide, which, according to Aungier (2000), requires a considerably higher discharge-to-inlet radius ratio (r_4/r_3) or divergence angle ($2\theta_c$) to reach similar pressure recovery as thin-vaned or airfoil designs.

3.6.4. Design point parameters

A conventional vaned diffuser is dependent on two basic diffusion mechanisms to realize its static pressure recovery, namely the effective passage area and the blade loading effect. The effective passage area increases from inlet to discharge providing streamline diffusion, which is increased by the fluid turning or blade loading effect (Aungier, 2000). Obviously the diffuser will perform best when both diffusion mechanisms operate close to the maximum achievable values. The blade passage length (L_B) and effective passage width (w) are given by:

$$L_B = \int_{r_3}^{r_4} \frac{dr}{\sin\beta} \tag{3.6.2}$$

$$w = \frac{2\pi r \sin\beta}{z} \tag{3.6.3}$$

The discharge sizing of the radial vaned diffuser includes three parameters: equivalent divergence angle $2\theta_C$ (Equation B.4.8), blade loading parameter L (Equation B.4.9), and the area ratio A_R (Equation B.4.10). Aungier (2000) recommends the following design limits

$$2\theta_C \leq 11^\circ \tag{3.6.4}$$

$$L \leq \tfrac{1}{3} \tag{3.6.5}$$

Aungier (2000) introduces a design parameter (E) which evaluates the effectiveness of the vaned diffuser design compared to a vaneless diffuser. The effectiveness design parameter is given by

$$E = \frac{R^2\left(A_R^2 - 1\right)}{A_R^2\left(R^2 - 1\right)} \tag{3.6.6}$$

The effectiveness design parameter serves more as a measure of whether the design has practical merit than as a design criterion. R is defined as radius ratio r_4/r_3. The area ratio is also a significant design parameter for a vaned diffuser. Aungier (2000) supplied two-dimensional diffuser performance maps that show optimum results for the inlet blockage levels to be expected at area ratios between 2.2 - 2.4 in a vaned diffusers with thin- or airfoil shape vanes

These design limits and target parameters provide guidelines in the diffuser design process. It should be apparent that not all of these design guidelines can be satisfied since there are not enough degrees of freedom, especially considering the compressor bounds (Section 3.3). VDDESIGN allows the user to alternate values of R, A_R and z until the best combination of $2\theta_C$, L and A_R is acquired, or establish the parameter most important to his design. The design point parameters of the new diffuser are compared to the standard diffuser of the RGT 1S/60 in Table 3.7.
Note the increase in static pressure recovery for the new design, the higher choke limit, the lower total LC, and the decreased Mach number at the diffuser inlet . The recommended design limits by Aungier (2000) for the $2\theta_C$, L and A_R are all exceeded, mostly due to the thick blade design instead of the preferred airfoil shape.

3.6.5. Number of vanes

In the vaned diffuser design process the number of vanes is selected on both aerodynamic and resonance conditions. Correct calculations for the

Table 3.7: Design point parameters by VDDESIGN

Diffuser	New diffuser	Standard diffuser
Effective divergence angle ($2\theta_C$) [°]	16.44	18.42
Blade loading (L)	0.54	0.43
Area ratio (A_R)	3.49	4.42
Static pressure coefficient (c_p)	0.65	0.54
Inlet Mach number (Ma_3)	0.84	0.88
Discharge Mach number (Ma_4)	0.25	0.19
Effectiveness parameter (E)	2.40	1.64
Total LC ($\bar{\omega}$)	0.23	0.41

number of vanes results in less distortion in the static pressure field due to reduced pressure pulse disturbance in the vaneless radial passage (Bennett *et al.*, 2000). To prevent resonance a compressor design should conform to, $z_{VD} \neq z_I$. Aungier (2000) recommends the following criterion for selecting the number of diffuser vanes:

$$z_{VD} = z_I \pm 1 \tag{3.6.7}$$

Since a low number of z_{VD} improves the stall incidence range the preferred number of vanes is $10 \leq z_{VD} \leq 20$ (Aungier, 2000). If the preferred choice of vane numbers is not within this range, $|z_{VD} - z_I| \geq 8$ is provided.

The potential number of vanes for the diffuser was constrained because of the nine equispaced bolts that fasten the compressor to the compressor housing. A multiple of nine diffuser vanes was considered an alternative that would comply with this limitation. Since there was no constraint on the number of impeller blades, the number of diffuser vanes was selected first. The selected number of vanes, z_{VD} = 18, agrees with the stall incidence range criteria suggested by Aungier (2000) and matches a reasonable total of efficient impeller blades (Section 3.4.2).

3.7. Compressor stage overall performance

The overall performance predictions by CENCOM of the centrifugal compressor stage at design point are given in Table 3.8.

The compressor stage overall performance predictions show that the target parameters set in Section 3.3, e.g. a total-to-static pressure ratio ≥ 3 with an efficiency value that would keep the input power close to the 144.14 kJ/kg benchmark, were accomplished.

Table 3.8: Compressor stage overall performance by CENCOM

Compressor	Parameters
Mass flow rate ($\dot{m}$) [kg/s]	0.60
Discharge static pressure (p_4) [kPa]	325.97
Discharge total temperature (T_t) [K]	443.91
Discharge flow coefficient (ψ)	0.0285
Total-to-static pressure ratio ($p_2/p_{t,1}$)	3.25
Adiabatic head coefficient (H_{ad})	0.84
Adiabatic total-to-total efficiency (η_{ad})	86.65%
Polytropic head coefficient (H_p)	0.87
Polytropic total-to-total efficiency (η_p)	88.54%
Input power (W_c) [kJ/kg]	144.57

4. Centrifugal Compressor Numerical Analysis

4.1. Introduction

The modelling procedures of both the standard and the new compressor, as well as the computational flow generation are discussed in the following chapter.

A detailed discussion of the 3-D software package platform, the required parameters, and the procedures followed is included in Appendix A.2.

4.2. Procedure for modelling the standard compressor

To get a grasp on the numerical analysis procedure used in this thesis, the subsequent section is devoted to describe the utilized modelling techniques. The standard RGT 1S/60 compressor is first discussed.

The geometry of the standard compressor was previously converted into an IGES file by use of an optical scanner. For this thesis the IGES files are imported into Autodesk® AutoCAD® software. The file import caused some irregularities resulting in a CAD model that was composed of mismatching surfaces. This resulted from either a point cloud of the optical scan that was too coarse, or because of the low quality of the IGES format that was used to save the optical scan. Following this, AutoCAD® software was used to clean the geometry file and get the best possible representation of the standard compressor impeller and diffuser (Figure 4.1).

As observed in the CAD model, the impeller is semi-covered and technically consists of two blade sections. The first part is a conventional axial blade that is shrouded (from here on referred to as a shroud ring), followed by a

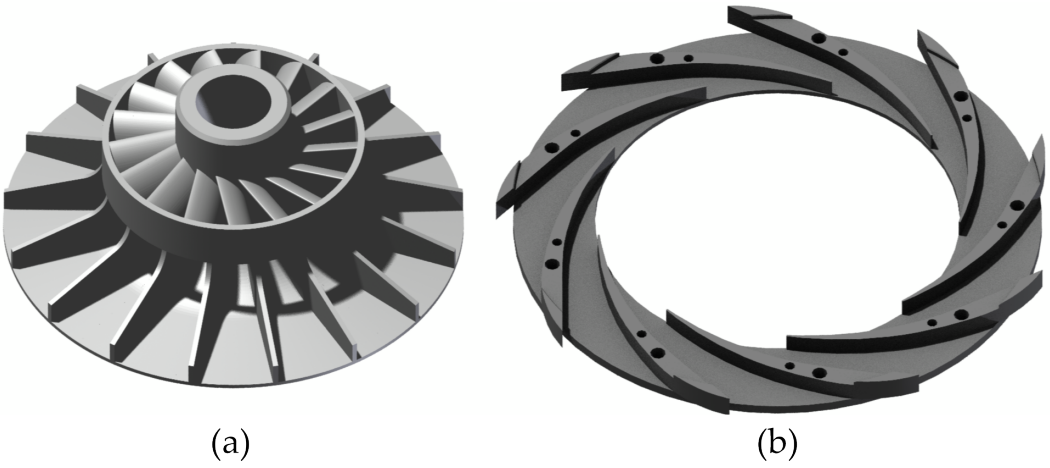

Figure 4.1: CAD model of the impeller (a) and diffuser (b)

straight radial section. The dimensions of the impeller are shown in Figure 4.2 and Table 4.1.

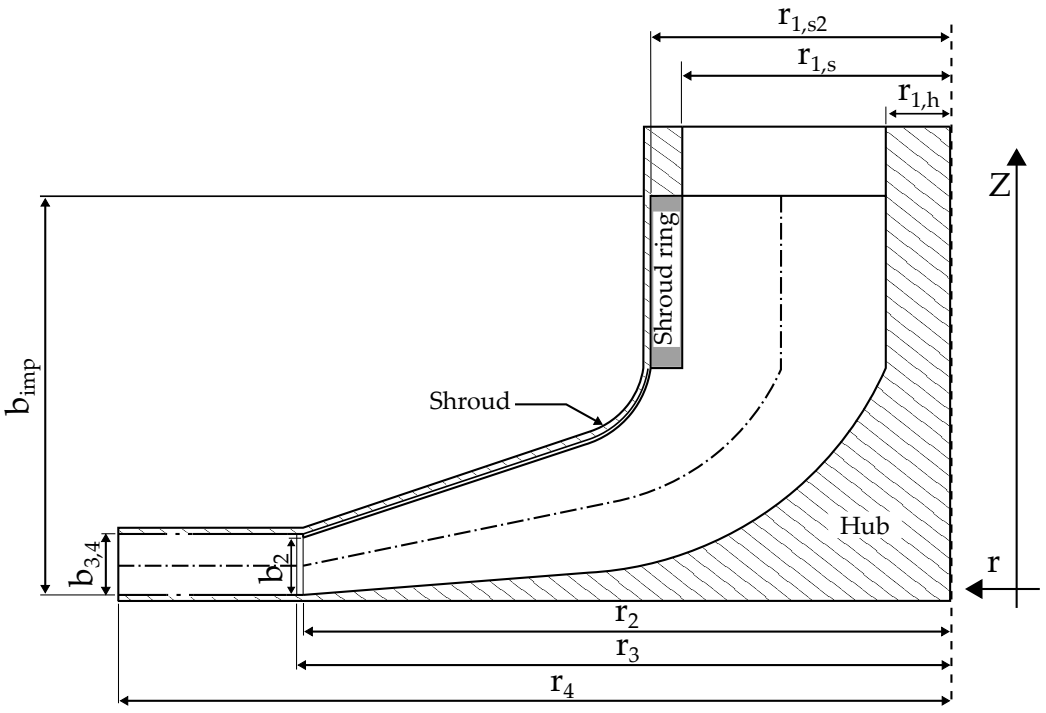

Figure 4.2: Meridional view of the standard compressor geometry

Table 4.1: Compressor dimensions

Parameters	Value [mm]
Hub radius ($r_{1,h}$)	20.65
Shroud radius ($r_{1,s}$)	44.35
Shroud ring radius ($r_{1,s2}$)	46.35
Impeller tip radius (r_2)	82.00
Diffuser inlet radius (r_3)	85.76
Diffuser discharge radius (r_4)	132.23
Impeller width (b_{imp})	42.90
Impeller tip width (b_2)	8.20
Diffuser width ($b_{3,4}$)	8.80

4.2.1. Computational domain

The computational domain of the standard compressor used for the CFD analysis stretched from the impeller inlet to the outlet of the vaned diffuser, as seen in Figure 4.3. The inlet of the computational domain is located 35 mm upstream of the leading edge of the impeller blade, and is modelled parallel to the r-θ plane. The outlet of the computational domain is located 20 mm downstream of the diffuser vane. This vaneless section after the diffuser vane is added for better convergence. Nonetheless a recirculation region at the trailing edge of the suction side of the diffuser vane had a negative impact on convergence, therefore the vaneless outlet domain was slightly pinched in an attempt to improve convergence. The somewhat pinched outlet domain increases the velocity gradient of the flow, reducing the probability of reverse flow that re-enters the outlet boundary and hinders convergence. The RGT 1S/60 compressor is not provided with a volute, instead a small 90° bend is installed at the shroud of the diffuser discharge to redirect the radial flow in the axial direction. This bend is not included in the computational design because the focus of this thesis was on the compressor.

4.2.2. Mesh generation

Because of the form of the standard compressor, ANSYS® TurboGrid™, could not be used to mesh the compressor. As an alternative the ANSYS® Meshing application was used to generate a mesh. This meant that instead of just the hub and shroud curves, a CAD file was required that represented the entire flow path of the standard compressor in solid form, consisting of: the inlet, the impeller, the vaneless radial passage, the diffuser, and the outlet. Following this the CAD file generated with the AutoCAD® software is exported to Autodesk® Inventor LT™ to create the solids necessary to gen-

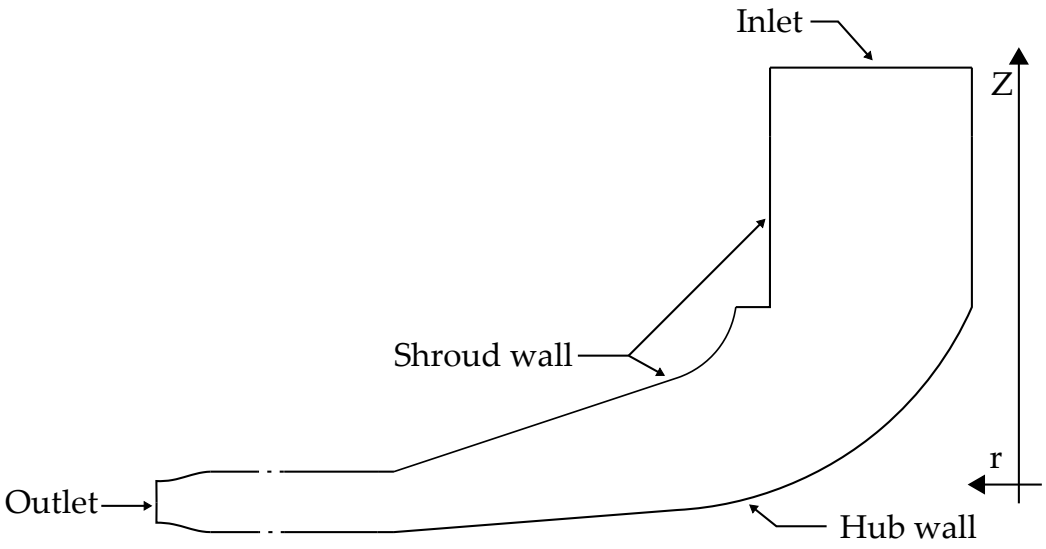

Figure 4.3: Meridional view of the standard compressor's computational domain

erate a mesh with ANSYS® Meshing.

The meshing process starts by specifying the global mesh controls, after which local mesh controls are used to refine or alter local areas. Following this the mesh is generated to check if the mesh complies with the quality criteria, the mesh controls are adjusted if the criterion are not met.

The standard compressor was meshed with 3 different cell types. The sweep method was used on the applicable bodies to generate hexahedrons where possible, and prisms on sections where hexahedral elements would lead to bad quality. On more complex shaped bodies tetrahedral cells were used. Inflation layers were applied to achieve y^+ values that were within the required range of the flow model, i.e. < 300 (Appendix E.3). The 3-D mesh of the standard compressor can be viewed in Figure E.2. Also the surface mesh at the leading edge and trailing edge of the diffuser is displayed in Figure E.3.

4.2.3. Mesh quality

The equations that are solved in CFD prefer equilateral/equiangular cells. Hence the overall quality of the computational mesh must comply to several quality criteria to ensure that important geometric details are captured, and to prevent convergence difficulties. The ANSYS® Meshing application displays the mesh information for nodes and elements, and allows the user to inspect the quality criteria for the mesh metric.

The mesh quality criteria used for the mesh of the standard compressor are given in Table 4.2. The quality requirements for the CFX®-Solver were established in correlation with the recommended mesh metric criteria (ANSYS Inc., 2012*b*). The standard compressor mesh consists of 2823785 nodes and 6796255 elements and met most of the set quality criteria as shown in Table 4.2.

Table 4.2: Mesh quality of the standard compressor (ANSYS® Meshing)

Mesh metric	Criteria	"Worst" value	"Bad" cells [%]	Ave.
Orthogonal quality	>0.25	0.365	0%	0.897
Aspect ratio	<1000	155	0%	1.04
Mesh expansion	<2.5	2.92	0.007%	1.54
Skewness	<0.9	0.85	0%	0.999

4.3. Procedure for modelling the new compressor

The modelling of the new compressor continued from the 1-D design (Chapter 3). The impeller hub and shroud contours generated with CompAero were represented by a continuous curve from impeller inlet to outlet, similar for the diffuser, and the mean-line of the impeller blade and diffuser vane profile was also represented by a single curve. The curves were then imported in ANSYS® BladeGen™ using the BladeGen™ import wizard where the outline of the blade profile and meridional plane were defined. Following this, the BladeGen™ software was used to evaluate the impeller blade and diffuser vane design, and slightly modify the design after the CFD results were processed to improve the stage performance. The BladeGen™ user interface is displayed in Figure E.1.

The geometry of the new compressor was created by importing the BladeGen™ files into the ANSYS® DesignModeler™. Following this the files were exported to Autodesk® Inventor LT™ with which the CAD design was finalized (Figure 4.4).

The dimensions of the impeller are shown in Figure 4.5 and Table 4.3.

4.3.1. Computational domain

The computational domain of the new compressor is of the same principle as the standard compressor. The domain stretches from the impeller inlet

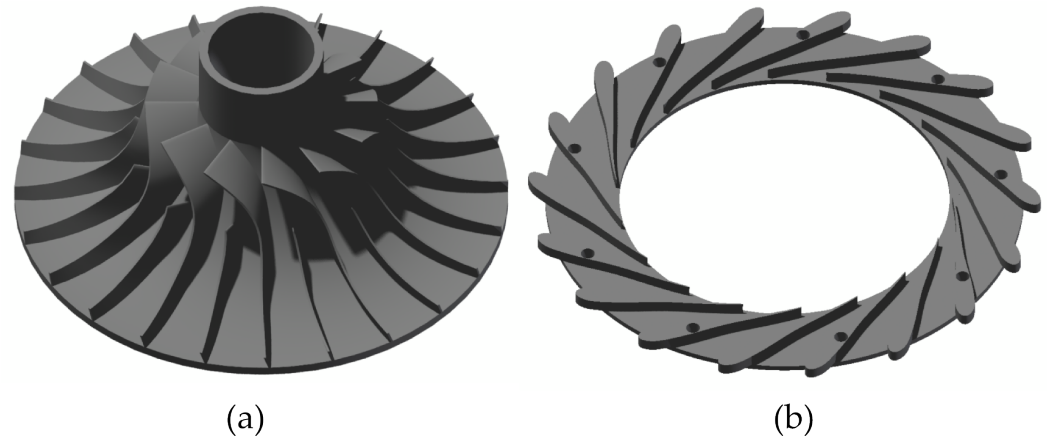

Figure 4.4: CAD model of the impeller (a) and diffuser (b)

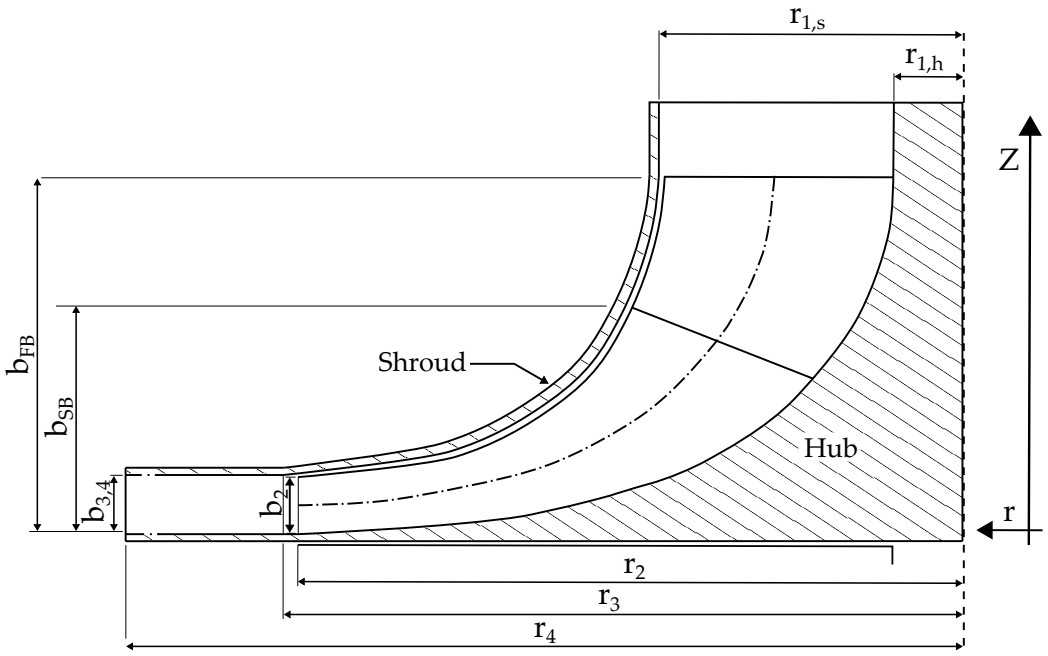

Figure 4.5: Meridional view of the new compressor geometry

to the outlet of the vaned diffuser, as seen in Figure 4.6. The inlet of the computational domain is located 24 mm upstream of the leading edge of the impeller blade, and is modelled parallel to the r-θ plane. The outlet of the computational domain is located 10 mm downstream of the diffuser vane. As with the standard compressor, no volute is simulated.

Table 4.3: Compressor dimensions

Parameters	Value [mm]
Hub radius ($r_{1,h}$)	20.65
Shroud radius ($r_{1,s}$)	44.35
Shroud ring radius ($r_{1,s2}$)	46.35
Impeller tip radius (r_2)	81.59
Diffuser inlet radius (r_3)	85.75
Diffuser discharge radius (r_4)	132.28
Impeller full blade width (b_{FB})	42.76
Impeller splitter blade width (b_{SB})	25.2
Impeller tip width (b_2)	6.1
Diffuser width ($b_{3,4}$)	6.1

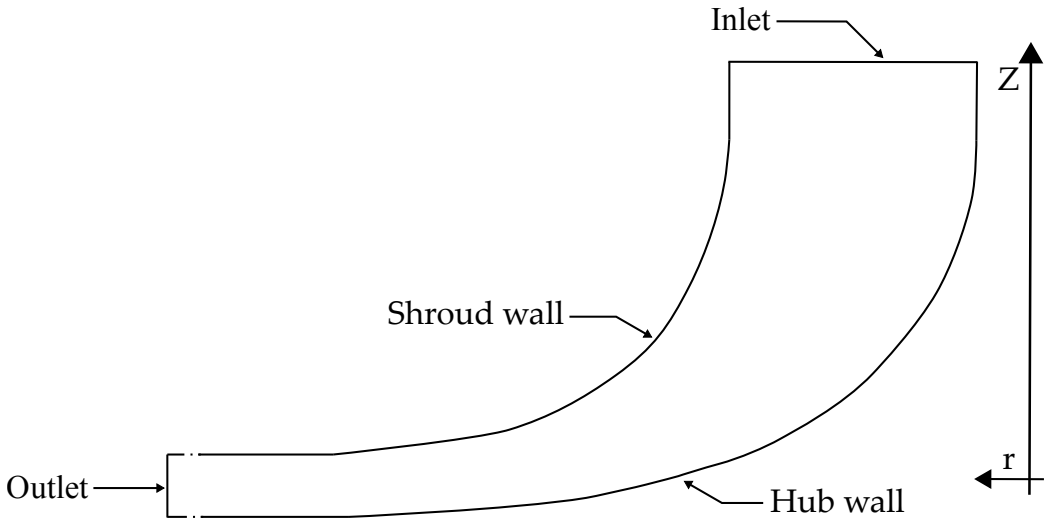

Figure 4.6: Meridional view of the new compressor's computational domain

4.3.2. Mesh generation

The ATM Optimized method in ANSYS® TurboGrid™ was used to automatically compute a default mesh. This method controls each unique mesh dimension by multiplying a specific edge refinement by a global size factor or specific refinement factors. Increasing the global size factor will non-linearly increase the total mesh size, and the overall mesh size will decrease when this factor decreases. Local edge refinements were used to increase or decrease the mesh size of local regions around the leading and trailing edge of the blades. Samples of the blade-to-blade impeller leading edge and trailing edge are shown in Figure E.4. The blade-to-blade diffuser leading edge

and trailing edge are displayed in Figure E.5.

TurboGrid™ provides a constant expansion rate within the O-grid block around the blade to distribute the elements normal to the blade surface, and assure a smooth transition to the passage mesh. The expansion rate is controlled by specifying the number of elements normal to the blade, which can be done by defining both the factor base and factor ratio. The option proportional to mesh size computes the edge refinement factor that will increase the resolution in the O-grid. The edge refinement is worked out as the sum of the factor base, factor ratio, and global size factor. The mesh settings are listed in Table 4.4.

The cells near the hub, shroud and blade wall were inflated to attain low y^+ values concerning accurate capture of the boundary layer velocity gradient. The y^+ values in the boundary layer are within the viscous sublayer range, i.e. between 0 and 10 (Appendix E.3). Only at the impeller tip the y^+ values do not comply, this is further discussed in Section 4.3.3.

The span-wise mesh distribution can be changed in several manners. For this mesh the proportional method is used where TurboGrid™ automatically computes the number and distribution of elements in the span-wise direction, resulting in an identical near wall element height for the hub, the shroud, and the blade.

The element count for the clearance gap was kept at 50 when refining the mesh since Shum *et al.* (2000) stated that due to the inviscid nature of leakage flow and the thin impeller shroud tip, less nodes are required for tip clearance simulation in CFD.

Table 4.4: Mesh settings

Mesh data	Impeller	Diffuser
Global size factor	1.8	1.5
Boundary refinement Factor Base	2.05	3
Boundary refinement Factor ratio	0.75	1.5
Boundary cutoff edge	0.8	-
Passage factor	2.5	1.5
Shroud tip clearance # elements	50	-

4.3.3. Mesh quality

The mesh quality for the new compressor had to comply to the same quality criteria as the standard compressor to ensure that important geometric details were captured and to prevent convergence difficulties (Section 4.2.3). However, TurboGrid™ works with a minimum and a maximum face angle instead of a skewness factor, which is essentially the same. The TurboGrid™ application shows the mesh statistics of the elements, and allows the user to inspect the quality criteria for the mesh metric. The mesh of the new impeller consists of 9301295 nodes and 8988686 elements. The quality criteria that were set for the mesh, and the mesh statistics of the new impeller are shown in Table 4.5.

Table 4.5: Mesh quality of the new impeller (TurboGrid™)

Mesh metric	Criteria	"Worst" value	"Bad" cells [%]
Orthogonal angle [°]	>25	79.8	0%
Aspect ratio	<1000	195.75	0%
Mesh expansion	<2.5	39.63	0.0227%
Minimum face angle [°]	15	24.98	0%
Maximum face angle [°]	165	157.2	0%

The mesh statistic of the new impeller show that 0.0227% of the cells exceed the mesh expansion criteria. Out of a total of 8988686 cells this comes down to 2040 cells. The tip clearance at the trailing edge region of both the main and splitter blade is where the mesh limits were not met (Figure E.9). Consequently the y^+ values at the impeller tip do not fall within the viscous sublayer range. Nevertheless Shum *et al.* (2000) concluded that the leakage flow is quite different from a standard boundary layer fluid flow due to the inviscid nature and the thin impeller shroud tip. Shum *et al.* (2000) stated that the use of lesser nodes for tip clearance simulation in CFD is justified. But the lesser nodes do effect the mesh quality and y^+ values.

ANSYS, Inc. only recently added cut-off blade support to TurboGrid™ ATM, and this unfortunately is a weak spot that could not be addressed. Since the "bad" cells represent only a fraction of the total number of cells, the mesh was considered acceptable. The mesh of the new diffuser consists of 2444400 nodes and 2369268 elements. The mesh statistics of the new diffuser are shown in Table 4.6.
The mesh quality requirements for the CFX®-Solver were established in correlation with the recommended mesh metric criteria (ANSYS Inc., 2012*b*) and with the default TurboGrid™ mesh limits.

Table 4.6: Mesh quality of the new diffuser (TurboGrid™)

Mesh metric	Criteria	"Worst" value	"Bad" cells [%]
Orthogonal angle [°]	>25	32.3	0%
Aspect ratio	<1000	529.3	0%
Mesh expansion	<2.5	2.234	0%
Minimum face angle [°]	15	53.65	0%
Maximum face angle [°]	165	117.0	0%

4.4. Computational flow generation

Since the numerical analyses for both compressors is performed in similar fashion, the computational flow generation of both the standard compressor and the new compressor are discussed in the following section.

4.4.1. Fluid model

The operating fluid used in the CFD simulations of the standard compressor and the new compressor was atmospheric air. The ideal gas model was selected as gas model in CFX®-Pre for both the standard compressor and the new compressor design.

4.4.2. Flow model

The simulations were performed in steady state condition. However after the steady state simulations proved problematic for the standard compressor, transient mode was selected for the remainder of the simulation process using the steady state result files as initial conditions.

A turbulent Navier-Stokes flow solver was used for the standard compressor with the two-equation SST k-ω model to solve the flow equations. The SST k-ω model was preferable over the other two-equation models, k-ϵ and k-ω, because of its better convergence. The k-ϵ and k-ω models, especially the latter, were unstable. Due to the instability in the flow and the recirculation encountered in the diffuser the flow models were difficult to compare but a time-averaged mass-flow average of the pressure ratio and efficiency illustrated a deviation between all flow models of approximately 4%.

For the new compressor design the time invested in the preliminary 1-D design paid off in the 3-D numerical analysis. Only small adjustments had to be made and no flow dynamics caused convergence problems. As with the standard compressor the two-equation models k-ϵ, k-ω and SST k-ω were

considered and the flow performance prediction and stability of the turbulence models were compared. The SST k-ω turbulence model behaved unstable and predicted unrealistic recirculation in the diffuser. The k-ϵ model on the other hand showed better convergence but failed to properly model separation or recirculation. The k-ω model was eventually selected because of its good convergence and boundary layer flow prediction, however this model does seem to over-predict the efficiency value and pressure ratio.

The temperature, 293 K, and pressure, 101 kPa, used as reference values in CFX®-Pre were measured in the test facility on an average day.

4.4.3. Rotating machinery

The clockwise rotational speed of the standard and new impeller was set to 46 krpm to define the operating flow range at design speed. The diffuser is stationary and was therefore simulated in the stationary frame of reference. Since the frame of reference for the impeller is rotating a general connection interface was applied between the impeller and the diffuser (see Section 4.4.4).

For the standard compressor the initial conditions were unknown, and the solver had trouble to prevent back-flow at the diffuser outlet when these conditions were not met at a rotating speed of 46 krpm. Therefore a physical start-up procedure was simulated to benefit from the more relaxed error margins of the initial conditions at lower rotation speeds. The rotational speed was initially set at half the operational speed, namely 23 krpm, and from there on the rotational speed was increased with 5 krpm with every simulation to reach 46 krpm.

4.4.4. Boundary conditions

The boundary conditions for both compressors were defined in CFX®-Pre, and were identical for both numerical analyses. The boundary conditions were composed of six boundary groups:

1. Inlet
The inlet boundary was assigned to the compressor inlet, a relative total pressure imposed boundary condition was selected. The inlet property quantities are defined in Table 4.7.

2. Outlet
The outlet boundary is allocated for a static pressure imposed boundary condition to perform the calculations. For the new compressor design the 1-D performance parameters gave a good indication of the initial conditions

Table 4.7: Inlet boundary property values

Property	Value
Velocity vector	Normal to surface
Absolute total pressure [kPa]	101.325
Absolute total temperature [K]	293
Turbulent viscosity [m^2/s]	0.0001

of the 3-D analysis; a static pressure of 3.5 atm at the outlet was appropriate.

However, due to the nature of the solver and the standard compressor design some problems regarding the initial conditions had to be resolved to start the simulation. A physical start-up was simulated as discussed in Section 4.4.3. The back-pressure was intentionally left low during the start-up process, only when 46 krpm was reached the static pressure value at the outlet was increased to a higher value. Eventually an initial outlet static pressure of 1.5 atm resulted in a successful simulation with reasonable results.

Unfortunately CFX® does not automatically adapt the back pressure to impose the prescribed mass flow rate, therefore the back pressure is altered manually for both compressor simulations to obtain the correct mass flow rate after convergence.

3. Opening
The initial conditions for the standard compressor were not accurate enough at first, which caused the CFX®-Solver to try and enforce outflow by erecting walls at a portion of the outlet. This was overcome by temporarily replacing the outlet boundary condition with a pressure-specified opening. Both outflow and inflow are allowed preventing artificial walls from being erected. However as the solution progressed, inflow kept occurring at the outlet boundary due to excessive recirculation as a result of separation. Therefore the outlet region was moved further downstream and was pinched to enforce outflow. Following this an outlet boundary was used again, but solely when the specific initial conditions at the outlet were available.

4. Wall
The wall boundaries were used for all solid surfaces such as the impeller blades, the diffuser vanes, and the hub and shroud surfaces. For the impeller blades and impeller hub surface the rotating wall type was selected and set to the same rotational speed as the impeller, and a counter-rotating wall boundary option was used for the impeller shroud to simulate a stationary parameter. Since the diffuser domain is motionless, all wall bound-

aries in the diffuser are stationary.

5. Periodic
The computational time required for a simulation with a fine mesh to converge is a large limitation on CFD analysis. Consequently the option of periodic boundaries represents the full mesh with only the least number of blades and vanes necessary to reduce computational time. The rotational periodicity interface model was applied to both the impeller and the diffuser. The full mesh was represented by one main blade, one splitter blade, and one diffuser vane.

6. General connection
The interface of the impeller and diffuser domain was covered by a frame change with use of the general connection interface model. The general connection option is required when one side of the interface is in a stationary frame of reference and the other side in a rotating frame of reference, as is the case with a centrifugal compressor.

The frozen rotor frame change model was applied as an option of the general connection. This model provides a snapshot of the flow at the interface by freezing the relative position of the impeller to the diffuser. The least amount of computational effort is required for this type of connection, however, the disadvantage of this method is the exclusion of transient effects. Any dynamic interaction between the two domains is not modelled, only approximated.

4.4.5. Solver control

4.4.5.1. Standard compressor

As the standard compressor was simulated in transient analysis type, the control variables for the time dependent behaviour of transient simulations had to be determined by means of the time duration and the timestep. The timestep (Δt) allows CFX® to track the progress of real time during the simulation, and time duration (t_d) is specified by the user to limit the real time the simulation is to run. The CFX®-Solver uses specified values of the time duration and the timestep to determine whether the simulation must be continued or finished. For instance the CFX®-Solver will continue to work out the solution at each timestep iteration until $N\Delta t \geq t_d$, where N denotes the number of actually performed timesteps.

The time duration option "time per run" was used where the real time, relative to the initial time specified for this run, at which to end the transient analysis is defined. Adaptive timestepping was used to automate the pro-

cedure of modifying the timestep. In addition the initial timestep, minimum timestep and maximum timestep parameters were specified. Firstly the time per run was defined as the total time equal to one complete rotation of the impeller at operating speed (Equation 4.4.1), and secondly the initial timestep was determined (Equation 4.4.2).

$$t = \frac{1}{(RPM/60)} \tag{4.4.1}$$

$$\Delta t_{initial} = \frac{(RPM/60)}{c_{loops} \cdot \Delta t_{per\,passage} \cdot z_{PG}} \tag{4.4.2}$$

where c_{loops} is the maximum number of coefficient loops carried out per timestep, $\Delta t_{per\,passage}$ is the number of timesteps per blade passage, and z_{PG} is the total number of impeller blade passages. The number of coefficient loops is the adaptive timestep option that was used, where a target minimum/maximum number of coefficient loops within a timestep is selected. If the actual number of coefficient loops used is less than the target minimum coefficient loops or greater than the target maximum coefficient loops, the timestep will increase or decrease respectively. The timestep increase factor and the timestep decrease factor were specified. The basic settings for the transient analysis are given in Table 4.8.

Table 4.8: Basic settings of the transient analysis

Transient setting	Value
Time per run [s]	0.001304
Initial time [s]	0
Initial timestep [s]	7.67e^{-06}
Maximum timestep [s]	0.0001
Minimum timestep [s]	7.67e^{-06}
Target max. loops	5
Target min. loops	3
Timestep decrease factor	0.8
Timestep increase factor	1.06

The use of adaptive timestepping, homing in on 3-5 coefficient loops per timestep, will automatically find an efficient and small enough timestep to meet the convergence criteria of 1e^{-04} RMS. Obviously it is important to check timestep convergence during a simulation. A specific Courant number was not used for stability due to the nature of the CFX®-Solver. Hence the Courant number was only used as an additional check to see if

the timestep was correctly specified.

The transient scheme used in the simulation was a second-order accurate backward euler scheme, the default in ANSYS® CFX®, which is applicable for variable timestep sizes.

The initial values for the simulation are obtained from steady state simulation.

4.4.5.2. New compressor

The basic settings of the solver control for the new compressor were specified for a steady state analysis. The auto timescale was selected as fluid timescale control. The convergence criteria were set to a maximum of 1000 iterations or RMS residuals smaller than 10^{-4}. The turbulence numerics option was set to first order, which required less computational power and produced adequate results.

4.5. Numerical analysis conclusion

The 1-D software system provided a suitable preliminary design that exhibited applicable properties when transferred to the 3-D software platform. The 1-D and 3-D software systems for turbomachinery are prone to user errors which influence computational results, therefore caution is essential.

5. Experimental Setup

5.1. Introduction

The work related to the experimental performance of the Rover Gas Turbines 1S/60 gas turbine is detailed in this chapter. The experimental setup was built for the centrifugal compressor work of this thesis, and simultaneously supporting a thesis where the operational fuel of the RGT 1S/60 will be Liquefied Petroleum Gas (LPG). Besides these two research theses the experimental setup will be used for future gas turbine related research. The gas turbine test facility, instrumentation and operating principle are discussed in this chapter.

5.2. Performance model

The RGT 1S/60 was firstly evaluated with a thermodynamic cycle calculation, predicting the general performance and the working of its turbomachinery. Some initial performance predictions specified in the Rover Gas Turbines Ltd (1965*a*) were incorporated in the model that follows the gas turbine performance calculations given by Saravanamuttoo *et al.* (2001).

The ideal Brayton cycle describes the workings of a constant pressure gas turbine and consists of three components: a gas compressor, a combustion chamber, and an expansion turbine. The location after and/or before a stage is numbered in Figure 5.1 for identification in equations.

In the following subsections the temperature and pressure values were estimated at a stagnation point where the fluid velocity equals zero. Evidently all kinetic energy at this stagnation point has been converted into pressure- and internal energy (isentropically) so, in compressible flows, stagnation fluid properties are equal to total fluid properties.

The performance predictions of the RGT 1S/60 at design point were calculated with a mass flow rate, power output, and maximum combustor outlet

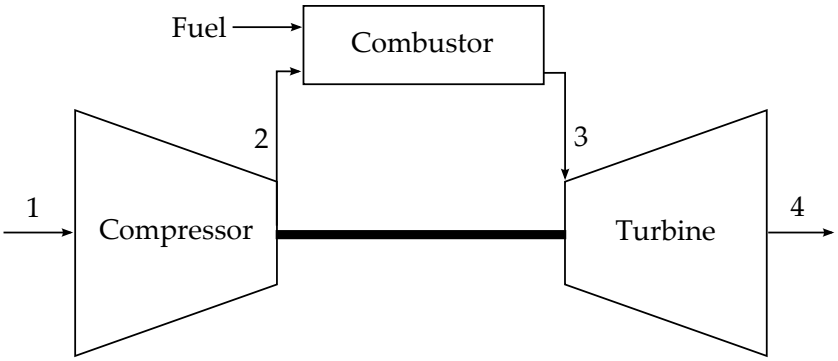

Figure 5.1: Gas turbine cycle diagram

temperature values all obtained from the Rover Gas Turbines Ltd (1965*a*) and specified in Table 5.1.

Table 5.1: Rover Gas Turbines Ltd (1965*a*) performance specifications

Gas turbine properties	
Mass flow rate ($\dot{m}$) [kg/s]	0.60
Pressure ratio ($p_{t,2}/p_{t,1}$)	2.8
Maximum combustor outlet (T_3) [K]	1032
Power output [kW]	45

5.2.1. Compressor efficiency prediction

The actual work done by the compressor was firstly calculated to predict the isentropic efficiency. The effect of various friction forces on the power output from a compressor was accounted for by introducing a power input factor ψ = 1.04 (Saravanamuttoo *et al.*, 2001). Furthermore the simplified Stanitz slip factor (Equation 5.2.1) was used to accommodated a slip loss which affects the actual work done by the compressor.

$$\sigma = \frac{1 - (0.63\pi)}{z} \tag{5.2.1}$$

The first law of thermodynamics was then used to derive a stagnation temperature equivalent to the work done:

$$T_{02s} - T_{01} = \frac{\psi \sigma U^2}{C_p} \tag{5.2.2}$$

Since the pressure ratio over the compressor was given (Table 5.1), the isentropic efficiency was calculated with the following definition:

$$\frac{p_{02}}{p_{01}} = \left(\frac{\eta_c(T_{02s} - T_{01})}{T_{01}} + 1 \right)^{\gamma/(\gamma-1)} \tag{5.2.3}$$

An isentropic efficiency value of *70.6%* was found.

5.2.2. Turbine performance prediction

The performance prediction of the axial flow turbine stage started by calculating the efficiency. The axial flow turbine model by Saravanamuttoo *et al.* (2001) was used to determine the isentropic efficiency and is described in Appendix C. The applied model estimated an isentropic efficiency of *85.4%* for the axial flow turbine stage. The efficiency estimate was used to calculate the turbine output temperature, given:

$$T_{04} = T_{03} - \eta_t T_{03} \left(\frac{p_{04}}{p_{03}} \right)^{(\gamma-1/\gamma)} \tag{5.2.4}$$

The first law of thermodynamics was used to estimate the actual work done by the turbine (Equation 5.2.5). Following this the total power output of the axial flow turbine is then calculated (Equation 5.2.6).

$$W_t = C_{p0}(T_{03} - T_{04}) \tag{5.2.5}$$

$$\dot{W}_t = \dot{m} W_t \tag{5.2.6}$$

5.2.3. Combustor performance prediction

The mass flow rate of fuel that is supplied to the combustor was estimated by using a theoretical fuel/air ratio ($f_{theoretical}$) and an actual fuel/air ratio (f_{actual}) of 0.0202 and 0.0204 respectively (Saravanamuttoo *et al.*, 2001). The actual fuel/air ratio was used to calculate the fuel flow (Equation 5.2.7) and the Specific Fuel Consumption (SFC) of the gas turbine (Equation 5.2.8).

$$\dot{m}_f = \dot{m}(f_{actual}) \tag{5.2.7}$$

$$SFC = 3600(f_{actual})/\dot{W}_{net} \tag{5.2.8}$$

Later the heat added to the system by the combustor was calculated (Equation 5.2.9) with which it was possible to calculate the stagnation temperature downstream of the combustor stage (Equation 5.2.10).

$$Q_h = (\dot{m} + \dot{m}_f)h_{03} - \dot{m}h_{02} \tag{5.2.9}$$

$$T_{03s} = \left(\frac{Q_h}{C_{p0}}\right) + T_{02s} \tag{5.2.10}$$

For the pressure drop over the combustor Saravanamuttoo *et al.* (2001) suggested a value of 2% to 8%, therefore the exact average of 5% was assumed. The efficiency of the combustor is defined by

$$\eta_{combustor} = \left(\frac{f_{actual}}{f_{theoretical}}\right) \tag{5.2.11}$$

5.2.4. RGT 1S/60 operating statistics

The torque produced by the RGT 1S/60 was of interest for the experimental tests, therefore the torque on the main shaft was estimated using

$$\tau = \frac{Power}{2\pi\omega} \tag{5.2.12}$$

The estimated torque on the main shaft was multiplied by the gearbox ratio of the RGT 1S/60 to obtain the torque on the drive shaft of the dynamometer. Following the performance estimate from the two turbomachinery stages, an overall thermodynamic cycle efficiency value was approximated, using:

$$\eta_{TT,0-4} = \frac{\dot{W}_t - \dot{W}_c}{Q_h} \tag{5.2.13}$$

The end result of the thermodynamic cycle calculation was an overall efficiency of *10.5%*. This may seem poor, however the age of the design does support this low efficiency value. All predicted performance specifications that are of importance are shown in Table 5.2.

The performance estimates of the RGT 1S/60 are similar to the results from Prinsloo (2008), who predicted η_c = 71%, η_t = 86%, and $\eta_{TT,0-4}$ = 10.7%. Quarta (2012) also created a performance model of the RGT 1S/60 and predicted η_c = 70.5%, η_t = 84.8%, and $\eta_{TT,0-4}$ = 10.6%.

Table 5.2: General performance predictions of the RGT 1S/60

Estimated gas turbine properties	
Mass flow rate ($\dot{m}$) [kg/s]	0.603
Compressor exit temperature ($T_{t,2}$) [K]	445.37
Compressor isentropic efficiency (η_c)	70.6%
Power consumption of the compressor ($\dot{W}_c$) [kW]	84.54
Combustor efficiency ($\eta_{combustor}$)	99%
Exhaust gas temperature ($T_{t,4}$) [K]	846.60
Turbine isentropic efficiency (η_t)	85.4%
Power produced by the turbine ($\dot{W}_t$) [kW]	128.72
Net power output [kW]	44.76
Drive shaft torque output [Nm]	144.14
Overall thermal cycle efficiency ($\eta_{TT,0-4}$)	10.5%

5.3. RGT 1S/60 gas turbine overview

The experimental setup could only be built when the working of the RGT 1S/60 and all its components were properly understood. Therefore a second RGT 1S/60 (also property of the Mechanical Engineering department of Stellenbosch University) was completely disassembled to provide access to all parts and study their functioning.

5.3.1. Introduction

This introduction functions as a basic description of the RGT 1S/60 assembly. A sectional overview of the RGT 1S/60 gas turbine is given in Figure 5.2 as a reference.

The compressor housing encloses the compressor rotor and main shaft bearing and directly functions as the main casing of the RGT 1S/60. There are two air intake passages formed at either side of the housing. The base is utilized as an oil sump, and the starter motor is installed on the underside. In addition an oil filler pipe, drain plug and an engine breather pipe are all incorporated within the housing. A supplementary mounting plate is attached to the front of the housing and comprises the fuel pump, the oil pump and main oil filter.

The main air casing is attached to the rear face of the compressor housing and ducts the pressurized air from the compressor to the combustion chamber. A single-can reverse flow combustor is secured on the front face of the air casing and consists of an outer air casing that encloses a flame tube. The spark plug is inserted into the outer air casing and secures the flame tube.

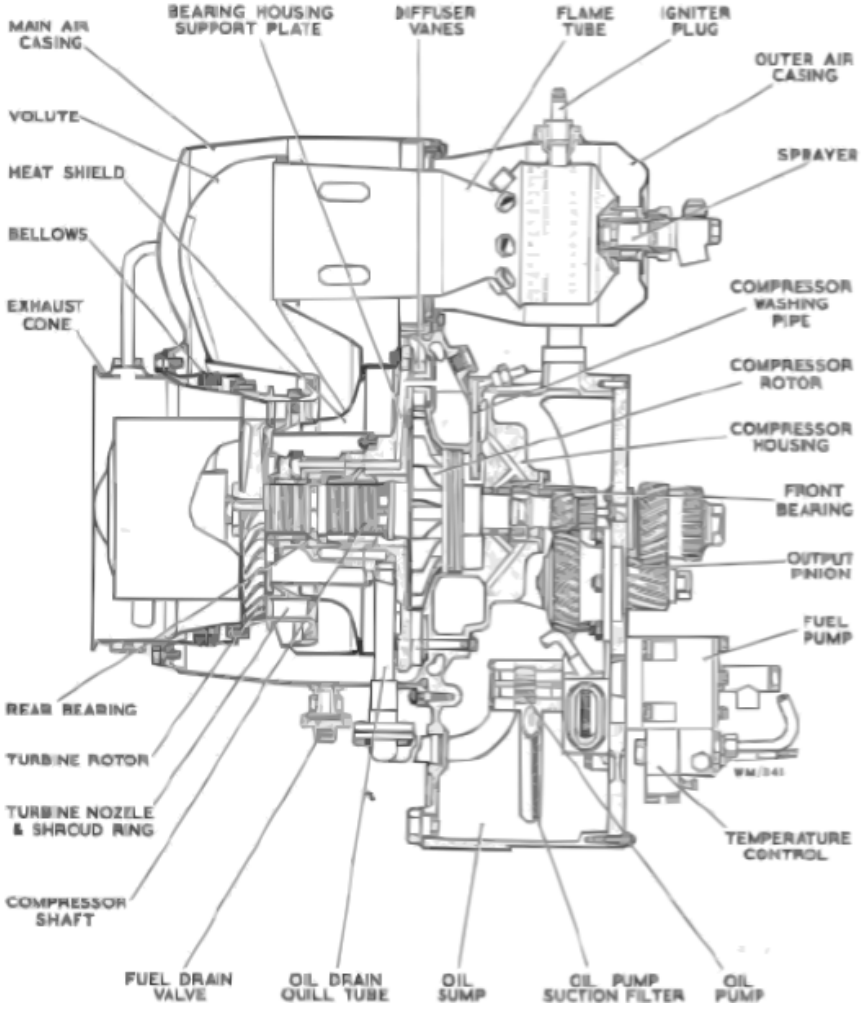

Figure 5.2: Sectional overview of the RGT 1S/60 gas turbine (Rover Gas Turbines Ltd, 1965*a*)

A fuel sprayer is situated into the head of the flame tube. Any possible accumulation of fuel is conveyed to a drain valve at the bottom of the main air casing which is normally open and closes under air pressure as the engine operates.

An inner spiral scroll casing ducts the gases from the combustor to the turbine stator and the shielded rear wall encloses a roller bearing that secures the turbine end of the main shaft. The turbine rotor is attached to the very end of the main shaft and is propelled by the gas flow that is directed through the rotor blades by the stator vanes.

5.3.2. Fuel pump

The mechanical fuel pump of the RGT 1S/60 is of a positive displacement type, which in theory works by having a cavity that expands on the suction

side and decreases on the discharge side. Liquid enters the pump on the suction side as the cavity expands, and later the liquid is discharged as the cavity contracts. For each cycle of operation the volume flow is constant since it will produce the same flow at any given rotational speed irrespective of the discharge pressure. Therefore it is advised not to operate the pump when the discharge side is obstructed because the pressure will build continuously until possible damage is done to the components. The fuel pump of the RGT 1S/60 is mounted externally and is driven through a coupling connecting the end of the rotor shaft with the pump drive gear in the auxiliaries gear train. The fuel pump comprises two separate chambers that are coupled with a small aperture and contain fuel at atmospheric pressure (Figure 5.3).

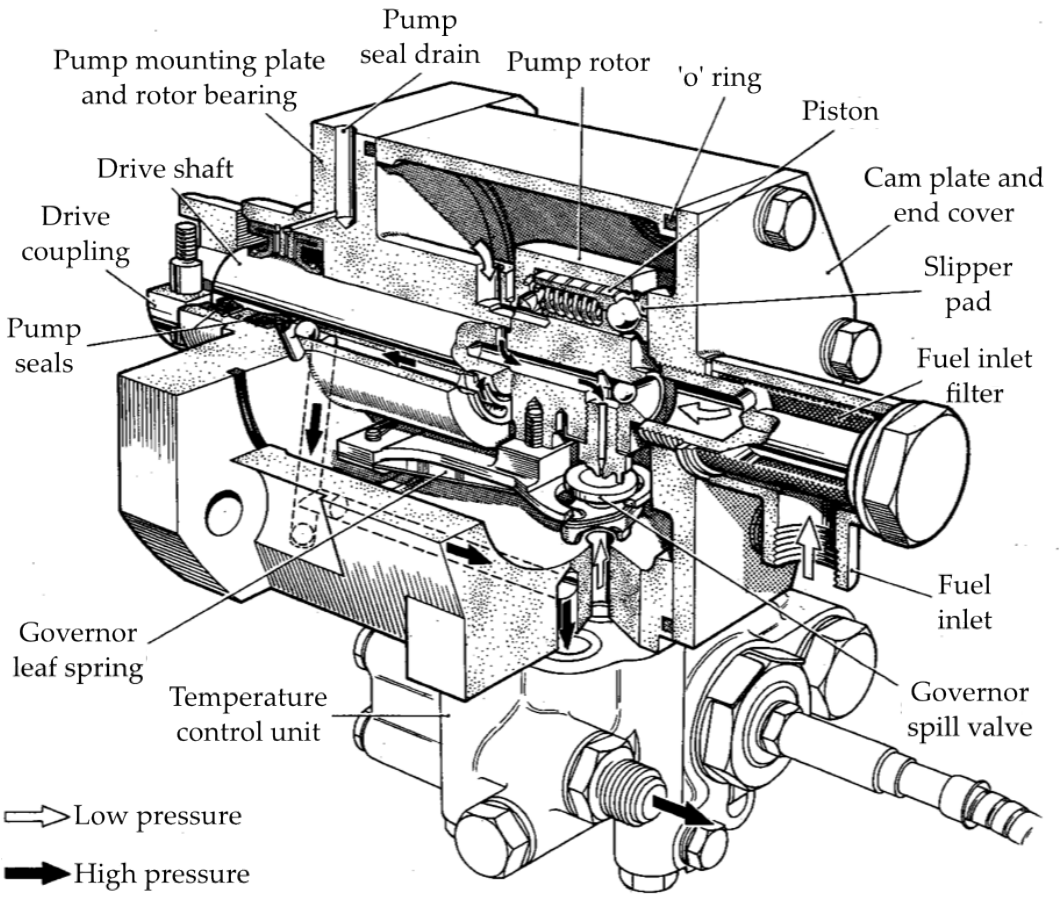

Figure 5.3: Sectioned view of the fuel pump (Rover Gas Turbines Ltd, 1965*b*)

The main chamber houses a drive shaft with a pump rotor at the end. Three small spring loaded pistons are equispaced around the axis of the pump

rotor. The pistons carry cup shaped slipper pads, held in position by the thrust of the spring, that ride on a circular tapered cam plate mounted on the backside of the pump end cover. As the cam face is at an angle the pistons are pushed towards the end of the piston bore for one half a revolution and away from it for the other half, initiating an axial motion in the piston bore which constitutes the pumping action. Each piston chamber in the pump rotor has a small cavity into the rotor bearing at its lowest point that is paired with an opening to the fuel in the main chamber. Consequently liquid flows into the opening as the suction side expands, and the liquid flows out of the cavity into internal drilling lines when the piston travel is compressed. As a result pressure is built in the discharge line of the fuel pump leading to the fuel sprayer. Because the positive discharge pump has the characteristic to endlessly increase pressure and no additional throttling method is available on the RGT 1S/60, the main shaft rotational speed will theoretically increase unlimited and components will fail. Hence a centrifugal speed governor is situated on the outer face of the rotor pump which is arranged to operate a half ball spill valve at a pre-determined datum. As the centrifugal force increases with speed, the leaf spring speed governor will eventually bend to bleed pressure and maintain operating speed. The other two sides of the outer face of the rotor carry balance weights. Some later type fuel pumps also include a second spring leaf overspeed governor serving as an emergency control with a somewhat higher datum.

The second chamber forms the bottom part of the fuel pump and functions as a temperature controller that acts when the EGT exceeds the predetermined maximum by bleeding off fuel from the high pressure side of the fuel pump into the chamber (Figure 5.4). The movement of a pivoting control lever that holds the ball valve is controlled by the expansion of a bourdon tube. A thermocouple filled with mercury is located in the exhaust stream and is connected to a capillary tube. If the EGT exceeds the pre-determined maximum the mercury will expand and transmit a pressure increase to the bourdon tube via the capillary tube.

The bourdon tube expands and acts against a spring that retains the control lever. The movement of the control lever opens the valve and reduces the fuel pressure. The temperature control will continue until the EGT lowers to the pre-determined level.

In conclusion, the fuel is fed into the main chamber of the pump where it is pressurized and discharged into the fuel sprayer supply line. In addition a speed governor prevents exceeding operating speed and a temperature control acts when the EGT overheats.

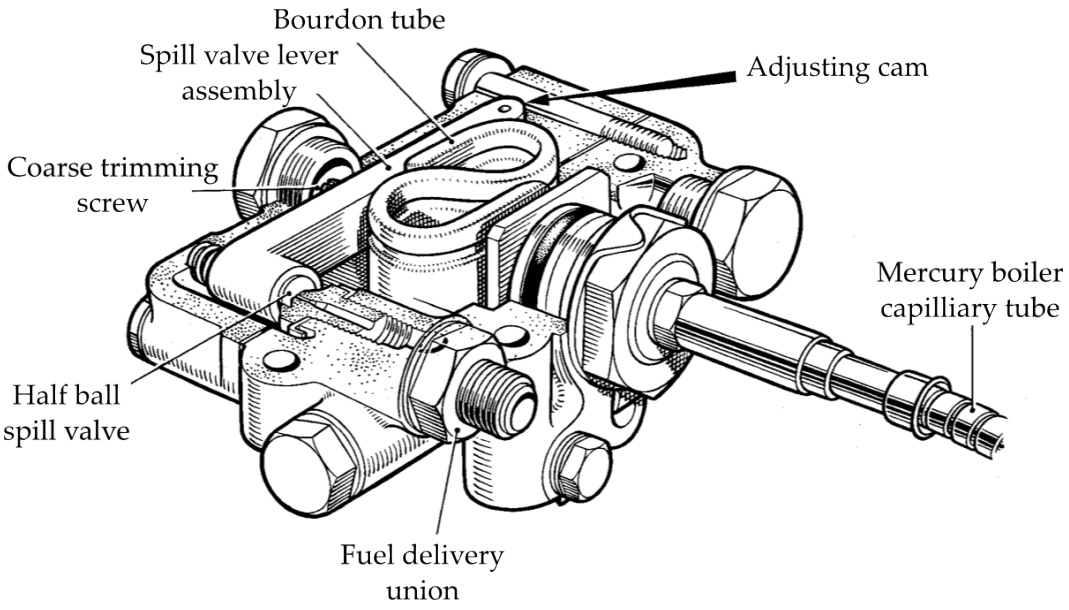

Figure 5.4: Internal view of the temperature control unit (Rover Gas Turbines Ltd, 1965*b*)

5.3.3. Fuel sprayer

Several different fuel sprayers and accumulators for the RGT 1S/60 are mentioned in the disassembly manual (Rover Gas Turbines Ltd, 1965*c*). The fuel sprayer type and joined accumulator that were available for the RGT 1S/60 is of the early type gas turbines. The fuel sprayer only has a barrel cam stop that controls a shut-off valve, therefore the fuel supply is either open or closed, hence the only speed control of the RGT 1S/60 is the mechanical speed regulator in the fuel pump (see Section 5.3.2). When the fuel sprayer body is open, the pressurized fuel passes through a filter into the atomiser. Thereafter the vaporized fuel is equally distributed by four uniform slots in the swirl plate which imparts a swirling motion before the finely atomised spray is released into the flame tube. Because a constant fuel flow is important for smooth gas turbine operation, the fuel accumulator assists in keeping the pressure and flow consistent. The fuel accumulator provides reserve pressure that will inhibit any fuel pressure irregularity from the fuel pump. In addition the fuel accumulator has a fuel bleed outlet to discharge fuel pressure after operating the gas turbine.

5.4. Experimental setup

The experimental setup is build in a test cell laboratory where the ambient temperature and atmospheric pressure vary lightly throughout the year.

Most tests were performed with an ambient temperature of 293 K and a pressure of 101 kPa; the computational models use the same ambient temperature and pressure conditions. Air is blown through the test cell by a large central fan during operation to keep the temperature down and prevent severe change in the ambient conditions that will effect the engine performance, in addition an extraction pipe is installed directly after the exhaust of the gas turbine to avoid recycling of exhaust gasses.

5.4.1. Test bench

The entire gas turbine setup required a rigid test bench to install and secure all components requisite for the experimental testing procedures. Therefore a steel test bench with U-shaped beams and cross-beams with a total size of 3 m by 0.9 m was allocated, as seen in Figure 5.5. An eddy-current Schenck dynamometer is positioned at the end of the test bench with the rear facing the control room. The flange of the dynamometer is connected to a drive shaft, which is protected by a shaft guard to contain the shaft in case of a failure. Following this the RGT 1S/60 gas turbine is placed on screw-jacks, level with the dynamometer, and is connected to the other side of the drive shaft. The inlet ducting is attached to the gas turbine, where the inlet is facing the control room to keep it as far from the exhaust gasses as possible and the conical section is supported by a bracket. Right after the exhaust an extraction pipe is installed to direct the exhaust gasses out of the test cell. The extraction pipe has a conical front part that allows ambient air to be sucked in and mix with the exhaust gasses which will reduce temperatures. Further, an instrumentation rack is installed on the test bench which accommodates measuring equipment, a spark plug charger to boost the spark and a relay to activate the starter motor.

As a precautionary measure the whole test bench is positioned perpendicular to the control room, allowing debris to sling sideways relative to the control room in the event of a component failure.

Rear left view

Front right view

Figure 5.5: Test bench setup

5.4.2. Fuel system

The operating fuel (kerosene) is supplied to the gas turbine by gravity feed. A stainless steel tank with a capacity of approximately 120 L is installed on the side wall of the test cell and is used for storage and supply. The supply feed at the bottom of the tank is controlled by a NC (normally closed) solenoid valve, followed by a hand valve for double safety. Fuel piping then carries the fuel to the test bench where it will flow through a filter and a fuel flow measuring device before it will be supplied to the fuel pump (for the fuel pump, see Section 5.3.2).

The fuel sprayer only has a barrel cam stop that controls a shut-off valve, therefore the fuel supply is either open or closed (see Section 5.3.3). This shut-off valve had to be controlled from inside the control room, since no one was allowed inside the test cell during experimental testing. As a solution a boat throttler was installed in the test cell because of its ability to both push and pull, i.e. either opening or closing the fuel sprayer valve (Figure 5.6).

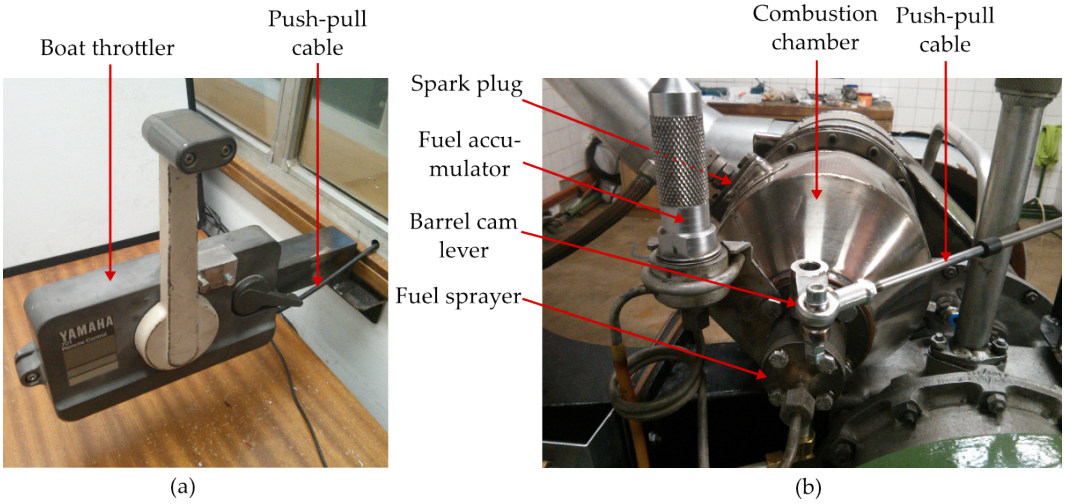

Figure 5.6: Boat throttler (a) and fuel sprayer (b)

As discussed in Section 5.3, the RGT 1S/60 gas turbine does not have a throttling function. The fuel sprayer is either open, or closed, and the fuel pump only has a speed governor to stabilise the rotational speed at 46 krpm operational speed. In an attempt to be able to regulate the fuel flow, and thus the rotational speed of the engine, a needle-valve system was selected (Figure 5.7). The needle-valve is installed in between the fuel pump and the fuel sprayer, and is preceded by a solenoid valve that is normally closed.

The needle-valve is connected to a DC electro motor which makes remote operation possible. The idea behind the use of a needle-valve is that by reducing the orifice the fuel flow can be restricted, and when less fuel is supplied to the combustion chamber the rotational speed will reduce. Two needle-valves were installed in parallel to have one on idle fuel supply and the other could be used for fuel control.

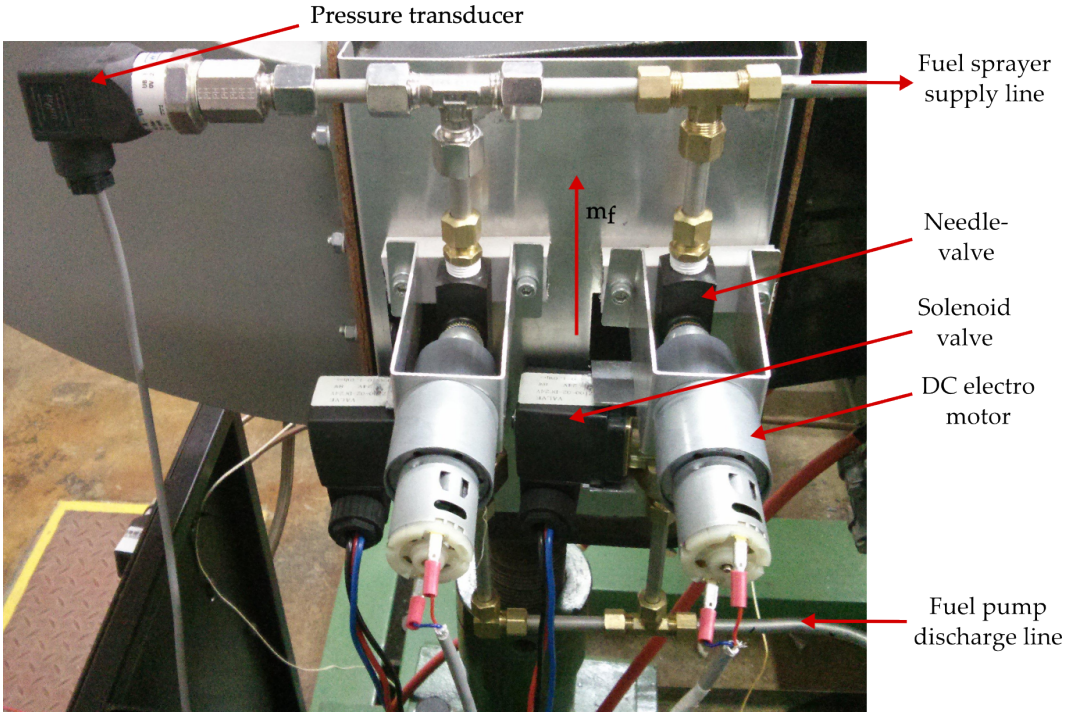

Figure 5.7: Needle-valve system

However in practice this system unfortunately failed due to the nature of the fuel pump. Whenever the needle valve was closed, and the RPM would drop slightly, the fuel pump responded by closing the speed governor. Consequently the fuel pressure would increase to its utmost value. Following this the needle valve simply acted as a venturi because of the high fuel pressure; the fuel flow would simply accelerate briefly. For future work the author recommends a controllable pressure drain to regulate the rotational speed by adjusting the fuel pressure accordingly.

5.5. Data acquisition

In order to monitor and record various parameters related to the operation of the gas turbine, a number of electrical and electronic apparatus were re-

quired. These include measuring instrumentation, relays, controllers, and solenoids which will be discussed in the following section.

5.5.1. Measuring instrumentation

The mass flow rate, temperature, rotational speed, fuel flow rate and static pressure values at various locations are measured while operating. Figure 5.8 shows a schematic of the locations where measuring instrumentation is used. The procedures used to calibrate the measuring equipment are discussed in Appendix D.3.

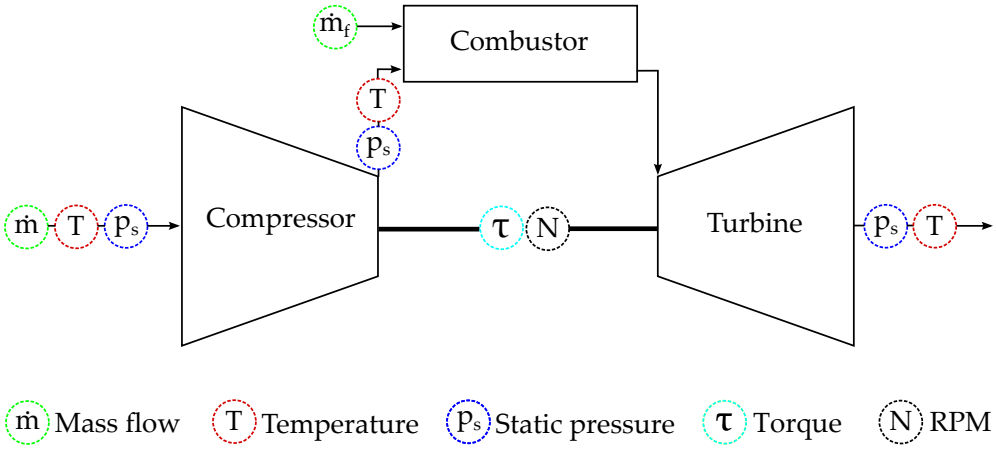

Figure 5.8: Data instrumentation on the RGT 1S/60

5.5.1.1. Air mass flow

The RGT 1S/60 gas turbine is provided with an intake system, designed by Prinsloo (2008), capable of accurate mass flow measurement. The single intake system consists of a conical inlet section that is followed by a diffuser which splits to feed the dual intakes of the Rover turbine. Prinsloo (2008) designed the intake system according to the *British Standard* (BS 848, 1997), which targets fan performance testing. Nevertheless, Prinsloo (2008) argued that the fundamental principals of evaluation were justified if the intake system was integrated in a gas turbine cycle.

The conical part of the intake system functions as a non-calibrated mass flow measuring tool, however a number of inlet characteristics set by the *British Standard* (BS 848, 1997) are to be met. Firstly the pressure ratio between the atmospheric pressure and the static pressure at the throat of the

conical inlet is required to be $p_r \geq 0.96$, i.e. Δp may not exceed 4 000 Pa. Secondly the Reynolds number (Re_d) at the throat of the conical inlet may not fall short of $Re_d < 20\,000$, and preferably exceeds $Re_d > 300\,000$ whereby a constant compound flow rate coefficient ($\alpha\epsilon$) may be applied in the *British Standard* (BS 848, 1997) mass flow rate calculation. Furthermore the uncertainty percentage in the reading of the differential pressure transducer must not exceed 1.5%.

To meet these requirements, Prinsloo (2008) iteratively calculated the diameter of the throat for the best compromise between size and accuracy. A summary of the dimensional sizing of the conical inlet is included in Table 5.3 (adjusted to Stellenbosch atmospheric conditions).

Table 5.3: Conical inlet parameters

Intake properties		Air properties	
Throat diameter [m]	0.11	γ	1.4
Throat area (A_0) [m^2]	0.0095	R	287
Mach number (Ma_0)	0.15	ρ	1.195
Mass flow rate ($\dot{m}$) [kg/s]	0.60	ν	1.51E-05
Velocity of flow (V_0) [m/s]	52.86	μ	1.81E-05
Static temperature (T_0) [K]	293.16	$\alpha\epsilon$	0.96
Static pressure (p_0) [Pa]	101325		
Total pressure difference (Δp) [Pa]	1811.56	< 4000	
Reynolds number (Re_d)	384819.03	> 300000	

The final design then agreed with the *British Standard* (BS 848, 1997) requirements and supports the mass flow rate calculation by the following expression:

$$\dot{m} = \alpha\epsilon \frac{\pi d^2}{4} \sqrt{2\rho_u \Delta p} \tag{5.5.1}$$

Where the pressure difference (Δp) is calculated at the throat of the conical inlet duct, using four static pressure taps (Figure 5.9).

5.5.1.2. Temperature

The gas temperature through the gas turbine stages is measured at three possible positions during operation. The temperature of the inlet air is determined by means of a K-type thermocouple positioned at one of the intake passages. The discharge temperature of the compressor stage is measured right after the diffuser again by means of a K-type thermocouple. For

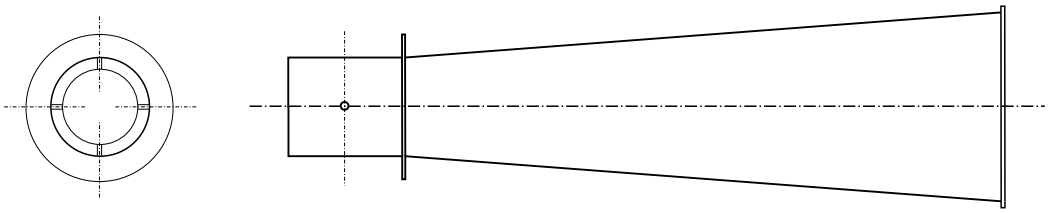

Figure 5.9: Four static pressure taps in the conical inlet duct

the Exhaust Gas Temperature (EGT) four thermocouples with heat resistant shielding were equispaced at the circumference of the exhaust. More K-type thermocouples are used to measure the temperature at the throat of the intake system and the oil temperature. In addition two J-type thermocouples are installed to measure the cooling water temperature of the dynamometer.

The K-type thermocouple is used for most temperature readings because of its accuracy and reliability. The K-type thermocouple is accurate within 1.7 °C and has a sensitivity of 41 μV/°C. The temperature range of the cooling water is low, therefore the J-type thermocouple was selected which has a lower temperature range but in return has a higher sensitivity of 50 μV/°C. No thermocouple has been positioned after the combustor due to issues with the geometry of the gas turbine and possible carbon related problems.

5.5.1.3. Static pressure

The static pressure is measured before and after the compressor stage, using a WIKA A-10 type pressure transducer. Another A-10 type transducer is used to measure the static pressure at the exhaust. Furthermore the same pressure transducer is used to measure the pressure of the fuel right before the fuel sprayer, and the oil pressure after the oil pump. The WIKA A-10 type pressure transducer has an accuracy of $\pm$0.5% and, to keep the absolute error margin as small as possible, the pressure range for all pressure measurement locations was individually selected based on the performance estimation in Section 5.2.4.

Besides the static pressure transducers, a WIKA A2G-50 differential pressure transmitter is used to calculate the static pressure difference between the intake throat and the atmospheric pressure in the test cell. The pressure transmitter has a measuring range of 0-7 kPa and an accuracy of $\pm$1.5%.

Ideally the static pressure should be measured in the vaneless radial passage and at multiple positions of the diffuser. However due to the age of the gas turbine it was decided not to modify the existing parts, and only in-

troduce static pressure measurement taps when the new compressor would be installed.

5.5.1.4. Rotational speed and torque

The rotational speed of the main shaft of the RGT 1S/60 was measured with a variable reluctance (VR) speed sensor, located at the rear of the Schenck dynamometer used for this thesis.

The VR speed sensor was installed facing a rotating toothed trigger wheel (Figure 5.10). The individual teeth of the rotating wheel influence the magnetic flux in front of the sensor pole piece. As the magnetic field deforms, an AC voltage is induced in the coil surrounding the permanent magnet. The magnitude of the induced voltage is proportional to the speed of the toothed wheel, and thus the speed of the dynamometer. Because the RGT 1S/60 gas turbine has a build-in reduction gearbox, the rotational speed of the dynamometer had to be multiplied with the gearbox ratio to get the main shaft speed.

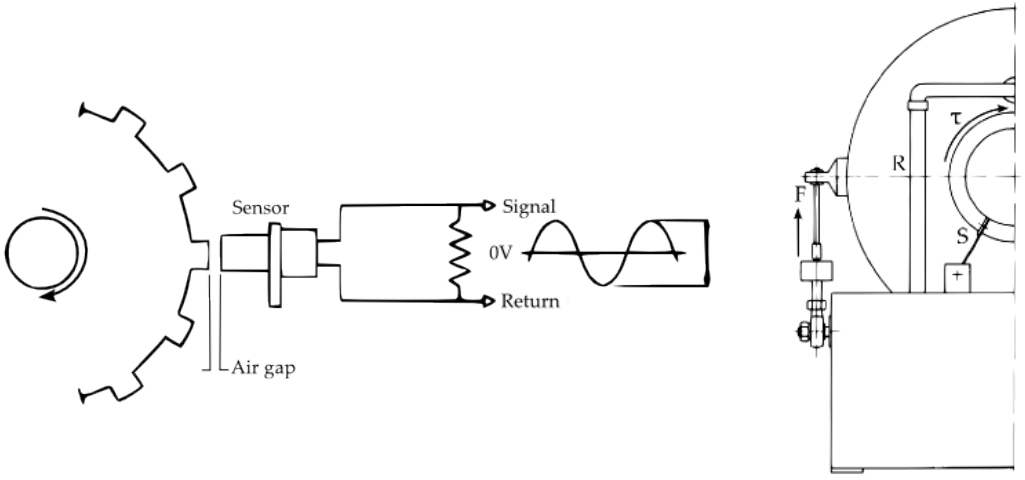

Figure 5.10: Speed sensor and load cell principle (SCHENCK Pegasus GmbH, 1997)

The generated torque was measured using a load cell which was installed on a torque arm at a distance R from the centre of the dynamometer (Figure 5.10). The load cell transducer provides an electrical signal that is proportional to the torque.

5.5.1.5. Fuel mass flow

For fuel flow measurement a DFM-50C-K is incorporated in the fuel system. It features indication in: actual flow [l/h], total fuel consumption [l], and

operating time [t]. One of the downsides of the control system was the lack of channels to capture signals for every measuring instrument, and because the fuel flow data was the least valuable, it was not connected to the control system. Because the fuel flow meter is equipped with a screen that shows the required data, a camera was directed at the display to monitor the fuel flow. The RGT 1S/60 gas turbine used approximately 34 l/h at its operation point, which is close to the estimated value of 36 l/h using Equation 5.2.7.

5.5.2. Control cabinet

The controllers that were used for the experimental setup were installed in a 19" cabinet in the control room that includes the dynamometer control unit, power supply to the dynamometer, and a Programmable Logic Controller (PLC). An Allen Bradley MircoLogix1200 PLC was used to monitor the various parameters that were measured by the instrumentation. Furthermore a program called ETA (engine test automation) from Cape Advanced Engineering was used to communicate with the PLC (Appendix D.1). The Allen Bradley MircoLogix1200 PLC is shown in Figure 5.11.

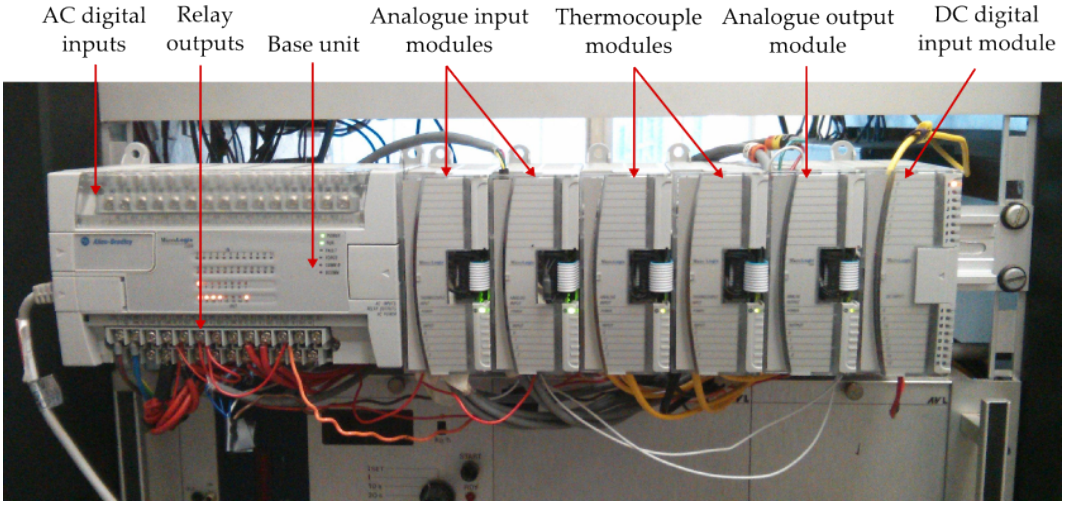

Figure 5.11: PLC; main CPU and separate modules

The PLC was connected to mains power and the base unit CPU was powered by 24 V DC, all individual expansion modules use the base unit as a power source. The relays of the base unit were used to control separate relays in the electrical circuits of the starter motor, the spark plug, and the solenoids in the fuel system. In addition a master relay was used to immediately cut off the fuel supply to the gas turbine by closing all solenoids.

The analogue input modules were used for all measurement instrumentation related to the pressure, speed, and torque. The input to the modules is a 4 - 20 mA analogue output signal from the pressure transducers and 0-10 V for the speed and torque measurements. The output signal 4 - 20 mA is selected because current output offers a higher noise immunity and the instrumentation can be positioned further away from the PLC without influencing the data.

To prevent difficulties with replacing a defective thermocouple, a junction box was installed in the test cell. Following this the extension wires were run from the junction box to the thermocouple input modules of the PLC.

The analogue output module was used to send commands to the controller of the dynamometer. A physical emergency stop button was hard-wired to the DC digital input module. The physical emergency stop button is connected in series to the master switch of the ETA and all solenoid valves, and is an extra precaution in case of faulty or lagging computer controls.

5.6. Data processing

The user interface program ETA (see Appendix D.1) records all experimental data during operation and saves the outcome in an Excel file, hence all further gas turbine performance characteristics are computed and plotted in Excel.

Due to the error percentage of the measuring instrumentation it was considered necessary to perform an uncertainty analysis to determine the accuracy or quality of the test results. The static pressure transducers are directly connected to the PLC and the results showed no signs of noise that would effect the measuring data, therefore the use of a time-averaged value of the static pressure was valid. The static pressure results will have an uncertainty percentage of $\pm 0.5\%$. Similarly the differential pressure transmitter has an uncertainty of $\pm 1.5\%$. The thermocouple measurements are directly connected to the PLC and were therefore time-averaged, considering a ± 1.7 °C uncertainty. The mass flow rate and efficiency calculations are dependent on the relative effect of both temperature and pressure reading uncertainty. Therefore the mass flow rate and efficiency values have an uncertainty of 1% and 0.75% at the expected value respectively.

5.7. Results

The RGT 1S/60 gas turbine start-up is relatively straight forward (see Appendix D.2.2.1). The gas turbine will spool to its operating speed of 46 krpm, then the speed governor in the fuel pump will activate to keep the gas turbine RPM stable at the operating point. The gas turbine is not designed to adjust the fuel flow and the system that was selected to alter the fuel flow failed due to the nature of the fuel pump (see Section 5.4.2), therefore the rotational speed cannot be adjusted. Only a single working value at operation point can be obtained. Hence the gas turbine spool-up from starter motor deactivation to operating speed is used to create the actual working line of the compressor.

Figure 5.12 shows the similarity of the total-to-static pressure ratio during the start-up process between three consecutive experimental runs. The start-up procedure seems to be similar for all runs above a pressure ratio of 1.6, but a minor difference in characteristic is observed below that pressure ratio. Because the starter motor is disconnected manually, the data might have been influenced by irregular starter motor deactivation.

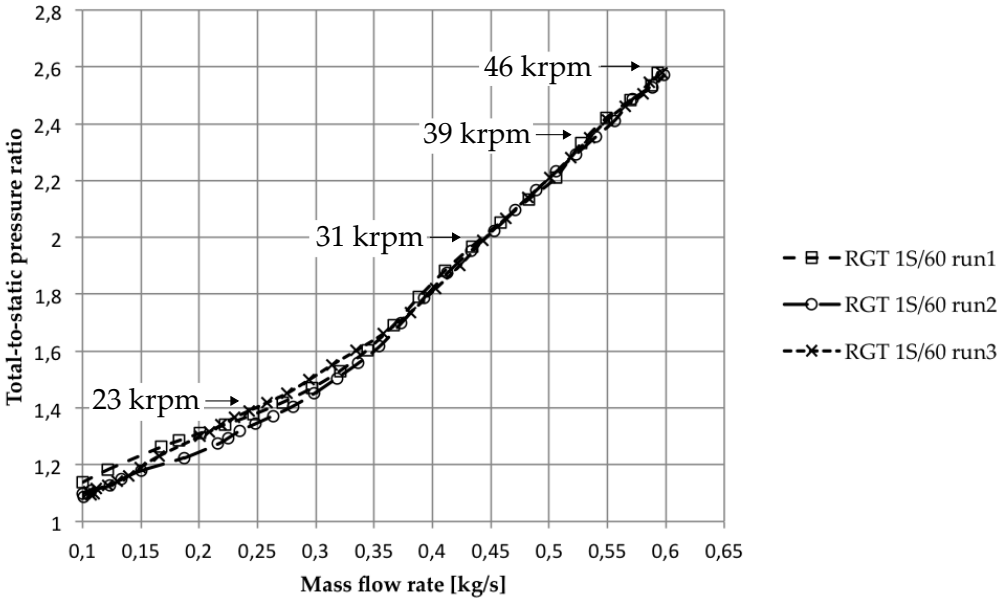

Figure 5.12: Comparison of the start-up process of multiple runs

The experimental data at operating point is displayed in Appendix D.4.

6. Compressor Performance Evaluation

6.1. Validation of the standard compressor CFD results

The CFD results of the standard compressor were validated against the experimental data of the RGT 1S/60 compressor (Figure 6.1). Because the RGT 1S/60 only operates at 46 krpm, the CFD simulations are only performed at this rotational speed. Since the outlet boundary of the computational domain in CFX® is static pressure imposed, several simulations are run to achieve a mass flow that corresponds to the experimental mass flow rate.

The compressor of the RGT 1S/60 is not equipped with a volute, instead a 90° bend is situated directly after the diffuser blade to direct the air flow into the axial direction. The compressed air is then discharged in the outer casing of the gas turbine. The static pressure is measured at two pressure taps located on either side of the outer casing of the RGT 1S/60. In order to compute the static pressure at the same location, the whole outer and inner casing would have to be modelled, which would drastically increase computational time. It was therefore decided not to model the entire engine, and to just include a small pinched radial section at the diffuser discharge of the computational domain (Figure 4.3). Therefore the static pressure of the experimental data would most likely not correspond completely to the computed values in CFX®-Post.

Table 6.1 indicates the compressor discharge conditions for experimental and CFD data. As expected the static pressure value that is measured in the experimental setup deviates from the static pressure computed by CFX®. The static pressure of the experimental data is somewhat higher than the CFD predictions, most likely due to further diffusion in the outer casing of the RGT 1S/60. The static pressure value obtained from CFD is approximately 2.5% lower than on the experimental measurement. Hence if the CFD value is compensated for the location where the value is computed,

the increase in static pressure would still result in an acceptable difference.

Table 6.1: Compressor discharge conditions for experimental and CFD data at operating point

	Exp.	CFD	Δ
Total discharge pressure ($p_{t,4}$) [kPa]	271.06	271.88	0.82
Static discharge pressure (p_4) [kPa]	260.07	253.61	6.46
Total-to-total isen. efficiency ($\eta_{TT,1-4}$)	61.24%	63.83%	2.59%

The total pressure of the experimental test data is calculated by adding the dynamic pressure to the static pressure reading. The difference in location of the static pressure measurements influences the deviation in total pressure and efficiency values.

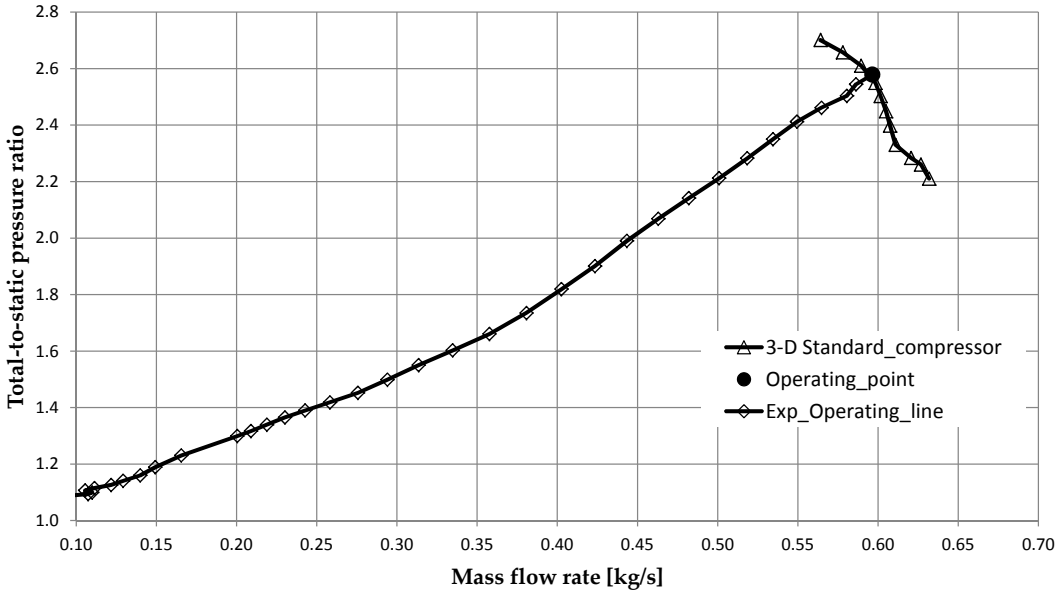

Figure 6.1: RGT 1S/60 total-to-static performance map

The total-to-total isentropic efficiency is calculated from the experimental data using the static pressure ratio and total temperature ratio, defined as (Baskharone, 2014):

$$\eta_{TT,1-4} = \left[\left(\frac{p_4}{p_1}\right)^{(\lambda-1/\lambda)} - 1\right] / \left[\left(\frac{T_{t,4}}{T_{t,1}}\right) - 1\right] \tag{6.1.1}$$

6.2. Modelling results and discussion

6.2.1. Overall compressor performance

The performance of the new compressor design was initially evaluated in CompAero using CENCOM by predicting the aerodynamic performance of the new compressor stage, and then simulated in CFX®. Table 6.2 supplies the 1-D and CFD overall performance estimates, from the impeller inlet (1) to diffuser discharge (4). In addition Figure 6.2 and Figure 6.3 exhibit the overall pressure ratio and efficiency respectively. From the figures it is obvious that the new compressor out-performs the standard compressor design, both the estimated pressure ratio and efficiency values show significant improvements.

The 1-D result and CFD results for the new compressor differ slightly at design point. The 1-D results predict a higher total-to-static pressure recovery compared to the CFD results, however the 1-D simulations predict a lower static pressure at the discharge of the impeller. The compressor efficiency predictions of the 1-D simulations at operating point are higher than the CFD values, but for the impeller the CFD predicts a higher efficiency at operating point. The 1-D analysis predicts a significantly larger operating range for the new compressor than the CFD simulations. These trends were also found by Krige (2013) who predicted the performance of several radial diffusers using CompAero for 1-D simulations and a CFD software package for 3-D analysis. Nevertheless both 1-D and CFD analysis of the new compressor clearly show a performance improvement over the CFD results of the standard compressor (Table 6.2).

Table 6.2: Overall compressor performance

Compressor	Standard		New	
	CFD	Exp.	1-D	CFD
Pressure ratio ($p_4/p_{t,1}$)	2.50	2.58	3.25	3.30
Pressure ratio ($p_{t,4}/p_{t,1}$)	2.68	2.68	3.40	3.44
Isentropic efficiency ($\eta_{TT,1-4}$)	63.83%	61.24%	86.65%	85.55%

The increase in total pressure by the new impeller design is evident in the results, in the same way as the improved total-to-static pressure ratio indicates the improved static pressure recovery of 0.65 predicted by VDDESIGN for the new design, compared to 0.54 for the standard diffuser (see Table 3.7).

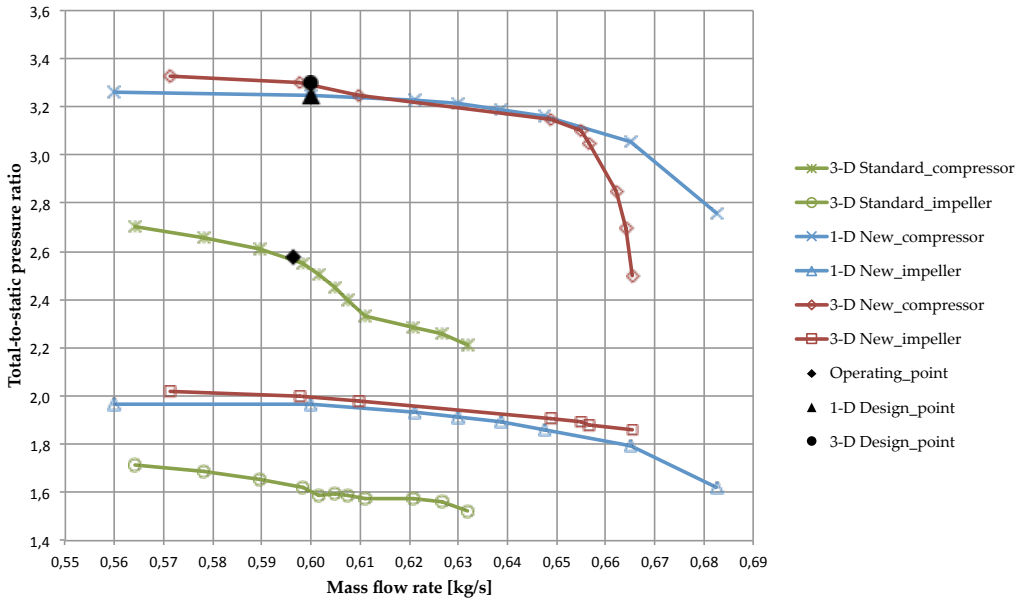

Figure 6.2: Total-to-static pressure ratio of the compressors

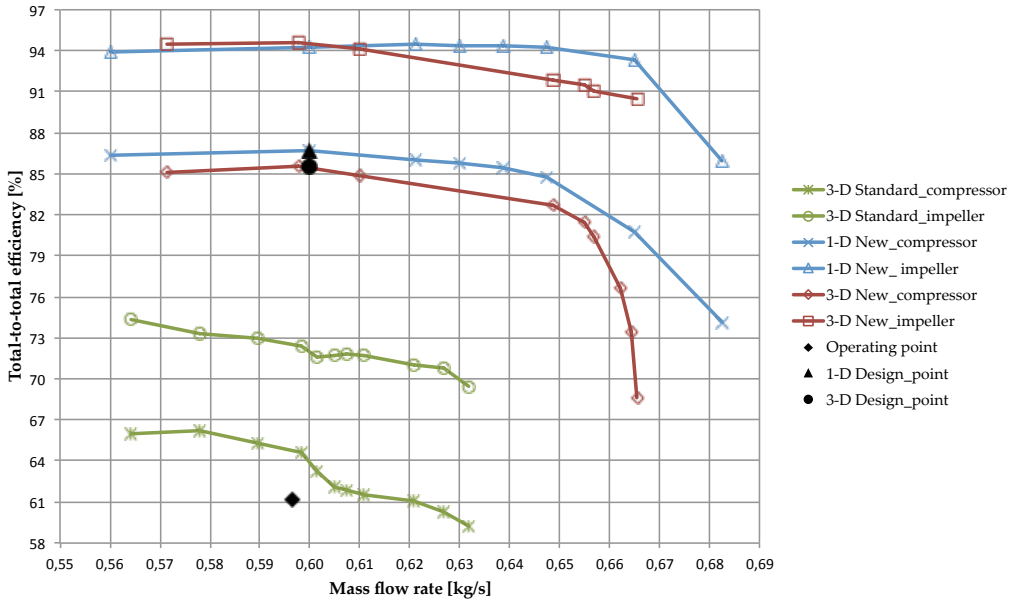

Figure 6.3: Total-to-total efficiency values of the compressors

6.2.2. Modelling results

After the numerical simulations of the standard and new compressor were conducted, the 3-D modelling results at operating point were analysed with CFX®-Post. A top view of the Mach number contour is shown in Figure 6.4. The recirculation region in the flow passage of the impeller and the separation region from the diffuser vane of the standard compressor are clearly visible, and explains the difficulty with convergence and mass flow balance.

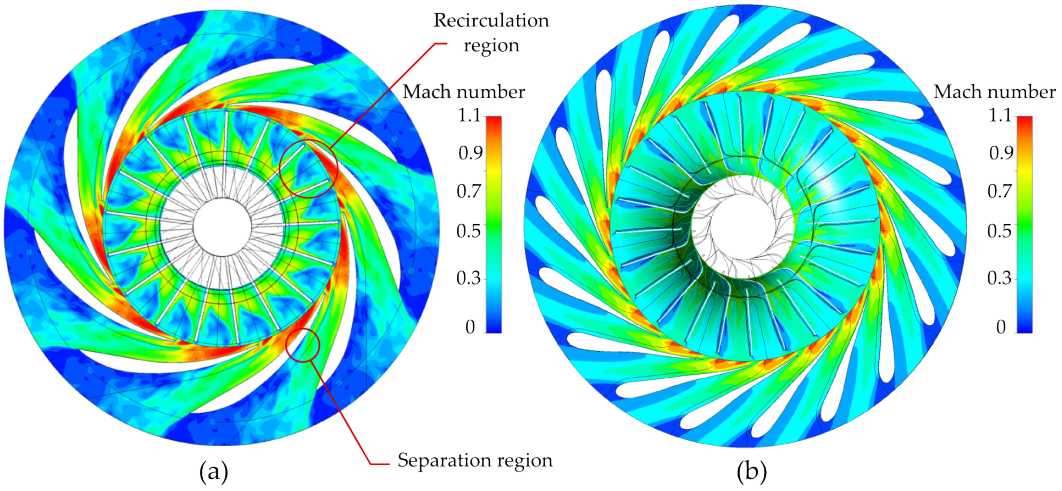

Figure 6.4: Mach number of the standard compressor (a) and the new compressor (b)

Focusing on the standard compressor analysis, a visual inspection of the 3-D results show a distorted flow in the impeller passage. Strong vortices are visible over the entire through-flow of the impeller passage starting just after the leading edge of the blade suction side (Figure 6.5.a).

Downstream of the impeller tip, the 1-D analysis performed on the standard diffuser predicted a mismatch between the flow and the diffuser vane angle at 50% span at the operating point. The 3-D modelling confirmed the mismatch at the diffuser inlet, as shown in Figure 6.5.b. The Mach number of the flow in the vaneless radial passage was high at the impeller tip, consequently the 3-D analysis results show a supersonic region in between the leading edge of the diffuser and the throat at operating point (Figure 6.6).

Recirculation at the diffuser vane was predicted over the entire operating range from 0.57 kg/s $\leq \dot{m} \leq$ 0.67 kg/s by the 1-D analysis. Inspecting the 3-D results confirmed substantial recirculation at the operating point at the

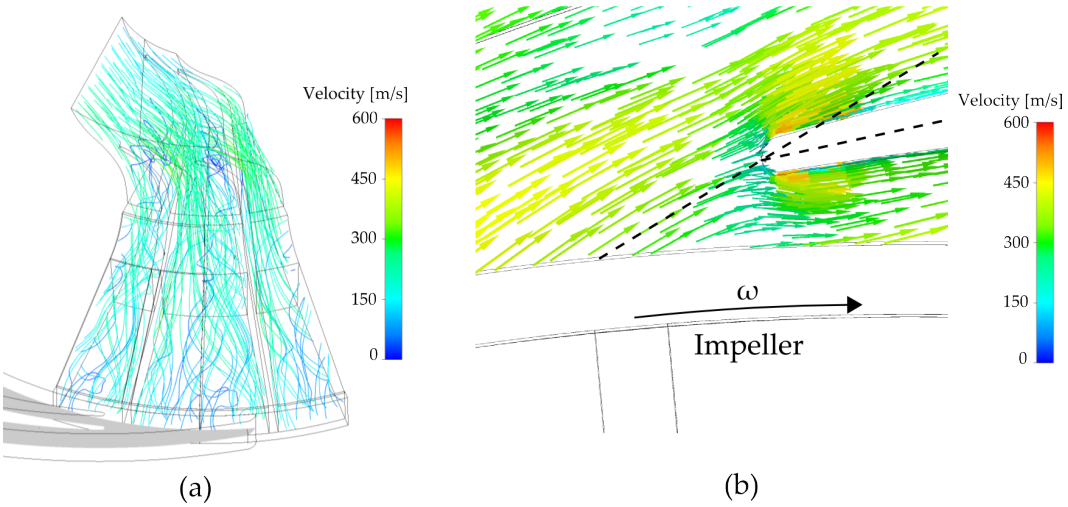

Figure 6.5: Distorted flow in the through-flow passage of the standard compressor (a), velocity vectors at the diffuser inlet to exhibit the mismatch between the flow and the blade angle (b)

suction side of the diffuser vane, as exhibited in Figure 6.6. The low Mach number in the stationary frame of reference and the velocity vectors both indicate severe recirculation in the standard diffuser over approximately 75% of the suction side of the diffuser vanes at the operating point. The Mach number seems particularly high close to the diffuser vane leading edge which suggests that the mismatched inlet flow and diffuser vane angle causes local acceleration.

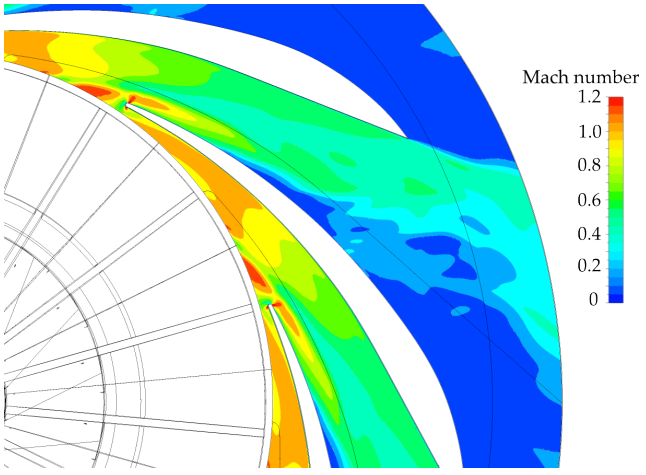

Figure 6.6: Low Mach region indicates recirculating flow at the suction side of the standard diffuser vane at 50% span at operating point

In conclusion the numerical modelling of the standard compressor predicted strong vortices in the impeller passage, a mismatched flow at the diffuser inlet and recirculation at the suction surface of the diffuser.

Focusing on the new compressor design, low relative velocity regions were predicted over about 50% of the main blades suction surface as shown in Figure 6.7. The flow separation causes a small recirculation region.

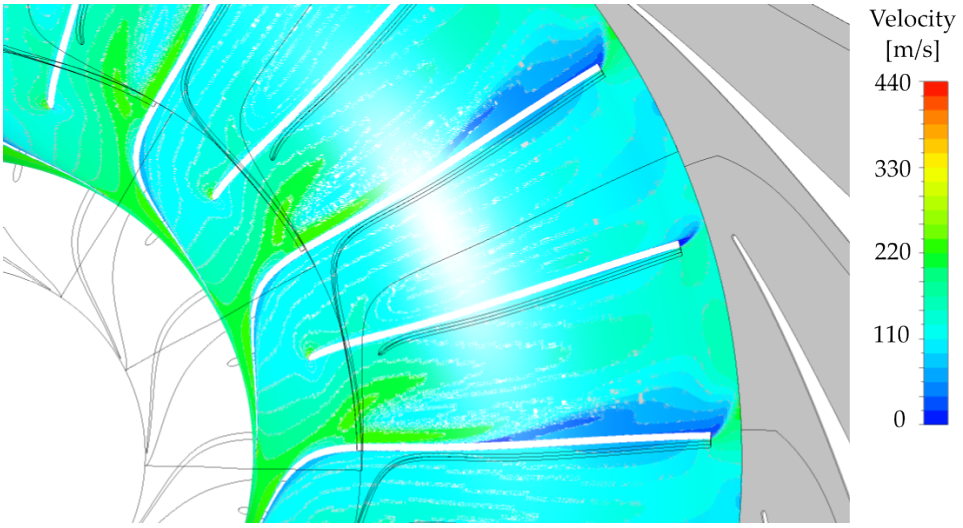

Figure 6.7: Low velocity region at the main blade suction side at 50% span at the operating point

The 3-D modelling predicts supersonic regions in the vaneless radial passage from the diffuser vane leading edge to the throat (Figure 6.8). The supersonic regions are similar to the high Mach regions found in the standard compressor (see Figure 6.6), however the high Mach numbers dilute quicker due to a shorter region from the diffuser vane leading edge to the throat. Recirculation is predicted close to the hub of the diffuser vane at the leading edge due to flow misalignment, as shown in Figure 6.8. Separation is predicted at the trailing edge of the vane from hub-to-shroud, shown in Figure 6.8 and Figure 6.9. Shum *et al.* (2000) however observed that no heavy separation takes place when the fluid flow angle misaligns with only some of the span, e.g. near the hub or the shroud. At 50% span the 3-D simulations exhibit separation only at the diffuser discharge. As shown in Figure 6.9 low Mach regions arise around 30% span and increase to the hub. Aungier (2000) noted that some level of separation in the boundary layer of the diffuser vane will always be visible when designed for maximum pressure recovery.

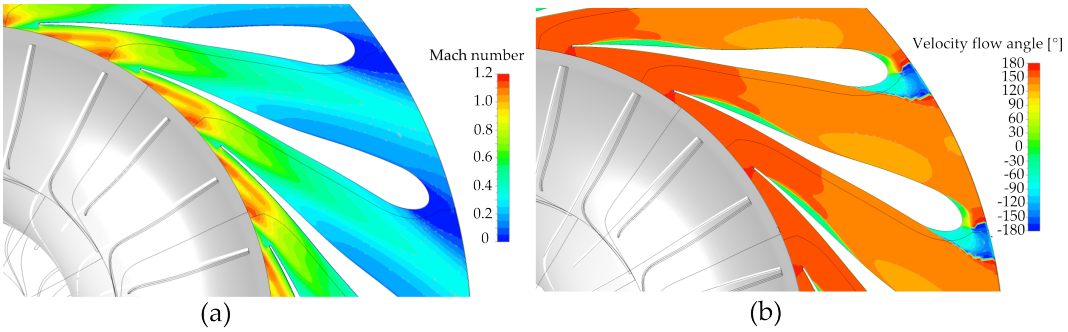

Figure 6.8: High Mach number flow at the diffuser inlet and throat at 50% span and operating point of the new compressor (a). The angle between the flow and the theta direction perpendicular to the leading and trailing edge of the vanes, i.e. velocity flow angle, shows recirculation along 50% of the suction side of the vane starting at the leading edge at 20% span (b)

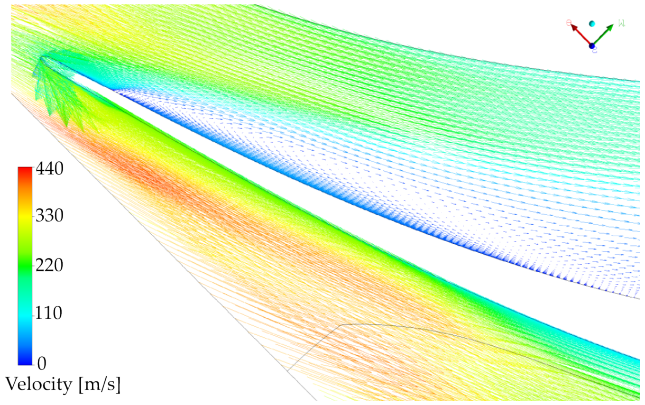

Figure 6.9: Low Mach number region at the main blade suction side of the new impeller at 30% span at the operating point

In order to attain performance improvement of the centrifugal compressor without having to change the turbine stage of the RGT 1S/60, the input power, or torque, would have to remain the same. The compressor power input is defined using the following equation (Boyce, 2002):

$$W_c = \frac{\dot{m}\,(h_2 - h_1)}{\eta_c} \tag{6.2.1}$$

The performance estimates in Section 5.2 were used to calculate the input power of the standard compressor, and served as a benchmark for the new

centrifugal compressor design. The power input value and the related parameters of the standard compressor benchmark and the new compressor design are exhibited in Table 6.3.

Table 6.3: Power input estimates of the standard and new compressor

Parameters	Standard comp.	New comp.
Inlet temperature ($T_{t,1}$) [K]	293	293
Discharge total temperature ($T_{t,2}$) [K]	445.17	428.82
Total-to-total pressure ratio (p_2/p_1)	2.8	3.44
Isentropic efficiency ($\eta_{TT,1-4}$)	70.6%	85.55%
Input power (W_c) [kJ/kg]	144.14	146.50

After the CFD analysis of the standard compressor was completed the power input was predicted to be 148.4 kJ/kg, and the experimental tests results indicated a power input value of 155.8 kJ/kg. The power input value from the experimental tests is significantly higher than the set benchmark, probably as a result of wear and a consequential decrease in efficiency. Nevertheless the CFD analyses indicate a small but appropriate deviation between the two designs. The deviation between the input power of the new compressor and the benchmark was considered acceptable.

7. Conclusions and Recommendations

This thesis was performed with the objective to analyse, assess and redesign the centrifugal compressor of the RGT 1S/60 to attain a better performing compressor stage. Because the turbine design of the RGT 1S/60 was to be kept unchanged, it was of importance that the input power, or torque, would remain the same. Therefore both an increase in pressure ratio and an improved efficiency value were design targets.

7.1. Conclusions

The CompAero 1-D software package helps the designer to achieve the best possible centrifugal compressor design, if the designer adheres to the design parameters specified by Aungier (2000). These design parameters are particularly critical for the VDDESIGN program to configure the vaned diffuser. The design criteria include: the effective divergence angle, the area ratio, and the blade loading parameter. Aungier (2000) warns of a deterioration in compressor performance if these criteria are not met.

The design of the centrifugal compressor does not comply with some of these criteria, as seen in Table 3.7, because of bolt orifices that compromised the design. However, even with the blade shape not conforming to the standard thin/airfoil type, the preliminary design created with the 1-D software package directly provided meaningful results when 3-D CFD analysis was performed. Care should be taken when considering the choke and stall margins predicted by CompAero, as these limits are optimistic relative to the CFD results (see Figure 6.2).

The combination of the software packages CompAero and CFX® proved to speed up the analysing process of the centrifugal compressor performance. The inclusion of a preliminary 1-D design stage had a considerable benefit in saving computational time when identifying the effects of interaction in-

duced alterations in blockage, loss and slip on the compressor performance.

Since the turbine blade of the RGT 1S/60 gas turbine will remain unchanged, the power input of the standard compressor was set as a benchmark for the new compressor design. The power input of the new centrifugal compressor design was predicted to deviate by only 1.6% from the set benchmark (Table 5.2), therefore the design was considered appropriate for the experimental setup.

The CFD results of the standard compressor indicate strong vortices in the impeller passage, a mismatched flow at the diffuser inlet and strong recirculation at the suction surface of the diffuser. The new diffuser design on the other hand successfully eliminates those instabilities and significantly improves the compressor stage performance (Table 6.2). When comparing the CFD results of the standard compressor and the new compressor, the new design achieves an increase in total-to-static pressure ratio from 2.5 to 3.3 at 46krpm and ambient conditions of 293 K and 101 kPa. For the total-to-total efficiency of the compressor stage an increase from 63.8% to 85.6% is predicted. Both these values exceed the set targets in Section 3.3, but still comply with the objective to keep the input power the same.

The experimental tests were performed on the standard configuration of the RGT 1S/60 and compared to the CFD predictions, even though the location of static pressure measuring point was not identical to the computational outlet. Concluding from the values in Table 6.1 the CFD analysis underpredicts static pressure. Considering that the outlet of the CFD computational domain is directly after the diffuser, a moderate increase in static pressure is expected when the flow is further diffused in the outer casing of the gas turbine where the experimental measurement takes place. Therefore the correlation between the experimental data and the computational results was deemed satisfactory.

7.2. Recommendations

Additional design work is required to create a shroud cover for the new compressor to fit the RGT 1S/60 gas turbine housing. The bolt slots in the disc that secures the diffuser have to be repositioned to fit the new diffuser vane design; the new diffuser design accommodates the bolts that fasten the entire compressor to the gas turbine housing. Lastly the new impeller and diffuser design models have to be prepared to fit the main shaft and gas turbine housing respectively.

The author recommends the following items for future work related to the new centrifugal compressor design and the experimental setup:

- Further work can be done on the centrifugal compressor design by optimizing the design to attain maximum performance gains at the compressor design point.
- Dismantling the RGT 1S/60 before the compressor is manufactured to ensure that the geometry parameters acquired from the CAD file are correct, and that the new design complies with the geometry criteria.
- The addition of several data measuring points in the new compressor configuration to get a more accurate comparison between the experimental and computational data.
- Regarding the experimental setup a revision of the fuel system. The ability to vary the rotational speed of the gas turbine will increase the potential research that can be performed using the RGT 1S/60. To manage the rotational speed a fuel system that adjusts the fuel pressure accordingly, instead of the fuel flow rate. Hence the sudden increase in fuel pressure which results from the speed governor can be suppressed.
- A pressure bleed valve to be installed in between the fuel pump and the fuel sprayer. The bled fuel will be redirected to the fuel tank. Being able to remotely control and monitor the pressure bleed is a must.
- To improve safety in the test cell the glass windows in the control room should be reinforced by either installing impact resistance glass, or other protective measures in front of the glass window without compensating visibility.
- Due to the substantial increase in pressure it is advised to further analyse the effect on the combustion system.

List of References

Anish, S. and Sitaram, N. (2009 March). Computational investigation of impeller-to-diffuser interaction in a centrifugal compressor with different types of diffusers. *Proceedings of the Institution of Mechanical Engineers, Part A: Journal of Power and Energy*, vol. 223, no. 2, pp. 167–178. ISSN 0957-6509.

ANSYS Inc. (2012*a*). User manual: ANSYS CFX introduction v14.5; Turbulence.

ANSYS Inc. (2012*b*). User manual: ANSYS Meshing introduction v14.5; Mesh quality.

Arunchalam, V., Nagpurwala, W., Deshpande, M. and Shankapal, M. (2008). Numerical Studies on the Effect of Impeller Blade Skew on Centrifugal Compressor Performance. *International Conference on Thermal Engineering*, pp. 567–572.

Aungier, R.H. (2000). *Centrifugal compressors: a strategy for aerodynamic design and analysis*. 1st edn. The American Society of Mechanical Engineers.

Aungier, R.H. (2003). *Axial-Flow Compressors: a strategy for aerodynamic design and analysis*. 1st edn. The American Society of Mechanical Engineers.

Aungier, R.H., Direnzi, G.L. and Hohlweg, W.C. (1993). Comparison of Conventional and Low Solidity Vaned Diffusers. , no. ASME Paper No. 93-GT-98.

Baskharone, E.A. (2014). *Principles of Turbomachinery in Air-Breathing Engines*. 1st edn. Cambridge University Press.

Bennett, I., Tourlidakis, A. and Elder, R.L. (2000 January). The design and analysis of pipe diffusers for centrifugal compressors. *Proceedings of the Institution of Mechanical Engineers, Part A: Journal of Power and Energy*, vol. 214, no. 1, pp. 87–96. ISSN 0957-6509.

Boncinelli, P., Ermini, M., Bartolacci, S. and Arnone, A. (2007 November). Impeller-Diffuser Interaction in Centrifugal Compressors: Numerical Analysis of Radiver Test Case. *Journal of Propulsion and Power*, vol. 23, no. 6, pp. 1304–1312. ISSN 0748-4658.

Boyce, M.P. (2002). *Gas Turbine Engineering Handbook*. 2nd edn. Gulf Professional Publishing. ISBN 0884157326.

BS 848, B.S. (1997). Fans for general purposes - Part 1: Performance testing using standardized airways.

Came, P.M. and Robinson, C.J. (1998 February). Centrifugal compressor design. *Proceedings of the Institution of Mechanical Engineers, Part C: Journal of Mechanical Engineering Science*, vol. 213, no. 2, pp. 139–155. ISSN 0954-4062.

Clements, W.W. and Artt, D.W. (1987 June). The influence of diffuser channel geometry on the flow range and efficiency of a centrifugal compressor. *Proceedings of the Institution of Mechanical Engineers*, vol. 201, pp. 145–152. ISSN 0263-7138.

Clements, W.W. and Artt, D.W. (1988 June). The influence of diffuser channel length-to-width ratio on the efficiency of a centrifugal compressor. *Proceedings of the Institution of Mechanical Engineers*, vol. 202, pp. 163–169. ISSN 0263-7138.

Cukurel, B., Lawless, P.B. and Fleeter, S. (2010). Particle Image Velocity Investigation of a High Speed Centrifugal Compressor Diffuser: Spanwise and Loading Variations. *Journal of Turbomachinery*, vol. 132, no. 2, p. 021010. ISSN 0889504X.

Cumpsty, N.A. (1989). *Compressor aerodynamics*. 1st edn. Longman Scientific & Technical.

Deniz, S., Greitzer, E.M. and Cumpsty, N.A. (2014). Effects of Inlet Flow Field Conditions on the Performance of Centrifugal Compressor Diffusers, Part 2: Straight-Channel Diffuser. vol. 122, no. January 2000.

Dixon, L.S. (2005). *Fluid Mechanics and Thermodynamics of Turbomachinery*. 1st edn. Butterworth-Heinemann.

Engeda, A. (2007). Effect of Impeller Exit Width Trimming on Compressor Performance.

Eum, H.-j., Kang, Y.-s. and Kang, S.-h. (2004). Tip Clearance Effect on Through-Flow and Performance of a Centrifugal Compressor. vol. 18, no. 6.

Filipenco, V.G., Deniz, S., Johnston, J.M., Greitzer, E.M. and Cumpsty, N.A. (2000). Effects of Inlet Flow Field Conditions on the Performance of Centrifugal Compressor Diffusers, Part 1: Discrete- Passage Diffuser. vol. 122, no. 1.

Inoue, M. and Cumpsty, N. (1984). Experimental Study of Centrifugal Impeller Discharge Flow in Vaneless and Vaned Diffusers. *Journal of Engineering for Gas Turbine and Power 106*.

Japikse, D. (1987). A Critical Evaluation of Three Centrifugal Compressors With Pedigree Data Sets: Part 5-Studies in Component Performance. *Turbomachinery*, vol. 109.

Kergourlay, G., Younsi, M., Bakir, F. and Rey, R. (2007). Influence of Splitter Blades on the Flow Field of a Centrifugal Pump: Test-Analysis Comparison. *International Journal of Rotating Machinery*, vol. 2007, pp. 1–13. ISSN 1023-621X.

Krige, D.S. (2013). *Performance Evaluation of a Micro Gas Turbine Centrifugal Compressor Diffuser by*. MEngr, Stellenbosch University.

Kritley, K.R. and Beach, T.A. (1992). Deterministic blade row interactions in a centrifugal compressor stage. *Journal of Turbomachinery*.

Kröger, D.G. (2008). Sunspot. Stellenbosch UNiversity Solar POwer Thermodynamic cyle principle.

Osborne, C. and Japikse, D. (1982). Comprehensive evaluation of a small centrifugal compressor.

Prinsloo, L. (2008). *The Commissioning of the Rover 1S / 60 Gas Turbine*. MSc, University of Pretoria.

Quarta, N.J. (2012). *Simulation of a Hybridised Solar Gas Turbine System*. Ph.D. thesis.

Rodgers, C. (1982). The performance of centrifugal compressor channel diffusers. , no. ASME Paer No. 82-GT-10.

Rover Gas Turbines Ltd (1965*a*). Operating manual. Rover 1S/60; Operating Manual of the Basic Engine.

Rover Gas Turbines Ltd (1965*b*). Overhaul manual. Rover 1S/60; Introduction.

Rover Gas Turbines Ltd (1965*c*). Overhaul manual. Rover 1S/60; Disassembly of the Basic Engine.

Saravanamuttoo, H.I.H., Rogers, G.F.C. and Cohen, H. (2001). *Gas Turbine Theory*. 5th edn. Pearson Education Limited.

SCHENCK Pegasus GmbH (1997). Eddy-Current Dynamometer technical documentation. Tech. Rep..

Shum, Y.K.P., Tan, C.S. and Clumpsty, N. (2000). Impeller-to-Diffuser Interaction in a Centrifugal Compressor. vol. 122, no. October 2000.

Ubaldi, M., Zunino, P. and Ghiglione, A. (1998). Detailed flow measurements within the impeller and the vaneless diffuser of a centrifugal turbomachine. *Experimental Thermal and Fluid Science*, vol. 17, pp. 147–155.

Yoshinaga, Y., Gyobu, I., Mishina, H., Koseki, F. and Hishida, N. (1980). Aerodynamic Performance of a Centrifugal Compressor With Vaned Diffusers. *ASME Journal of Fluids Engineering*, vol. 102.

Ziegler, K.U., Gallus, H.E. and Niehuis, R. (2003*a*). A Study on Impeller-Diffuser Interaction - Part I: Influence on the Performance. *Journal of Turbomachinery*, vol. 125, no. 1, p. 173. ISSN 0889504X.

Ziegler, K.U., Gallus, H.E. and Niehuis, R. (2003*b*). A Study on Impeller-Diffuser Interaction - Part II: Detailed Flow Analysis. *Journal of Turbomachinery*, vol. 125, no. 1, p. 183. ISSN 0889504X.

Appendices

A. Numerical Analysis

The 1-D and 3-D software package platforms are reviewed in detail in this Appendix.

A.1. Review of the 1-D software package

The software package that is used to perform the 1-D analyses is CompAero by Aungier (2000). CompAero implements the centrifugal compressor aerodynamic design and analysis strategy described in Aungier (2000), and axial flow turbine aerodynamic design and performance theory from Aungier (2003). The mean stream surface computations through all centrifugal compressor parts are executed by numerical methods supported by basic principles of fluid dynamics and thermodynamics.

The software package consists of various programs that each have their own specific function in the compressor design process, nonetheless only SIZE, CENCOM (***CEN***trifugal ***COM***pressor), and VDDESIGN (***V***aned ***D***iffuser ***DESIGN***) were beneficial to engineer a new centrifugal compressor design.

A.1.1. Overview of SIZE

The SIZE application is a centrifugal compressor stage preliminary aerodynamic design program. It implements the preliminary design procedure described in Chapter 6 of Aungier (2000). SIZE creates the input data files for the other centrifugal compressor aerodynamics programs of the CompAero software package. These input files are approximated, hence some editing may be necessary to achieve the appropriate values.

The specific rotation speed, impeller diameter, mass flow, head, efficiency and impeller tip flow angle are all required input data for the stage sizing calculations. Since some parameters are only used as design targets if the constraints of geometry permit, all input specifications can be edited iteratively to refine calculations and achieve the target performance.

A.1.2. Overview of CENCOM

The program CENCOM provides an aerodynamic performance analysis for a centrifugal compressor and plays a central role in the 1-D design process. The procedures used for the performance analysis are described in Chapter 5 of Aungier (2000). All geometry stages, i.e. the impeller, vaneless radial space and vaned diffuser are defined including the initial conditions of the flow. CENCOM collects performance predictions when a stage is analysed and uses them to provide performance maps for the centrifugal compressor design parameters such as: pressure, efficiency, and power.

A.1.2.1. Inlet flow and rotation speed input data

For a specific centrifugal compressor case the inlet flow, total pressure, total temperature, swirl and rotational speed are required parameters. Alternative options are available for three of the input parameters, namely, (Aungier, 2000):

- Inlet flow: mass flow rate, volume flow, or flow coefficient (ψ)
- Swirl parameter: on the mean streamline at the inlet either the absolute tangential velocity or absolute flow angle with respect to the tangent.
- Rotational speed: Rotations Per Minute (RPM), rotational Mach number (tip speed/inlet total sound speed), actual tip speed or equivalent tip speed.

In this thesis the three parameters used for the centrifugal compressor analysis were the mass flow rate ($\dot{m}$), the absolute tangential velocity (C_U), and the rotational speed (N). The operating range of the compressor at which the performance computations are executed by CompAero can be specified to a maximum number of 8 points.

A.1.2.2. Input data of the impeller geometry

The impeller geometry is related to the mean stream surface that divides the annulus into two equal areas, which is defined by the radius at the root-mean-square (rms) of the hub and shroud radii (Aungier, 2000). The blade angles are measured with respect to the tangential direction in the relevant stream surface. The impeller diameters for both the blade leading edge and trailing edge for the hub and shroud are required, as well as the passage widths relevant to the leading an trailing edges of the blade, the blade thicknesses, clearance gaps, throat area (A_{th}), and the cone angle (α_C) of the mean stream surface.

A.1.2.3. Vaneless radial passage input data

The conditions at the rms are also used for the input data of the vaneless passage. A minimum of three spaced stations of equal length along the passage are needed for the analysis. The flow path is generated by interpolation at each specific station using the required axial coordinate, radius and the passage width from hub-to-shroud.

A.1.2.4. Vaned diffuser input data

The thin-vaned or airfoil type vaned diffuser is applicable to the 1-D performance analysis of Aungier (2000). Nevertheless the author acquired reasonable results during occasional use for vane-island type diffusers, or thick vaned diffusers.

The required input data are shown in Figure 2.12, and include the radii of the leading edge and trailing edge (r_3, r_4), blade angles (β_3, β_4), passage inlet and outlet depths (b_3, b_4), and throat width (h_{th}). Additional data required include the number of vanes, the surface finish at the rms, the vane thickness at the leading and trailing edge, and the mean vane camberline angle at a mid-vane position.

A.1.2.5. Gas model

The ideal/non-deal gas flow models that are supported by CENCOM are listed below:

- Aungier's Modified Redlich-Kwong equation of state
- Original Reflich-Kwong equation of state
- Thermally perfect (ideal) gas equation of state
- Pdeugo-perfect gas equation of state

The thermally perfect, or ideal, gas equation of state was chosen as the thermodynamic model. Various gas properties are available in the ideal/non-ideal gas database of CENCOM for use in gas equations of state.

A.1.3. Overview of VDDESIGN

VDDESIGN is responsible for the aerodynamic design of conventional, thin or airfoil style vaned diffusers. The file from SIZE is used as a first input and is modified for most effective diffusion of the inlet aerodynamics of the finalized impeller design from CENCOM. The vane diffuser component sizing techniques, diffuser inlet, and vane design are iterative processes. The relative vane design geometry from VDDESIGN can be exported to CENCOM to execute the overall performance analysis of the compressor. The

impeller tip conditions are necessary to design a diffuser for the specific impeller configuration with VDDESIGN.

The required parameters are discussed in more detail in Chapter 3. However they will be briefly discussed to support the flow chart of the iterative design procedure followed in VDDESIGN shown in Figure A.1. The required parameters are: diffuser inlet radius (r_3), diffuser outlet radius (r_4), inlet blade angle (β_3), outlet blade angle (β_4), inlet passage depth (b_3), outlet passage depth (b_4), the number of diffuser vanes and the average vane surface finish.

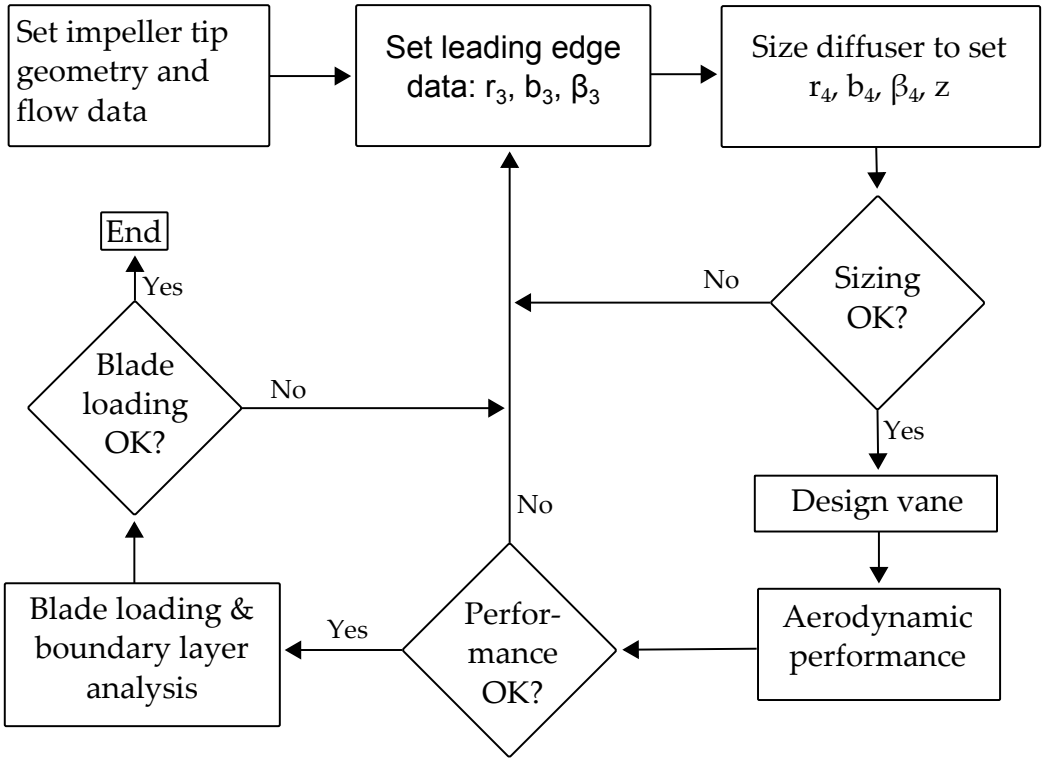

Figure A.1: Flow chart of the VDDESIGN design procedure

VDDESIGN allows to size all previously mentioned parameters according to one of the following sizing parameters:

- Divergence angle ($2\theta_C$)
- Area ratio (A_R)
- Discharge blade angle (β_4)

A.2. Review of the 3-D software package

ANSYS® v14.5 by ANSYS, Inc. is the CFD software platform used in this thesis. ANSYS® Workbench™ is the framework of the software package upon which the entire simulation process is tied together. The various software systems from the ANSYS® Workbench™ platform that are used for this thesis are described in this section.

A.2.1. Overview of ANSYS® Workbench

ANSYS® DesignModeler™ is a parametric feature-based solid modeller for 3-D modelling, or importing 3-D CAD models for CFD analysis preprocessing. Although Autodesk® software is used to generate the bodies that represent the flow-path of the standard compressor, the DesignModeler™ is still used to import the solid bodies in the Workbench™ environment.

The ANSYS® Meshing application is the general component of the Workbench™ to create meshes. It combines offerings from other ANSYS® meshing programs, such as ICEM CFD™ and TurboGrid™, and can be used for different solvers.

ANSYS® BladeGen™ is used to create bladed components by only modelling a single blade row. BladeGen™ provides an import wizard where the outline of the blade profile and meridional plane can be defined by supplied curve files. Following this, BladeGen™ converts the splines into a blade profile and meridional plane where the blade design can be either modified or evaluated. The design data can automatically be converted into a CAD file using BladeEditor™.

ANSYS® TurboGrid™ software is a highly automated hexahedral mesh generator specifically for turbomachinery. A structure of blocks, known as a topology, acts as a framework for positioning the mesh elements. The topology is invariant from hub-to-shroud and is edited on 2-D layers which are located at various spanwise locations. The surface mesh is visible on the topology, as the topology is adjusted the actual mesh is also changed showing the true effect of the topology changes. Visualization of the mesh statistics on the layers helps to identify the problem areas before generating the full 3-D mesh.

ANSYS® CFX® is a general purpose CFD software package that combines a solver with a pre- and post-processing ability. The CFX®-Pre program is where the CFD simulation is defined. The physics setup can be done in either general mode, or turbomachinery mode which simplifies the setup

for rotating machinery. CFX®-Solver involves creating a flow field including respective turbulence models and appropriate boundary conditions by solving a group of discretized equations for both steady and unsteady flow models. CFX®-Post is used as a tool to obtain quantitative and/or qualitative information about the fluid flow performance, and perform a flow field visualization.

The least number of blades or vanes required to represent the impeller and diffuser respectively can be selected to reduce the computational time, and consequently overcome the large limitation on CFD simulations with a fine mesh. The required rotational periodicity is configured in CFX®-Pre to simulate the complete compressor mesh.

A.2.2. Mesh quality and convergence

Several mesh metric represent the quality of the mesh and are checked after every mesh generation. Following this the mesh was adjusted when necessary to comply with the mesh quality criteria and improve the overall mesh quality. The mesh metric include:

- Orthogonal quality; orthogonality is the angle between the vector that joins two nodes and the normal vector for the surface integration point associated with that edge. Mesh orthogonal quality has a value between 0 and 1 and relates to how close these angles are to some optimal angle.
- Aspect ratio; the degree that mesh elements are stretched, i.e. the length of a cell divided by its width.
- Mesh expansion factor; the rate of change in the magnitude of adjacent element face areas or volumes.
- Skewness; determines how close to ideal a face or a cell is. Equilateral shapes are indicated by a value of 0 and degenerate cells are indicated by a value of 1.
- Minimum/maximum face angle; the same principle as skewness but with angle criteria.

For this thesis the mesh metric criteria were: an orthogonality quality greater than 25°, an aspect ratio smaller than 1000, a mesh expansion smaller than 2.5, and a skewness factor smaller than 0.9 or a minimum and maximum face angle of 15° and 165° respectively. The mesh quality values for both centrifugal compressors are exhibited in their specific section in Chapter 4.

The initial simulations were executed on a coarse mesh to allow for rapid convergence. Following this the converged solution was used to initialize the finer mesh.

B. CompAero Performance Analysis Theory

A summary of the theory behind the one-dimensional calculations on the mean stream surface with the software package CompAero is discussed in this Appendix. For a comprehensive explanation please refer to Chapter 4 and 5 in Aungier (2000).

B.1. Impeller work input coefficient prediction

The impeller analysis is conducted in the rotating frame of reference and firstly the work coefficients are determined. It is convenient to use a dimensionless form to express the impeller work. The total work input coefficient of the impeller is defined as:

$$I = \Delta h_t / U_2^2 = I_B + I_{DF} + I_L + I_R \tag{B.1.1}$$

B.1.1. blade work

The blade work input coefficient follows from the basic conservation of energy and power input, resulting in:

$$I_B = \sigma \left(1 - \lambda C_{m,2} \cot \beta_2 / U_2\right) \tag{B.1.2}$$

where σ is called the slip factor and λ represents the tip distortion.

B.1.1.1. The slip factor

The Busemann slip factor at zero flow results in the experimental expression in Equation B.1.3. Consequently the slip factor can be treated as a constant up to a limiting radius ratio ϵLIM. Following this Aungier *et al.* (1993) introduced a correction procedure for an accurate approximation to Busemann's results for larger values of ϵ (Equation B.1.4)

$$\sigma = 1 - \frac{\sqrt{\sin \beta_2}\, \sin \alpha_{C2}}{z^{0.7}} \tag{B.1.3}$$

$$\epsilon_{LIM} = \frac{\sigma - \sigma\star}{1 - \sigma\star}\sigma\star = \sin(19^0 + 0.2\beta_2) \tag{B.1.4}$$

Ultimately a corrected slip factor, σ_{COR}, is introduced for $\epsilon > \epsilon_{LIM}$:

$$\sigma_{COR} = \sigma\left[1 - \left(\frac{\epsilon - \epsilon_{LIM}}{1 - \epsilon_{LIM}}\right)^{\sqrt{\frac{\beta_2}{10}}}\right] \tag{B.1.5}$$

Special procedures are required to estimate the slip factor when splitter blades are employed for high Mach number impellers. Since splitter blades do not have the same meridional length (L) as full blades Aungier (2000) recommends the use of an effective number of blades, i.e.

$$z = z_{FB} + Z_{SB}L_{SB}/L_{FB} \tag{B.1.6}$$

B.1.1.2. The impeller distortion factor

The impeller distortion factor λ, also known as tip blockage, B_2, is an important parameter to determine the impeller work. Aungier *et al.* (1993) formulated an empirical tip blockage model defined as:

$$B_2 = \bar{\omega}_{SF}\frac{p_{v1}}{p_{v2}}\sqrt{\frac{W_1 d_H}{W_2 b_2}} + \left[0.3 + \frac{b_2^2}{L_B^2}\right]\frac{A_R^2\rho_2 b_2}{\rho_1 L_B} + \frac{\delta_{CL}}{2b_2} \tag{B.1.7}$$

where the velocity pressure = $p_v = p_t - p$ and a passage area ratio is defined in Equation B.1.8. The left hand side of the equation contains the term $\bar{\omega}_{SF}$ which represents the skin friction loss (Equation B.1.9).

$$A_R = \frac{A_2 \sin\beta_2}{A_1 \sin\beta_{th}} \tag{B.1.8}$$

$$\begin{aligned} \bar{\omega}_{SF} &= 4c_f\left(\bar{W}/W_1\right)^2 L_B/d_H \\ \bar{W}^2 &= \left(W_1^2 + W_2^2\right)/2 \\ \bar{W}^2 &\geq \left(W_{th}^2 + W_2^2\right)/2 \end{aligned} \tag{B.1.9}$$

The hydraulic diameter (d_H) represents the average of the throat and tip values, whereby the tip area is normal to the direction of the flow, i.e., $A_2 \sin\beta_2$. The last term in Equation B.1.7 applies to the tip clearance assuming that half of the total area is available for through-flow.

B.1.2. Clearance gap flows

The exploitative of the impeller work output by windage and disk friction, leakage, and recirculation is dependant upon flow disturbances in the clearance gaps. The governing equation of the gap flows is defined as

$$\frac{\delta p}{\delta r} = K^2 \omega^2 \rho r \tag{B.1.10}$$

where the clearance gap swirl parameter (K = $C_U/\omega r$) is assumed constant. The pressure difference over the blade is the main reason for flow leakage; the velocity is estimated by

$$U_{CL} = 0.816\sqrt{2\Delta p_{CL}/\rho_2} \tag{B.1.11}$$

where the throttling coefficient 0.816 is calculated by assuming abrupt contraction and expansion losses as the flow moves through the clearance gap, and the flow density at the tip is considered constant (Aungier *et al.*, 1993). Because the pressure difference across the blade surfaces must be equal to the torque of the impeller that is defined by the conservation of angular momentum, the following expression can be used to calculate the pressure difference across the gap:

$$\begin{aligned} \Delta p_{CL} &= \frac{\dot{m}\left(r_2 C_{U2} - r_1 C_{U1}\right)}{z\bar{r}\bar{b}L} \\ \bar{r} &= \left(r_1 + r_2\right)/2 \\ \bar{b} &= \left(b_1 + b_2\right)/2 \end{aligned} \tag{B.1.12}$$

Now the leakage flow through the blade clearance gap is estimated by

$$\dot{m}_{CL} = \rho_2 z s L U_{CL} \tag{B.1.13}$$

B.1.3. Windage and disk friction work

Aungier (2000) uses a disk torque coefficient model for centrifugal compressors from Daily and Nece which is empirically corrected:

$$C_M = C_{M0}\left(1 - K\right) 2/\left(1 - K_0\right)^2 \tag{B.1.14}$$

where C_{M0} represents the Daily and Nece torque coefficient. The disk and cover of the impeller are treated independently to calculate the disk friction and corrected by:

$$C_{MD} = 0.75 C_M C_{MC} = 0.75 L C_M \left[1 - \left(d_{1s}/d_2\right)^5\right]\left(r_2 - r_1\right) \tag{B.1.15}$$

where factor 0.75 is developed from experimental predictions and correlation studies. The work loss coefficient of the impeller due to windage and disk friction then yields:

$$I_{DF} = \left(C_{MD} + C_{MC}\right)\rho_2 U_2 r_2^2/\left(2\dot{m}\right) \tag{B.1.16}$$

B.1.4. Leakage work

The seal leakage can be computed when the pressure ratio across the seal is known. First the leakage mass flow is defined as:

$$\dot{m}_L = \pi d \delta C_t C_c C_r \rho \sqrt{RT} \tag{B.1.17}$$

where the seal carryover (C_c), the seal throttling (C_t) and the contraction ratio (C_r) are empirical seal coefficients; ρ and T are upstream values. Aungier *et al.* (1993) assumes that, for open impellers, half of the blade clearance leakage is re-energized by the impeller because of blade passage flow re-entry; expressed as

$$I_L = \dot{m}_{CL} U_{CL} / \left(2 U_2 \dot{m}\right) \tag{B.1.18}$$

where $\dot{m}_{CL}$ represents half of the leakage flow ($\dot{m}_L$)

B.1.5. Recirculation work

High head coefficient impellers that experience heavy blade loading and have low relative flow angles at the impeller tip often develop backflow. As a result an obvious increase in work is shown associated with recirculation work. Therefore the blade velocity difference is determined assuming ideal blade loading (Equation B.1.19). Furthermore the blade loading is evaluated by defining the equivalent diffusion factor to estimate the pronounced influence of the recirculation flow (Equation B.1.20).

$$\Delta W = 2\pi d_2 U_2 I_B / \left(z L_B\right) \tag{B.1.19}$$

$$\begin{aligned} W_{max} &= (W_1 + W_2 + \Delta W)/2 \\ D_{eq} &= W_{max}/W_2 \end{aligned} \tag{B.1.20}$$

When $D_{eq} > 2$ blade stall can be expected, hence a recirculation flow work input coefficient is defined as:

$$\begin{aligned} I_R &= (D_{eq}/2 - 1)\left[W_{U2}/C_{m2} - 2\cot\beta_2\right] \\ I_R &\geq 0 \end{aligned} \tag{B.1.21}$$

Only specific types of tip velocity triangles are prone to recirculation loss, therefore the recirculation work input coefficient is mostly equal to naught.

B.2. Impeller analysis loss coefficients

The impeller analysis uses loss models of Aungier *et al.* (1993) and are expressed in total pressure loss. All calculations are conducted in the rotating

frame of reference. The following models are used by Aungier (2000) in the impeller performance analysis to calculate various loss coefficients:

The incidence angle computations are applied at the hub, mean-line and shroud stream surfaces. The mean-line calculations weigh 10 times heavier than the hub and shroud stream surfaces. The first term of Equation B.2.1 represents the overall inlet shock and incidence loss coefficients, and the second term accounts for the effect of the abrupt flow area contraction at the blade leading edge; the usual blade thickness makes this term mostly negligible.

$$\bar{\omega}_{inc} = 0.8\left[1 - C_{m1}/\left(W_1 \sin\beta_1\right)\right]^2 + \left[z_{FB} t_{b1}/\left(2\pi r_1 \sin\beta_1\right)\right]^2 \tag{B.2.1}$$

where the first term can be recognized as 80% of a total abruption expansion loss. An additional diffusion loss that occurs at the entrance of some impellers which have a more significant flow diffusion between the leading edge of the blade and the throat area is defined as:

$$\bar{\omega}_{DIF} = 0.8\left[1 - W_{th}/W_1\right]^2 - \bar{\omega}_{inc}; \qquad \bar{\omega}_{DIF} \geq 0 \tag{B.2.2}$$

The choke losses are computed by assigning a sonic velocity area (Equation B.2.3) combined with a contracted throat area that models the aerodynamic blockage (Equation B.2.4).

$$A^\star = \dot{m}/\left(\rho^\star C^\star\right) \tag{B.2.3}$$

$$\begin{aligned} X &= 11 - 10 C_r A_{th}/A^\star \\ \bar{\omega}_{CH} &= 0; \qquad X \leq 0 \\ \bar{\omega}_{CH} &= tfrac12\left(0.05X + X^7\right); \qquad X > 0 \end{aligned} \tag{B.2.4}$$

The blade skin friction losses are also accounted for in the loss model (Equation B.1.9), and the blade loading loss coefficient is defined as:

$$\bar{\omega}_{BL} = \left(\Delta W/W_1\right)^2/24 \tag{B.2.5}$$

The blade loading loss coefficient model relates to the pressure gradient from blade-to-blade. It is expected that the blade loss coefficient will have a serious effect on the occurrence of flow separation when these gradients become larger than the velocity head. In addition the hub-to-shroud load loss has an identical effect on the flow separation (Equation B.2.6).

$$\begin{aligned} \bar{\omega}_{HS} &= \left(\bar{\kappa}_m b \bar{W}/W_1^2\right)/6 \\ \bar{\kappa}^m &= \left(\alpha_{C2} - \alpha_{C1}\right)/L \end{aligned} \tag{B.2.6}$$

The impeller tip mean stream surface distortion factor (Equation B.1.7) is also believed to contribute a loss and is defined as:

$$\bar{\omega}_{\lambda} = \left[(\lambda - 1)\, C_{m2}/W_1\right]^2 \tag{B.2.7}$$

Blade wake mixing is also expected to contribute to the impeller losses. The severity of the wake is approximated with the equivalent diffusion factor (Equation B.1.20) to estimate the separation velocity:

$$\begin{aligned} W_{SEP} &= W_2; \qquad D_{eq} \geq 2 \\ W_{SEP} &= W_2 D_{eq}/2 : \qquad D_{eq} > 2 \end{aligned} \tag{B.2.8}$$

Since the tangential velocity of the wake mix is controlled by conservation of momentum only the meridional velocity component before and after the wake mixing is approximated from W_{SEP}, that is:

$$C_{m,wake} = \sqrt{W_{SEP}^2 - W_U^2}\, C_{m,mix} = C_{m2} A_2 / \left(\pi d_2 b_2\right) \tag{B.2.9}$$

which supports the definition for the wake mixing loss coefficient:

$$\bar{\omega}_{CL} = 2\dot{m}_{CL} \Delta p_{CL} / \left(\dot{m} \rho_1 W_1^2\right) \tag{B.2.10}$$

The critical Mach number also contributes to the losses when shocks form due to supersonic speeds on the suction side of the blade; boundary layer separation is also expected. The critical Mach number loss coefficient is therefore estimated from

$$\bar{\omega}_{CR} = 0.4 \left[(Ma_1' - Ma_{CR}')\, W_{max}/W_1\right]^2 \tag{B.2.11}$$

B.3. Vaneless radial passage

The vaneless radial passage analysis acquires the total thermodynamic flow input values at the leading edge of the diffuser from the upstream impeller state. Equation B.3.1 through Equation B.3.4 form a conventional set of equations for one-dimensional performance analyses and are therefore used in CENCOM along the passage length of the vaneless radial diffuser. The one-dimensional analysis for the vaneless radial passage properties is, as is the case with the impeller analysis, refined with experimental data comparison. The governing equations are indicated below (Aungier, 2000).

$$2\pi r \rho b C_m \left(1 - B\right) = \dot{m} \tag{B.3.1}$$

$$b C_m \frac{d\left(r C_U\right)}{dm} = -r C C_U c_f \tag{B.3.2}$$

$$\frac{1}{\rho}\frac{dp}{dm} = \frac{C_U^2 \sin\alpha_C}{r} - C_m \frac{dC_m}{dm} - \frac{C C_m c_f}{b} - \frac{dI_D}{dm} - I_C \tag{B.3.3}$$

$$h_t = h + \tfrac{1}{2}C^2 \tag{B.3.4}$$

The supplementary terms I_D and I_C in Equation B.3.3 address loss because of flow diffusion and passage curvature respectively. The flow diffusion losses are subjected to additional relations and modelled with a classic diffuser analogy presented in Chapter 5 of Aungier (2000). So is a diffuser analogy used at each computing station to estimate the maximum, stall-free, local area by

$$(rb)_m = (eb)_1 \left[1 + 0.16m/b_1\right] \tag{B.3.5}$$

which is equivalent to a diffuser divergence angle, $2\theta_C = 9°$. The area blockage factor and skin friction coefficient are calculated with the use of a simple boundary layer model based on a $1/7^{\text{th}}$ power law for the velocity profiles.

$$C_m = C_{me}\left(\lambda/\delta\right)^{1/7} \tag{B.3.6}$$

$$C_U = C_{Ue}\left(\lambda/\delta\right)^{1/7} \tag{B.3.7}$$

where subscript e appoints a value at the boundary layer edge. If the two boundary layers are uniform and the boundary layer thickness (δ) is known, an expression for the area blockage (B) as a function of 2δ/b can be obtained by integrating across the mass flow passage (Equation B.3.8).

$$\begin{gathered}\int_0^b \rho C_m dy = \rho b C_{me}\left[1 - 2\delta/\left(8b\right)\right] = \rho b C_{me}\left(1 - B\right) \\ B = \frac{2\delta}{8b}\end{gathered} \tag{B.3.8}$$

In a like manner integrating for the angular momentum flux yields Equation B.3.9. Now the average angular momentum can be related to the boundary layer edge meridional velocity (Equation B.3.8).

$$\int_0^b r\rho C_m C_U dy = r\rho C_{me} C_{Ue}\left[1 - 2\delta/\left(4.5b\right)\right] \tag{B.3.9}$$

Thus C_{Ue} can be defined using rC_U at the inlet if δ is known. Following this the local predicted rC_U and the known rC_{Ue} are used along the passage to determine the local boundary layer thickness and area blockage.

B.4. Vaned diffuser

In CENCOM the thermodynamic conditions for the vaned diffuser are acquired from the upstream components. Evidently the discharge state values of the vaneless radial passage are used for the inlet conditions of the vaned diffuser.

B.4.1. Diffuser choke

The viscous area blockage in the vane throat parallel to the impeller is defined as a throat contraction ratio. If the effective throat area ($C_r A_{th}$) is equal to the sonic flow area (Equation B.2.3) choke will occur.

$$C_r = \sqrt{\frac{A_3 \sin \beta 3}{A_{th}}} \tag{B.4.1}$$

B.4.2. Diffuser stall

Vaned diffuser stall is analysed with an average value employed between the inlet and the throat, defined by

$$K = \frac{r_3}{h_{th}} \left[\frac{\cos \alpha_3}{\cos \alpha_{th}} - 1 \right] \alpha_{th} = A_{th}/A_3 \tag{B.4.2}$$

The Mach number effect on the onset of vaned diffuser stall is significant, consequently the following expression for K_0 is given

$$K_0 = \frac{M_3^2 \sin^2 \beta_3 \cos \beta_3}{1 - M_3^2 \sin^2 \beta_3} \tag{B.4.3}$$

which assumes a constant width and a flow angle equal to the vane inlet angle. Aungier (2000) provides an empirical criterion that estimates stall in vaned diffusers:

$$K + K_0 = 0.39 \tag{B.4.4}$$

B.4.3. Diffuser analysis loss coefficients

The loss models used for the diffuser are similar to the impeller loss coefficients (Section B.2), however the absolute velocity reference is used. For example the skin friction coefficient in Equation B.4.5 is identical to impeller Equation B.1.9, with exception of the term $2\delta/d_H$ which corrects for the fully-developed flow profile usually not present in a diffuser.

$$\bar{\omega}_{SF} = 4 c_f \left(\bar{C}/C_3 \right)^2 L_B/d_H/ \left(2\delta/d_H \right)^{0.25} \tag{B.4.5}$$

The optimum or minimum-loss incidence angle is given as

$$\sin \alpha_3^\star = \frac{C_{m3}}{C_3^\star} = \sqrt{\sin \beta_3 \sin \alpha_{th}} \tag{B.4.6}$$

Following this optimum incidence angle the minimum incidence angle loss can be determined (Equation B.4.7)

$$\bar{w}_{i0} = 0.8 \left[\left(C_3^\star - C_{th} \right) / C_3 \right]^2 + \left[z t_{b3} / \left(2\pi r_3 \right) \right]^2 \tag{B.4.7}$$

The blockage loss coefficient model is adjusted to allow the use of thick vanes and different hub-to-shroud widths; the diffuser divergence angle (Equation B.4.8) and the blade loading parameter are employed (Equation B.4.9).

$$2\theta_C = 2\tan^{-1}\left\{\left[\left(w_4 - t_{b4}\right)b_4/b_3 - w_3 + t_{b3}\right]/\left(2L_B\right)\right\} \tag{B.4.8}$$

where $w = \left(2\pi r \sin\beta\right)/z$.

$$L = \Delta C/\left(C_3 - C_4\right)\Delta C = 2\pi\frac{r_3 C_{U3} - r_4 C_{U4}}{zL_B} \tag{B.4.9}$$

The passage area ratio of the diffuser used in the discharge sizing process is given by:

$$A_R = \frac{r_4 \sin\beta_4}{r_3 \sin\beta_3} \tag{B.4.10}$$

The discharge area blockage and contributing variables such as the swirl parameter (K) and absolute meridional recirculating velocity are defined in Equation B.4.11. As with the impeller only the meridional velocity is used in the wake mixing process.

$$\begin{aligned} B_4 = \left[K_1 + K_2\left(\bar{C}_R^2 - 1\right)\right]L_B/w_4\bar{C}_R &= \frac{1}{2}\left[\frac{C_{m3}\sin\beta_4}{C_{m4}\sin\beta_3} + 1\right] \\ K_1 &= 0.2\left[1 - 1/\left(C_L C_\theta\right)\right] \\ K_2 &= \frac{2\theta_C}{125C_\theta}\left[1 - \frac{2\theta_C}{22C_\theta}\right] \end{aligned} \tag{B.4.11}$$

The total pressure at the diffuser discharge is defined as:

$$p_{t,4} = p_{t,3} - \left(p_{t,3} - p_3\right)\sum_i \bar{\omega}_i \tag{B.4.12}$$

where the total pressure loss coefficient is represented by $\bar{\omega}_i$

C. Axial Flow Turbine Stage Efficiency Model

The turbine stage efficiency model from Saravanamuttoo *et al.* (2001) was used to calculate the isentropic efficiency of the axial flow turbine stage. This isentropic efficiency model uses the geometry dimensions and blade design properties (Table C.1) to determine the velocity triangles of the axial flow turbine stage. Following this the flow angles can be used to estimate the various losses that have an effect on the overall performance of the turbine.

Table C.1: Turbine geometry

Geometry parameters	Stator	Rotor
Mean distance between blades [m]	0.0076	0.0050
Mean blade pitch [m]	0.0246	0.0173
Trailing edge thickness [m]	0.0008	0.0008
Mean blade height [m]	0.0124	0.0155
Chord [m]	0.0410	0.0236
Tip clearance [m]	0	0.0005
Trailing edge thickness/Chord ratio [t/c]	0.0195	0.0339
Pitch/Chord ratio [s/c]	0.6000	0.7331
Trailing edge thickness/Pitch ratio [t/s]	0.0325	0.0462

All assumptions, formulae, and figures in this Appendix originate from Saravanamuttoo *et al.* (2001).The suggested constant values for the specific heat and the specific heat ratio of the air flow are:

C_p = 1,148 kJ/kg·K $\qquad\qquad$ γ = 1.333

The axial flow turbine stage is divided into three different planes located at the: stator inlet, stator exit/rotor inlet and rotor exit. The numeral subscripts used in the equations each refer to a specific plane (Figure C.1).

C.1. Step 1: profile loss coefficient estimation

First the inlet flow angle of the stator and the rotor was determined. The inlet flow angle of the stator blade is assumed axial $\alpha_1 = 0$ and therefore the absolute velocity $C_1 = C_{a1}$. The rotor flow angle was found to be $\beta_2 = 14.8°$.

The blade tip speed (U) is a function of the rotor radius, therefore the shape of the velocity triangles varies from root to tip. Because of the low tip to root radius ratio the conditions at the mean of the annulus were used to assume the effects on the mass flow as it passes through the stage. The velocity triangles in Figure C.1 were used to determine the inlet and exit velocities in the different sections of the turbine.

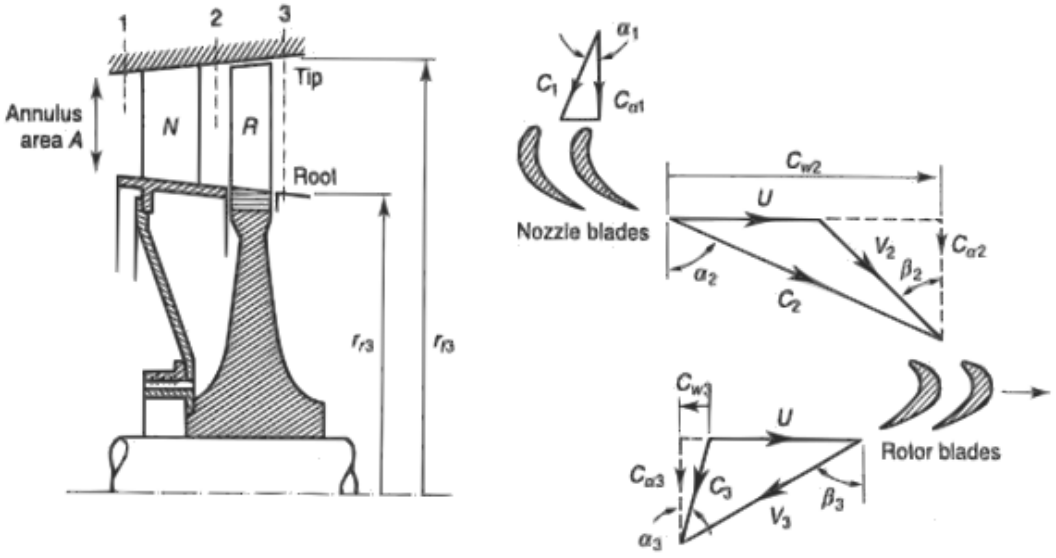

Figure C.1: Turbine planes and velocity triangles (Saravanamuttoo *et al.*, 2001)

The exit velocities of the stator vanes and rotor blades were estimated $V_2 = 143.4$ m/s and $V_3 = 493.4$ m/s respectively. Subsequently the cosine rule was used to calculate the outlet blade angle of the stator and rotor.

Stator: $\cos^{-1}\left(\frac{o}{s}\right) = 72°$ Rotor: $\cos^{-1}\left(\frac{o}{s}\right) = 73.2°$

Then the rotor inlet flow angle (α_2) and rotor exit flow angle (β_3) were determined by using linear interpolation on the curve in Figure C.2.

Stator: $\alpha_2 = 72.56°$ Rotor: $\beta_3 = 73.69°$

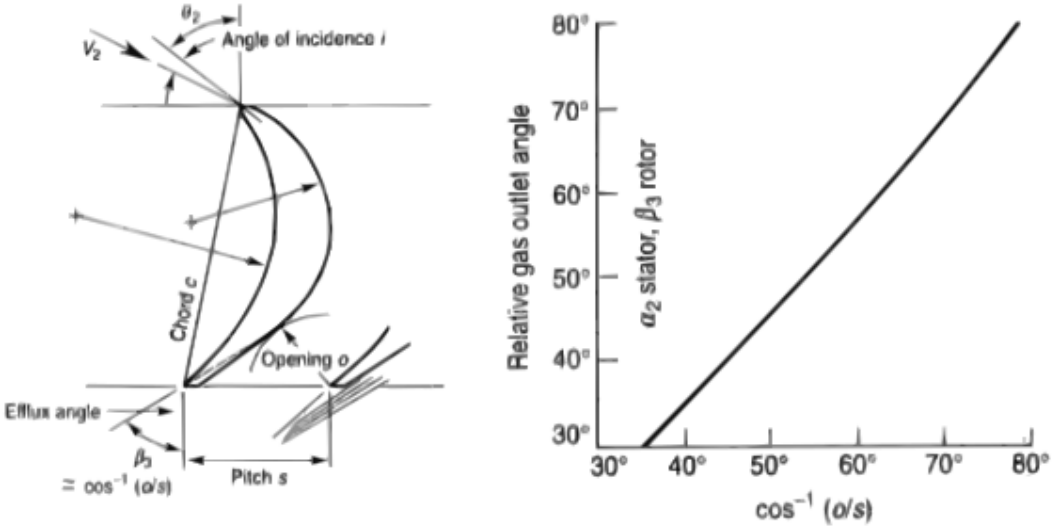

Figure C.2: Gas outlet angles (Saravanamuttoo *et al.*, 2001)

Following this all other relevant flow angles and velocities were estimated (Table C.2).

Table C.2: Velocity values and flow angles of the three turbine stages

Velocities [m/s]		Inlet and exit gas angles [°]	
Mean rotational speed (U)	403.43	Swirl angle jet pipe (α_3)	26.85
Inlet velocity ($C_{a1}/C_1/C_3$)	243.55	Relative outlet angle (β_3)	73.69
Outlet velocity (C_2)	439.71	Degree of reaction	0.54
Axial Inlet velocity (C_a)	146.95	Inlet gas angle (β_2)	14.9
Axial outlet velocity (C_{a2}/C_{a3})	138.58	Relative outlet angle (α_2)	71.63
Velocity at stage 2 (V_2)	143.39	Mean stator angle (α_m)	56.41
Velocity at stage 3 (V_3)	493.44	Mean rotor angle (β_m)	57.6

C.2. Step 2: estimating the overall loss coefficient

The overall blade loss coefficient (Υ) consists of profile loss, annulus loss, secondary flow loss and tip clearance loss. Thus Υ incorporates the two-dimensional profile loss and three-dimensional losses that were conveniently treated simultaneously.

The profile loss coefficient Υ_p was found by using the inlet and exit flow angles of the stator (a) and rotor (b) in Figure C.3.

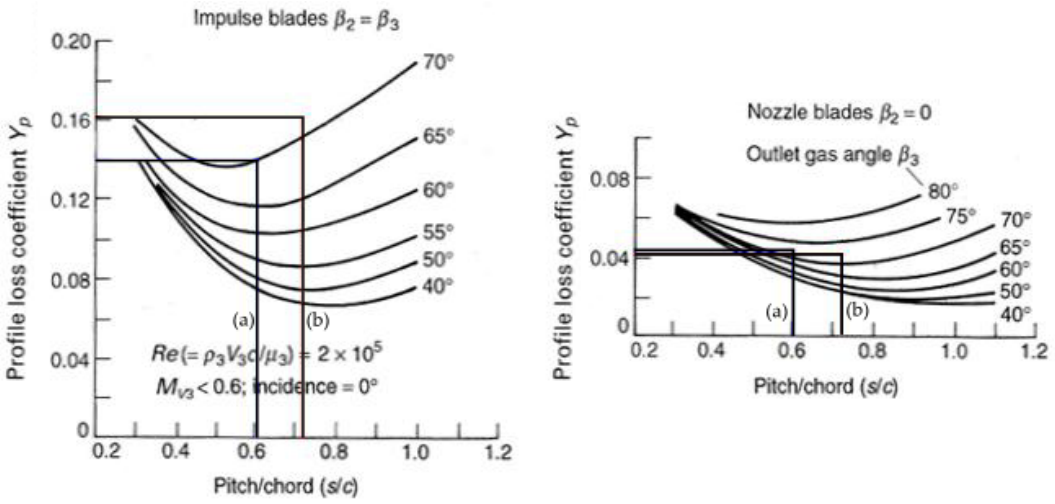

Figure C.3: Profile loss coefficient curve (Saravanamuttoo *et al.*, 2001)

After which the overall blade profile loss coefficient of the stator and rotor blades were determined by using:

$$(\Upsilon_p)_S = \left\{ \Upsilon_{p(\alpha_1=0)} + \left(\frac{\alpha_1}{\alpha_2}\right)^2 [\Upsilon_{p(\alpha_1=\alpha_2)} - \Upsilon_{p(\alpha_1=0)}] \right\} \left(\frac{t/c}{0.2}\right)^{\alpha_1/\alpha_2} \tag{C.2.1}$$

$$(\Upsilon_p)_R = \left\{ \Upsilon_{p(\beta_2=0)} + \left(\frac{\beta_2}{\beta_3}\right)^2 [\Upsilon_{p(\beta_2=\beta_3)} - \Upsilon_{p(\beta_2=0)}] \right\} \left(\frac{t/c}{0.2}\right)^{\beta_2/\beta_3} \tag{C.2.2}$$

$(\Upsilon_p)_S = 0.042$ $\qquad$ $(\Upsilon_p)_S = 0.032$

As the example above indicates, the equations regarding losses are identical for the stator and the rotor. Therefore only the equations for the rotor will be displayed from here onwards.

Annulus loss and secondary flow loss cannot easily be separated, thus they are accounted for by a secondary loss coefficient (Υ_s). In addition the tip clearance loss coefficient is denoted by (Υ_k). As has been noted these three dimensional friction losses are treated simultaneously:

$$\Upsilon_s + \Upsilon_k = \left[\lambda + B\left(\frac{k}{h}\right)\right] \left[\frac{C_L}{s/c}^2\right] \left[\frac{\cos^2 \beta_3}{\cos^3 \beta_m}\right] \tag{C.2.3}$$

The lift coefficient of the stator and rotor blades were estimated using

$$C_L = 2(s/c)(\tan \beta_2 + \tan \beta_3) \cos \beta_m \tag{C.2.4}$$

Furthermore, to calculate the secondary loss component (λ) the function curve in Figure C.4 was used in combination with the following equation:

$$\lambda = f\left\{\left(\frac{A_3 \cos\beta_3}{A_2 \cos\beta_2}\right)^2 \Big/ \left(1 + \frac{r_r}{r_t}\right)\right\} \tag{C.2.5}$$

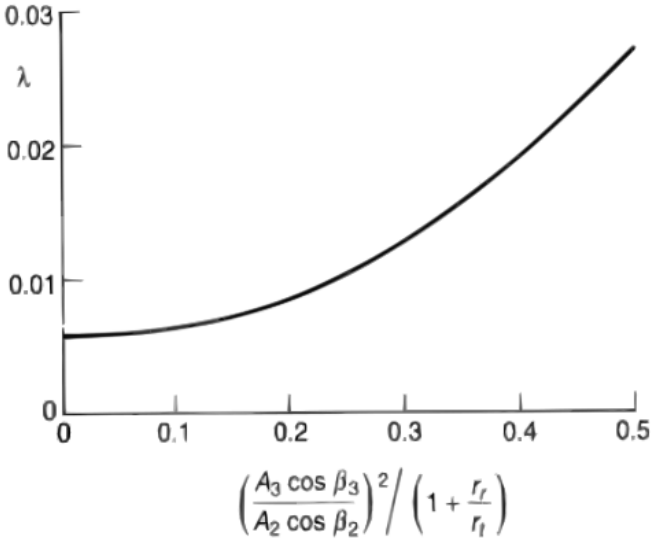

Figure C.4: Lambda function curve (Saravanamuttoo *et al.*, 2001)

When finally the secondary and tip clearance losses for the stator and rotor blades were determined

Stator: $\Upsilon_s + \Upsilon_k = 0.039$ Rotor: $\Upsilon_s + \Upsilon_k = 0.228$

C.3. Step 3: estimate the total loss coefficient

The total loss coefficient was calculated by adding the total profile loss coefficient and the secondary and tip clearance losses

$$\Upsilon_R = \left[(\Upsilon_P)_R + (\Upsilon_s + \Upsilon_k)_R\right] cf \tag{C.3.1}$$

A correction factor was required since the thickness/blade pitch ratio of the trailing edge is different from 0.02 (Figure C.5). Including the correction factor the total loss coefficient of the stator and rotor blades were found to be:

Stator: $\Upsilon_S = 0.088$ Rotor: $\Upsilon_R = 0.306$

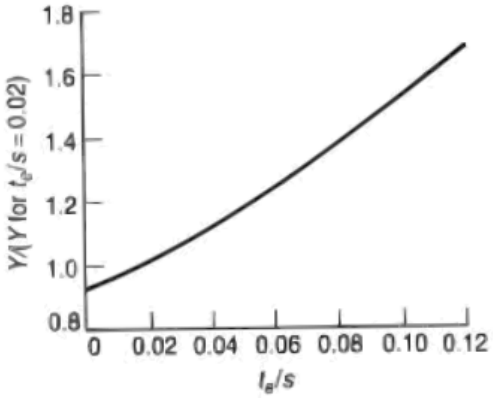

Figure C.5: Trailing edge thickness correction factor (Saravanamuttoo *et al.*, 2001)

C.4. Step 4: stage efficiency

The efficiency of the axial flow turbine can now be calculated using:

$$\eta_t = \frac{1}{\left\{1 + \left[\left(\lambda_R \left(\frac{V_3^2}{2C_p}\right)\right) + \left(\frac{T_3}{T_{02}}\right)\lambda_S \left(\frac{V_2^2}{2C_p}\right)\right] / (T_{01} - T_{03})\right\}} \tag{C.4.1}$$

where the temperature equivalent loss coefficients λ_S and λ_R are defined as

$$\lambda_S = \frac{\Upsilon_S}{T_{02}/T_2'} \qquad \lambda_R = \frac{\Upsilon_R}{T_{03}/T_3''}$$

The temperature values at the different stages of the axial flow turbine were determined (Table C.3). After that the total loss coefficient was estimated

Stator: λ_S = 0.0805 Rotor: λ_R = 0.2914

This results in an *85.4%* stage efficiency of the axial flow turbine.

Table C.3: Temperatures values of the three turbine stages

Turbine stage temperatures [K]	
Inlet stagnation temperature (T_{01} = T_{02})	1032
Stagnation temperature drop (ΔT_{0s})	190.21
Outlet stagnation temperature (T_{03})	841.79
Outlet temperature (T_3)	833.15
Temp equivalent outlet velocity (T_{02} - T_2)	87.03
Stage 2 temperature (T_2)	944.97
Stage 2 temp after isentropic expansion (T_2')	940.62
Isentropic expansion rotor blades (T_3'')	800.82

D. Experimental Setup

The experimental testing software, experimental procedure and measuring equipment calibration are discussed in this Appendix.

D.1. Testing software

Engine test automation (ETA) is the interface used for supervisory control and data acquisition. With ETA all instrumental data can be monitored (temperature, pressure, mass flow, speed, and torque), the solenoids in the fuel line can be regulated, the starter motor and the spark plug are controlled, alarms and emergency shut-downs can be programmed, measuring instrumentation can be calibrated and experimental data can be logged.
ETA communicates with the PLC in raw registry values between 0 and 32767 to exchange data, using the RsLogix software package to program the PLC and the Allen Bradley driver to interlink the ETA user interface and the PLC. A measuring instrumentation output signal of 4-20 mA will correspond to a 3277 register value for 4 mA, and a 16384 register value corresponds to 20 mA.

The registry values can be used to calibrate the analogue input and output channels of the PLC in ETA. The calibration screens capture the registry value and the measured value assigned to that registry value. In order to use the regression functions in ETA; numerous values are captured across the measuring range of the channel.

Because of the large quantity of measuring data available on the user interface, it can be difficult to observe every parameter during testing. To overcome this ETA supports the option to program alarms. Therefore alarms were set on the important channels such as speed, EGT, and oil pressure. If one of the parameters exceeds the set limits, several types of alarms can be programmed from a warning to an immediate shut-down.

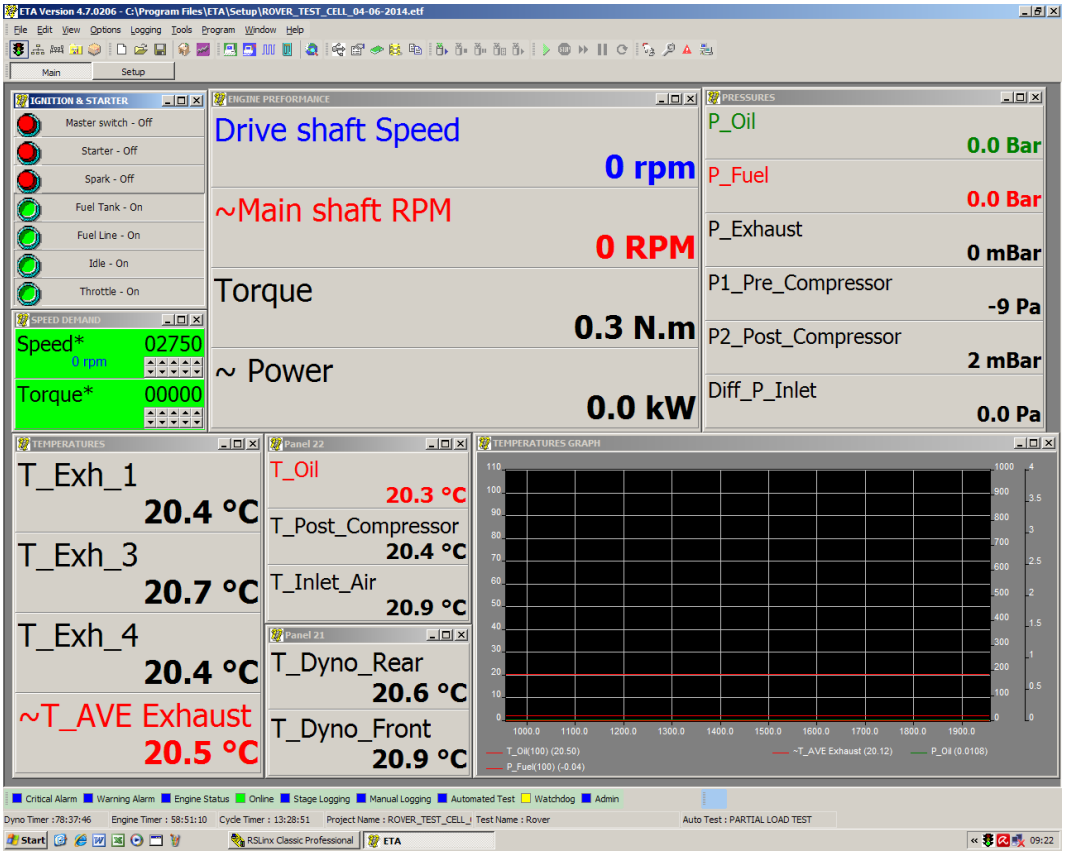

Figure D.1: ETA user interface

D.2. Experimental procedure

The experimental procedure before, during and after each test is discussed briefly in the following sections.

D.2.1. Pre-testing procedure

Visually inspect the entire test bench for any cracks in the structure or leakage of fluids. Always ensure that all couplings are firmly connected and that connections are firmly tightened. Be sure to perform the following checks before conducting any tests:

1. Inspect the gas turbine and check the oil level. Also inspect the fuel system and ensure that there is enough fuel in the fuel tank for the planned tests. In addition make sure that the drive shaft is free to rotate and that all external bolts are tightened and secured.
2. Clear the test-cell of objects that could potentially cause a danger during testing.

3. Ensure that enough water is supplied to the dynamometer and check all couplings and connections.
4. Check the equipment for potential electrical hazards.
5. Perform an excess fuel check- ensure drain valve is normally open.
6. Lastly ensure that the emergency stop button is functioning, check that the channels on ETA are functional and calibrated, and finally turn on the ventilation system and close the doors of the test-cell.

D.2.2. Operating procedure

During operation no one is allowed in the test cell. The start-up, shut down and emergency shut-down procedures are discussed below.

D.2.2.1. Start-up

1. Ensure all fuel system solenoids and manual fuel isolation valve are open.
2. Switch on the starter motor and spark.
3. Introduce fuel when the fuel pressure reaches approximately 2 bar.
4. Switch off the starter motor and spark at 12 krpm.
5. The engine will now spool to 46 krpm and stabilise at this operating speed.

D.2.2.2. Normal shut-down

1. Ensure no dynamometer load is on the gas turbine.
2. Close all fuel system solenoids with use of the master switch, and if shut-down happens during a start-up procedure ensure that the starter motor and spark are switched off.
3. Push the throttling lever forward to close the fuel sprayer.
4. When the main shaft has stopped rotating, monitor the gas turbine temperatures and assist the gas turbine cool down by briefly cranking the gas turbine to approximately 6 krpm.

D.2.2.3. Emergency shut-down

1. Engage the emergency stop button.
2. Simultaneously push the throttling lever forward to close the fuel sprayer.
3. When the main shaft has stopped rotating, monitor the gas turbine temperatures. **DO NOT** crank the gas turbine, instead wait for the gas turbine to cool down before entering the test cell to inspect possible failures. **DO NOT** touch the main casing, the combustion chamber or the gas turbine exhaust because these will still be at a high temperature.

D.2.3. Post-testing procedure

1. Allow all apparatus to cool down.
2. Switch off all equipment and disconnect the battery.
3. Close the water supply and the manual fuel lever at the fuel tank.
4. If the test cell is at atmospheric temperature, switch off the ventilation system.
5. Ensure all recorded experimental performance data is saved on the personal computer and processed for further examination.

D.3. Calibration of the measurement instrumentation

All measuring instrumentation that underwent calibration is connected to the Allen Bradley MicroLogix1200 PLC which communicates with the computer program ETA (see Appendix D.1). Once calibrated the software will save the programmed correlation between the required units and the output signal from the measuring instrumentation. It is therefore not necessary to recalibrate upon every experimental procedure. However, checks were done to ensure that the data remained reliable.

D.3.0.1. Pressure calibration

The static pressure transducers and channels were calibrated using a certified analogue pressure gauge and a hand pump. Festo fittings were used to connect the hand pump with a T-piece to the pressure transducer and the pressure gauge. The hand pump is then used to either compress or decompress the air. The air is compressed to five different values within the pressure measurement range of the particular pressure transducer. The program ETA is then used to capture the pressure reading on the analogue pressure gauge with the corresponding pressure transducer output signal. Following this the program performs a linear regression based on the stepped pressure readings.

The differential pressure transducer has a very small operating range (0-7 kPa) and therefore a Betz manometer is used for precise low pressure difference calibration. In ETA the output signal of the differential pressure transducer was equalled to the pressure reading of the Betz manometer. In order to linearly calibrate the differential pressure transducer the readings are stepped.

D.3.0.2. Thermocouple calibration

The thermocouples used for the temperature measurements were calibrated by the supplier, however the output signal still had to be correlated with the readings in ETA. A temperature probe was used to calibrate the thermocouples by matching the measurement displayed by ETA to the temperature probe reading. After several readings were acquired, a linear regression was performed in ETA to couple the voltage output to a temperature value. The EGT readings were merely used as indicator for safe testing and were not calibrated due to the high temperatures involved.

D.3.0.3. Load cell calibration

The load cell used to measure torque had been calibrated for previous experiments, the span value was checked and any zero offset error was adjusted in ETA.

D.4. Experimental data

This section contains the experimental data at operating point. The standard compressor performance is exhibited in Table D.1, the temperature values are shown in Figure D.2 and the pressure values are displayed in Figure D.3. All values are relatively close to the estimated operating parameters with exception of the compressor efficiency, probably caused by wear (see Table 5.2).

Table D.1: Experimental data of the standard compressor at operating point

Parameters	Values
Inlet static temperature (T) [K]	293.4
Outlet static temperature (T_t) [K]	461.8
Static temperature ratio (T_4/T_1)	1.56
Inlet total temperature (T) [K]	301.7
Outlet total temperature (T_t) [K]	468.1
Total temperature ratio ($T_{t,4}/T_{t,1}$)	1.55
Inlet static pressure (p) [kPa]	95.0
Outlet static pressure (P_t) [kPa]	263.1
Static pressure ratio (p_4/p_1)	2.77
Inlet total pressure (p) [kPa]	101.0
Outlet total pressure (P_t) [kPa]	271.1
Total pressure ratio ($p_{t,4}/p_{t,1}$)	2.68
Pressure ratio total-to-static ($p_4/p_{t,1}$)	2.60
Mass flow ($\dot{m}$) [kg/s]	0.597
Total-to-total isentropic efficiency (η_{TT})	61.2%
Total-to-static isentropic efficiency (η_{TS})	56.8%
Total-to-total polytropic efficiency (η_{TT})	64.0%
Total-to-static polytropic efficiency (η_{TS})	62.1%

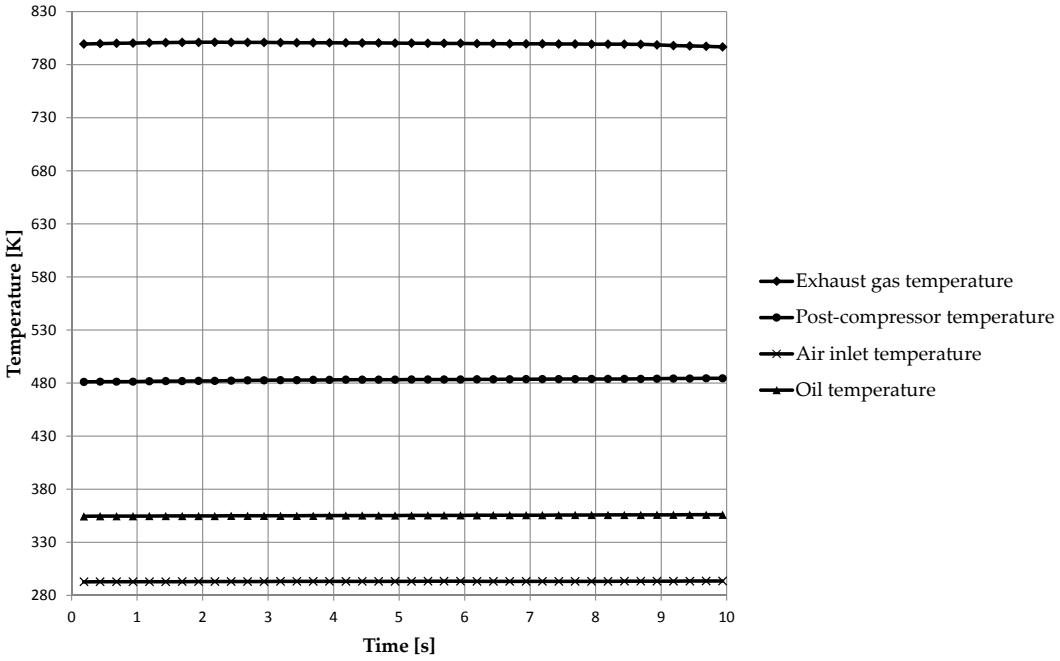

Figure D.2: Experimental temperature values of the RGT 1S/60 at operating point

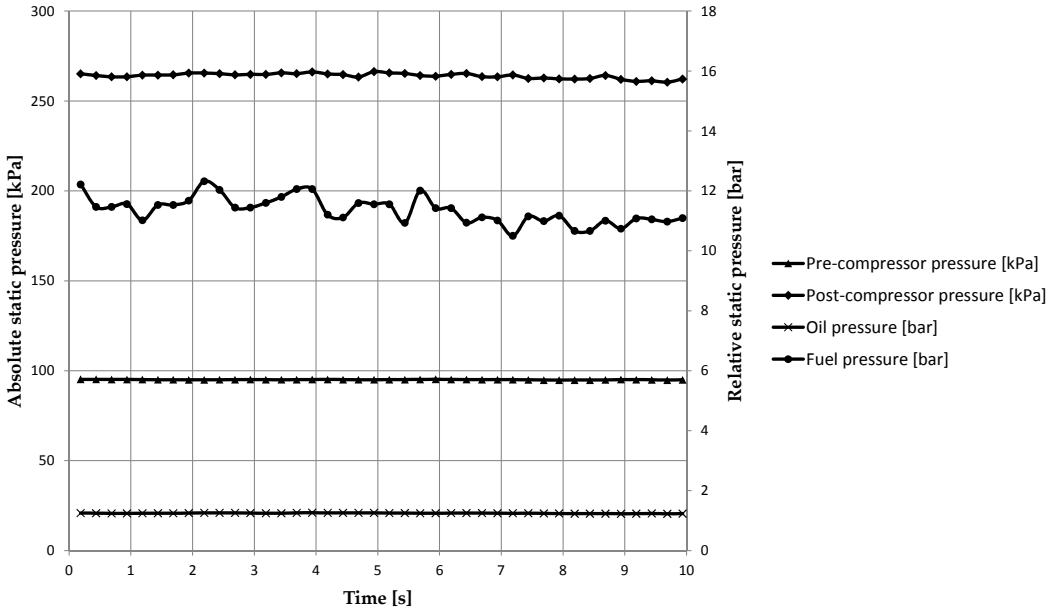

Figure D.3: Experimental pressure values of the RGT 1S/60 at operating point

E. Numerical Analysis Process and Mesh Overview

The numerical analysis process is partly discussed in this section, the user interface of the BladeGen™ software. The compressor meshes of this thesis are exhibited and lastly the y^+ values are displayed.

E.1. BladeGen™ user interface

The BladeGen™ user interface is displayed in Figure E.1 showing the new impeller design with splitter blades. The meridional shape is adjusted in window (a), a 3-D or blade-to-blade view of the final design is shown in window (b), the blade angle and the blade thickness at different span can be modified in window (c) and (d) respectively.

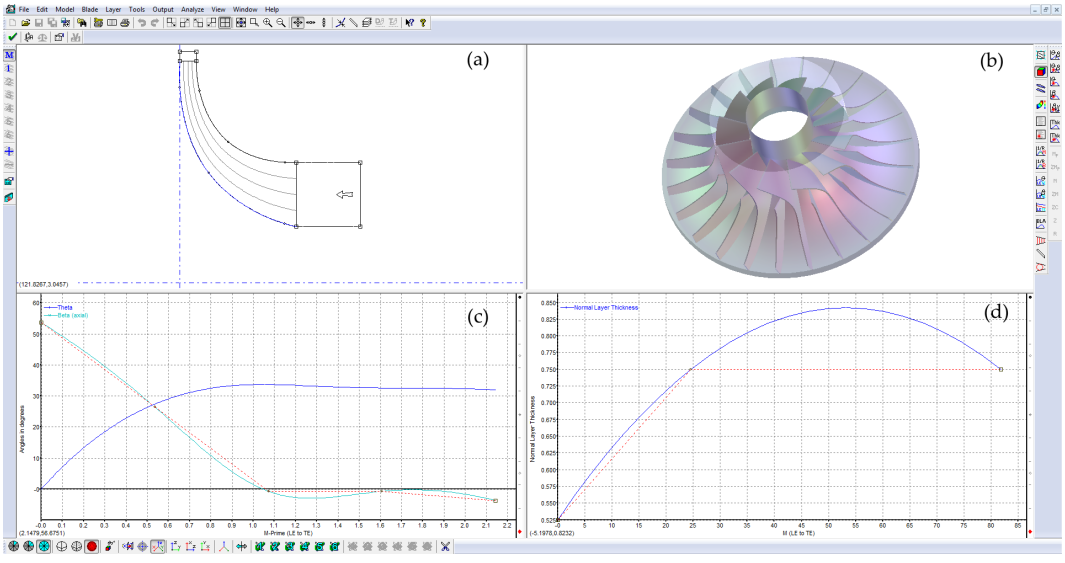

Figure E.1: User interface of ANSYS® BladeGen™

E.2. Mesh details

The mesh configurations of the compressors are provided in this section. The ANSYS® Meshing program was used to mesh the computational geometry of the standard compressor. The computational geometry of the new compressor is meshed with ANSYS® TurboGrid™.

E.2.1. Standard compressor

The 3-D mesh of the standard compressor can be viewed in Figure E.2. Also the surface mesh at the leading edge and trailing edge of the diffuser is displayed in Figure E.3.

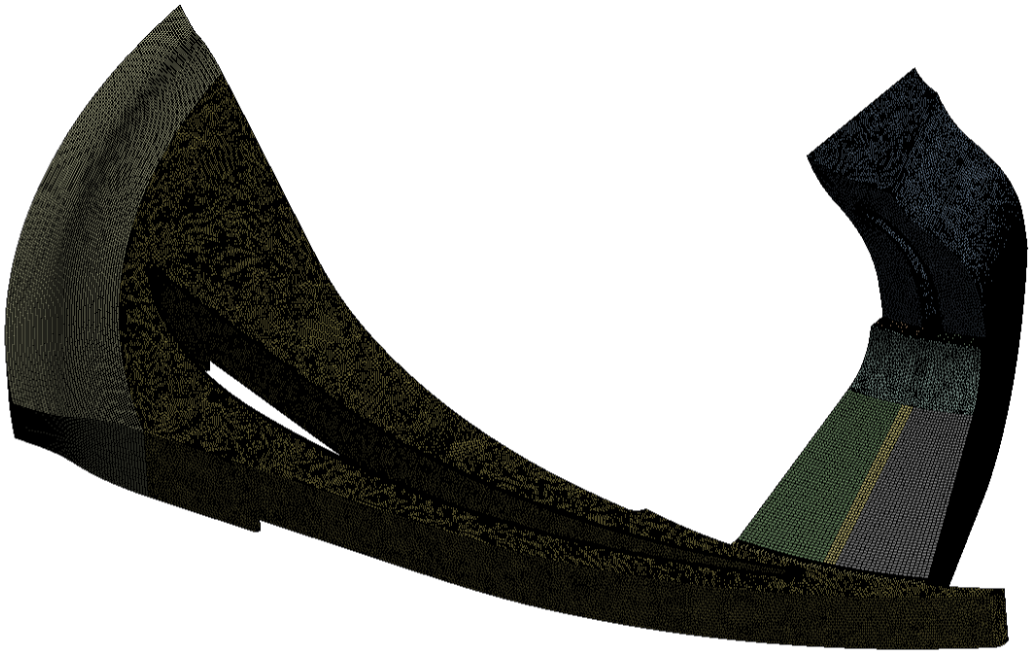

Figure E.2: View of the new standard mesh by ANSYS® Meshing

E.2.2. New compressor

The mesh at the leading edge and trailing edge of the new impeller are shown in Figure E.4. Also the diffuser mesh at the leading edge and trailing edge are displayed in Figure E.5.

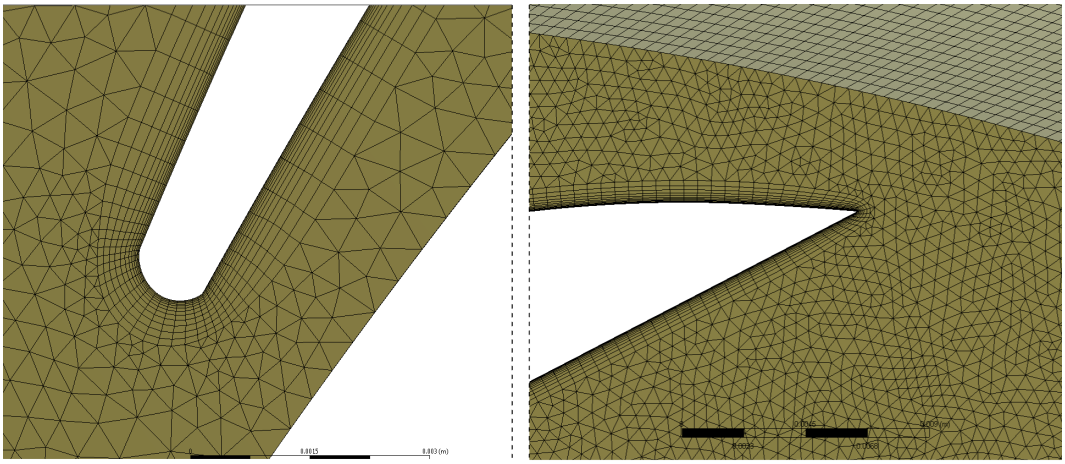

(a) Leading edge (b) Trailing edge

Figure E.3: Leading edge and trailing edge mesh of the standard diffuser by TurboGrid™

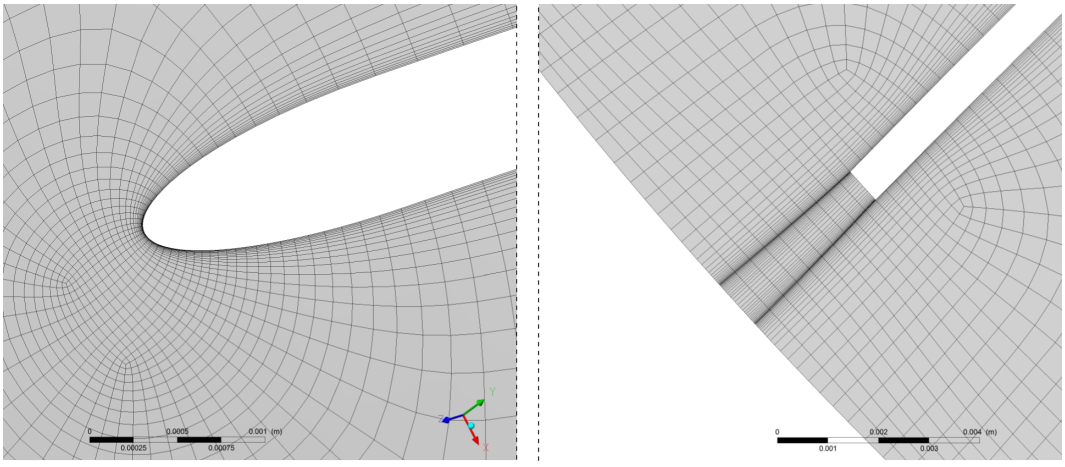

(a) Leading edge (b) Trailing edge

Figure E.4: Leading edge and trailing edge mesh of the new impeller by TurboGrid™

E.2.3. Mesh refinement

For the new compressor the total-to-static efficiency and total-to-static pressure ratio were calculated to preclude mesh dependency. Mesh refinement of the new compressor yielded an efficiency difference between the coarse mesh and the medium mesh, however the difference between the medium and the fine mesh was negligible (Table E.1). The mesh refinement for the standard compressor was not reliable due to recirculation issues at the dif-

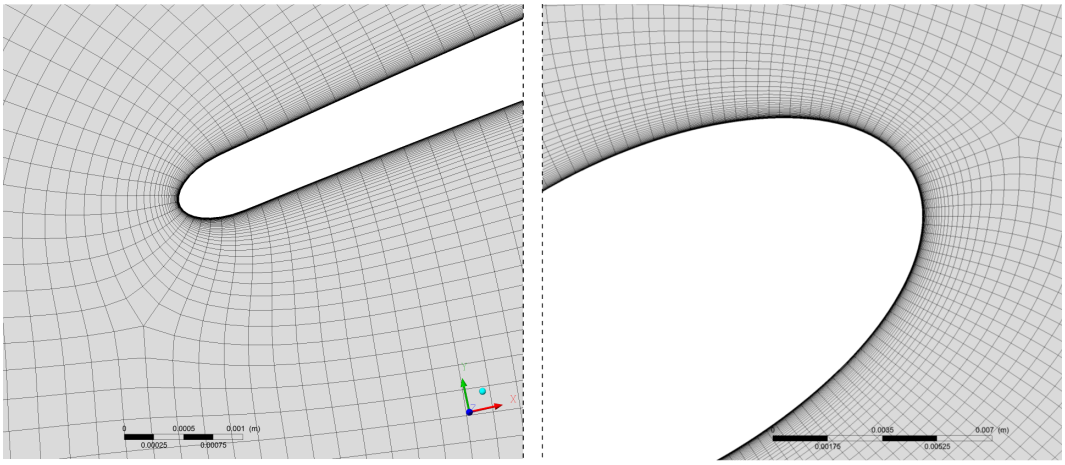

(a) Leading edge (b) Trailing edge

Figure E.5: Leading edge and trailing edge mesh of the new diffuser by TurboGrid™

fuser discharge which caused precarious results, hence the mesh refinement was not conducted.

Table E.1: Mesh dependency of the new compressor

Mesh	Efficiency (t-s)[%]	Pressure ratio (t-s)
Coarse	87.75	3.385
Medium	85.46	3.297
Fine	85.55	3.304

The mesh refinement of the new compressor is indicated in Figure E.6, Figure E.7 and Figure E.8 for the coarse, medium and fine mesh grid levels respectively. Note: the difference between the coarse and medium mesh is mostly in the spanwise direction, even though the coarse and medium surface mesh look alike in the mesh refinement figures.

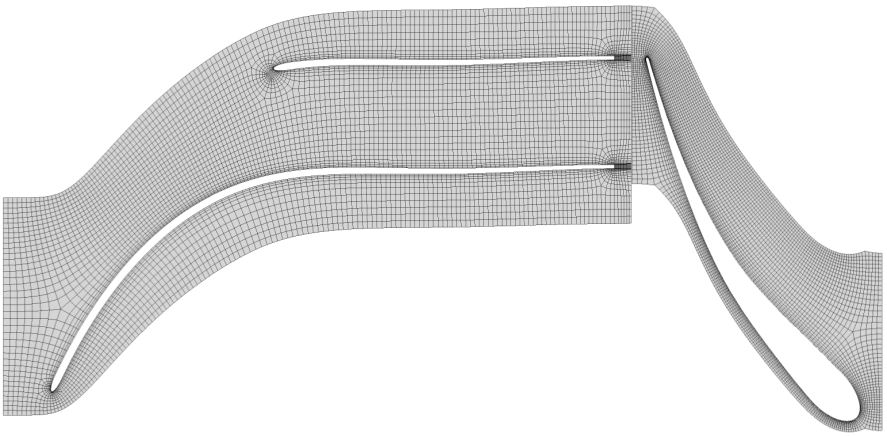

Figure E.6: Top view of the new compressor coarse mesh by TurboGrid™

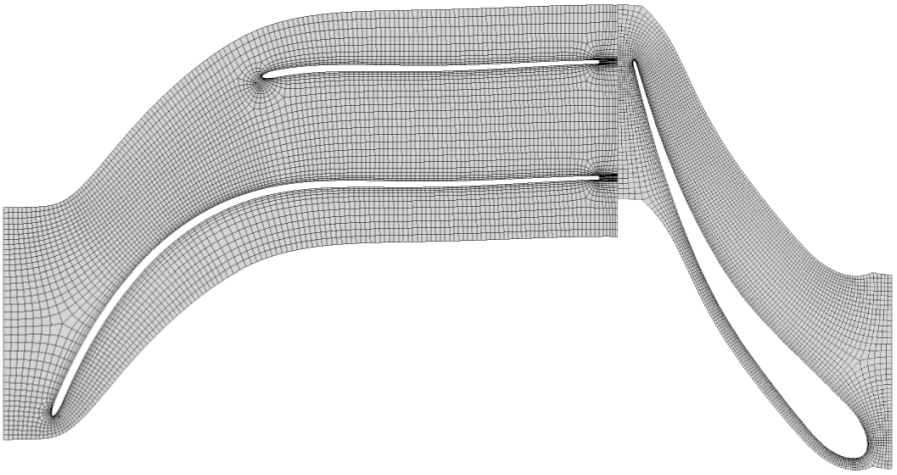

Figure E.7: Top view of the new compressor medium mesh by TurboGrid™

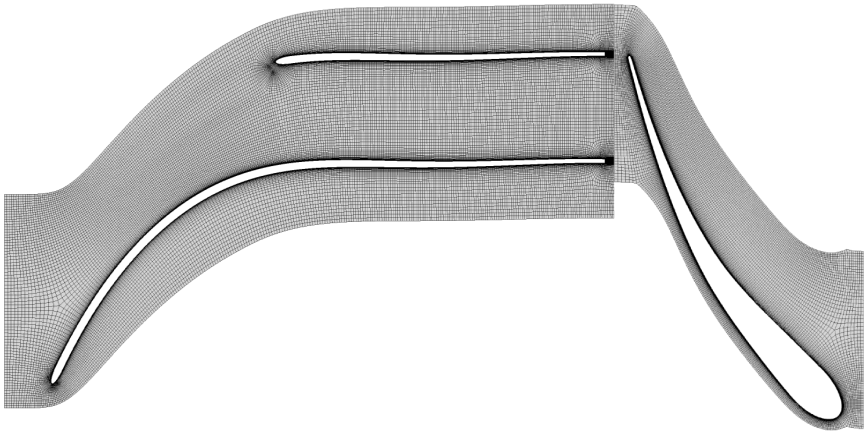

Figure E.8: Top view of the new diffuser fine mesh by TurboGrid™

E.2.4. Region of "bad" cells of the impeller mesh

The shroud clearance mesh at the trailing edge of the impeller blades failed to meet the mesh expansion rate quality criteria, the region of "bad" cells is indicated in Figure E.9. ANSYS, Inc. only recently added cut-off blade support to TurboGrid™ ATM, and this unfortunately is a weak spot that could not be addressed. Since this represents only a fraction of the total number of cells, the mesh was considered acceptable.

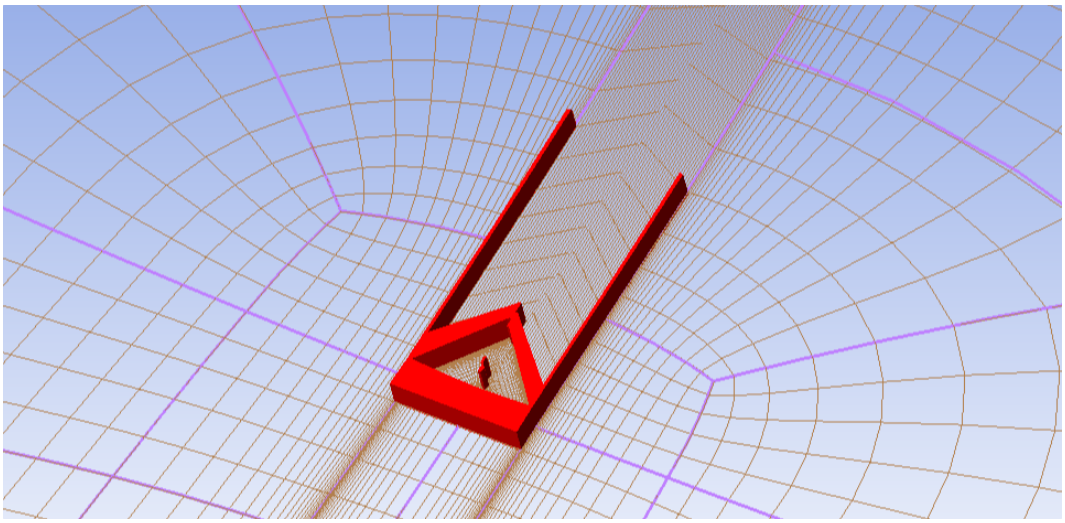

Figure E.9: Region of "bad" cells at the blade trailing edge of the impeller

E.3. y^+ values of the thesis compressors

In order to validate the 3-D meshes and solver setups for both compressors, the y^+ values from CFX® are displayed in this section. For the standard compressor the SST k-ω model was used as discussed in Section 4.4.2. The y^+ value recommended for the SST k-ω flow model is < 300 (ANSYS Inc., 2012*a*), but the model will now not take advantage of the low-Reynolds formulation, which is necessary in order to accurately predict separation. For the standard compressor however the recirculation effect in the diffuser was so strong that accurate separation prediction was deemed insignificant. Figure E.10 exhibits the y^+ values of the standard compressor, which indicates a maximum y^+ of 273 at the additional pinched radial passage at the diffuser outlet.

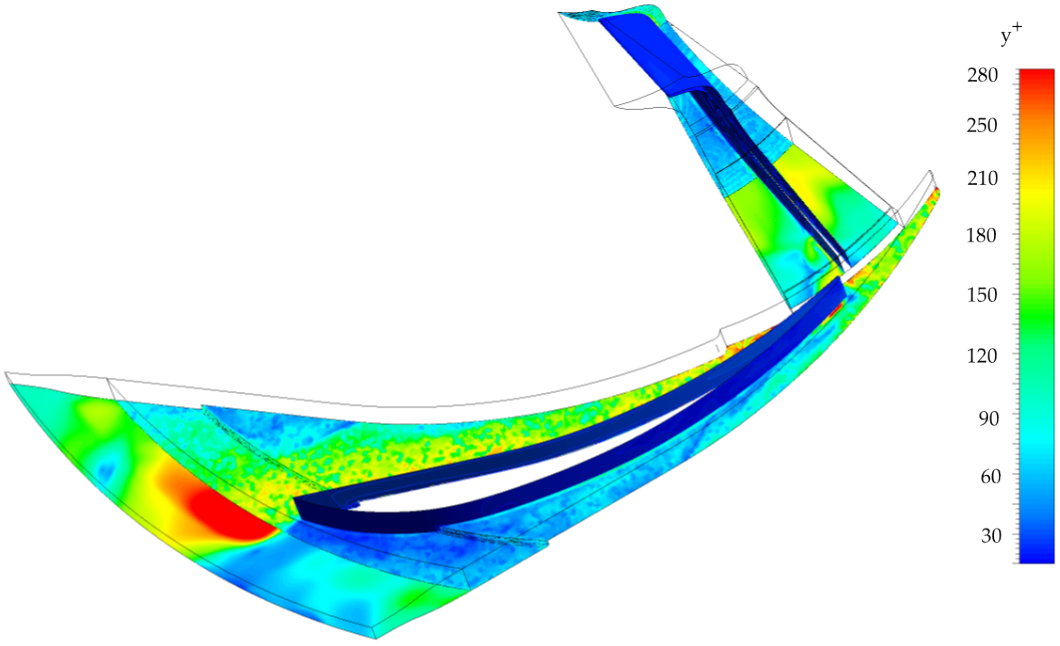

Figure E.10: y^+ values of the standard compressor using the SST k-ω model

The k-ω flow model was utilized for the numerical simulation of the new compressor (Section 4.4.2). To take full advantage of the low-Reynolds formulation in the k-ω model the target y^+ value was $1 \geq y^+ \leq 10$, i.e. in the viscous sublayer. Figure E.11 and Figure E.12 exhibit the y^+ values of the new compressor, which indicates y^+ values mostly below seven with exception of the hub at the inlet and a region at the discharge of the suction side of the impeller main blade where the y^+ is slightly higher but still below 10. The trailing edge surface of the impeller blades is the only region where the

target y^+ is not achieved, which is caused by the mesh at the trailing edge (see Section E.2.4).

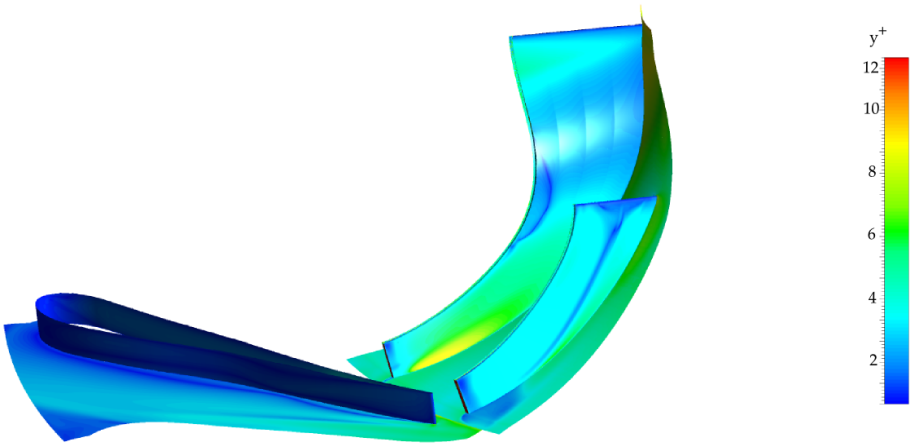

Figure E.11: Suction surface y^+ values of the new compressor using the k-ω model

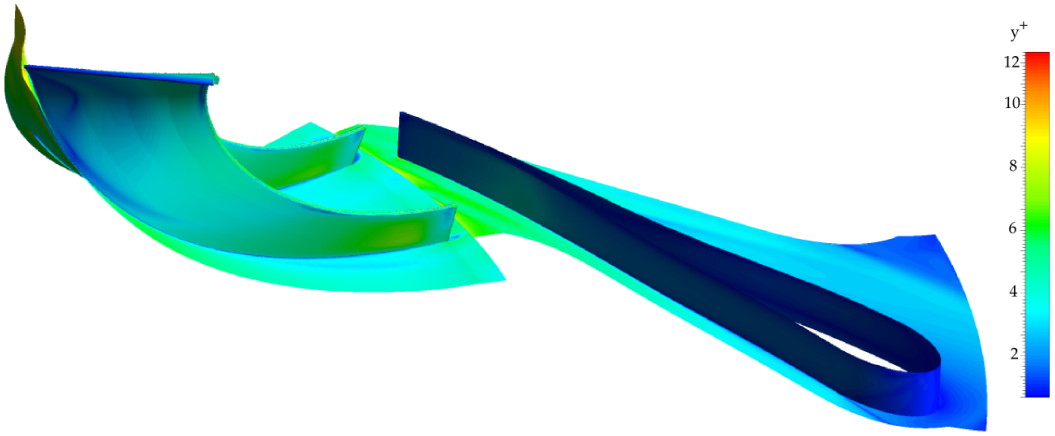

Figure E.12: Pressure surface y^+ values of the new compressor using the k-ω model